Politecnico di Milano

School of Industrial and Information Engineering

Master Degree in Space Engineering

CURRENT-DRIVEN MAGNETIC NOZZLE FLOW COLLIMATION: ANALYTICAL AND EXPERIMENTAL INVESTIGATION FOR PLASMA PROPULSION APPLICATIONS

Supervisor: Prof. Luigi DE LUCA
Co-Supervisor: Prof. Lorenzo CASALINO
External Supervisor: Prof. Edgar Y. CHOUEIRI

Master Thesis of:
Lorenzo FERRARIO 783846

Academic Year 2012 - 2013

Contents

List of Figures

List of Tables

Abstract

Abstract in English Language

Magnetic nozzles are steady state devices used to convert part of the thermal energy of a plasma into direct kinetic energy. These devices find applications in plasma propulsion for space, plasma surface processing and fundamental studies. One of the biggest issues with magnetic nozzles is the observed high beam divergence due to late plasma separation from the guiding field. In this work, the effects of an applied azimuthal electron current at the throat on the flow are analyzed in a finite-electron-temperature magnetic nozzle model. The solution is derived using an approximate analytical model and it shows that such a diamagnetic current increases the performances of the nozzle, especially the thrust coefficient and the specific impulse. A power assessment also shows that this performance gain is achieved more efficiently than what obtainable from plasma heating. Then, three different designs for an actual system to induce the azimuthal current are presented and discussed. The results of the experimental investigation of one of the proposed designs clearly shows that the focusing of the jet does occur, paving the way for the further study and, eventually, for an actual implementation of the concept on space plasma thrusters.

Keywords:
Plasma, Propulsion, Helicon Thruster, Magnetic Nozzle, Collimation

Abstract in Lingua Italiana

Un ugello magnetico è un dispositivo stazionario atto alla conversione di parte dell'energia termica di un plasma in energia cinetica. Questi dispositivi trovano applicazione nella propulsione spaziale al plasma, in sistemi per il trattamento di superfici ed in studi di fisica fondamentale. La tendenza del plasma a rimanere legato al campo magnetico rappresenta uno dei problemi principale di questi dispositivi e porta a scarse efficienze di divergenza dell'ugello. In questo lavoro viene analizzato l'effetto di una corrente elettronica azimutale applicata alla gola in un modello a temperatura elettronica finita. La soluzione analitica ottenuta mostra che una corrente diamagnetica influisce positivamente sulle performance dell'ugello, in particolar modo su coefficiente di spinta ed impulso specifico. Un'analisi delle potenze coinvolte mostra inoltre che questo sistema è più efficiente di un semplice riscaldamento del plasma. Quindi, vengono presentate e discusse tre diverse architetture per l'introduzione di questa corrente azimutale. I risultati di un'indagine sperimentale condotta su una di queste alternative mostrano chiaramente l'effetto collimante del sistema, aprendo la strada per ulteriori studi ed, in futuro, per una possibile implementazione su propulsori al plasma per uso spaziale.

Parole chiave:
Plasma, Propulsione, Helicon Thruster, Ugello Magnetico, Collimazione

Estratto della Tesi

Capitolo 1
Introduzione

La propulsione al plasma costituisce uno dei rami più promettenti dell'estesa famiglia dei sistemi di Propulsione Avanzata per lo Spazio. In generale, i motori al plasma sfruttano gas ionizzati come propellente, accelerandoli per via elettromagnetica o termica a diversi chilometri al secondo, generando così una reazione propulsiva. Questi sistemi hanno impulsi specifici comparabili ai ben noti propulsori a ioni, ma presentano densità di spinta (N/m^2) più alte, al prezzo di richieste di potenza elettrica altrettanto elevate.

Le architetture di propulsione al plasma possono essere classificate in varie categorie. Uno dei più attivi campi di ricerca riguarda la propulsione al plasma termica. In questa architettura, il gas viene ionizzato in una sorgente di plasma (generalmente helicon) e confinato da campi magnetostatici. L'accelerazione del propellente avviene poi per espansione gasdinamica attraverso un ugello convergente-divergente creato dalla stesso campo confinante. I principali vantaggi sono l'assenza di elettrodi, vero fattore limitante della vita operativa di un propulsore, e la possibilità di essere scalati ad alte potenze.

Recentemente, la maggior parte degli studi si sono concentrati sulla fisica che regola il distacco del plasma dalle linee di campo dell'ugello. Infatti, a causa del congelamento delle linee di forza, il gas ionizzato tende a rimanere legato alle superfici magnetiche anche quando queste ritornano su se stesse, producendo un getto con alto grado di divergenza e, di conseguenza, poco efficiente. In un recente articolo, Schmit e Fisch propongono di introdurre

una corrente azimutale prima del divergente dell'ugello per aumentare la collimazione del getto. Tuttavia, simulazioni condotte da Ahedo e Merino mostrano che le ipotesi alla base del modello di Hooper, utilizzato anche da Schmit e Fisch, sono ingiustificate e non permettono di comprendere la natura termo-elettrostatica dell'espansione del plasma negli ugelli magnetici.

In questo lavoro di tesi, dunque, ci proponiamo di risolvere il flusso di plasma in un ugello magnetico con una corrente azimutale, usando un modello più completo che consideri gli effetti termici e discerna il comportamento delle specie del plasma. Verificheremo l'effetto collimante osservato da Schmit e Fisch, cercheremo di comprendere la fisica che regola l'interazione tra corrente azimutale e collimazione del getto e ne valuteremo gli effetti sulle performance propulsive dell'ugello. Infine, proporremo alcune architetture per un sistema che induca tale corrente azimutale e condurremo un'investigazione sperimentale per verificare la fattibilità di una di queste soluzioni.

Capitolo 2
Teoria degli Ugelli Magnetici

Un ugello magnetico è un dispositivo stazionario atto alla conversione di parte dell'energia termica di un plasma in energia cinetica utile alla propulsione. Tale conversione avviene per espansione gasdinamica guidata da campi magnetici grazie alla condizione di congelamento delle linee di forza tipica dei plasmi quasi-ideali. Negli ugelli magnetici Electron-Driven, la maggior parte di questa energia termica è immagazzinata negli elettroni, che quindi guidano l'espansione. La separazione di carica viene prevenuta dall'insorgere di campi elettrostatici autoindotti che trascinano gli ioni, generando così la spinta.

Per lo studio di questi dispositivi possiamo avanzare diverse ipotesi di lavoro, tra cui: inerzia elettronica e temperatura ionica trascurabili, comportamento isotermico degli elettroni, assisimmetria e stazionarietà del flusso. Altre assunzioni prevedono di trascurare collisioni, viscosità e campi magnetici autoindotti (plasma n regime di basso β).

Capitolo 3
Il Moto di Swirl negli Ugelli Magnetici

In questa sezione valuteremo le forze indotte dal moto di swirl su ciascuna delle popolazioni di un plasma in moto in un ugello divergente, specializzando poi per il caso comune di plasma composto da elettroni e ioni a singola carica. Seguirà poi lo sviluppo e la discussione di un modello quasi-monodimensionale dell'ugello in regime di corrente azimutale.

Valutazione delle Forze Indotte dal Moto di Swirl

Data l'equazione della quantità di moto della popolazione a in un modello a più fluidi in coordinate cilindriche, possiamo estrarre i termini meridionale (r, z) ed azimutale (ϑ):

$$m_a(\tilde{\mathbf{u}}_\mathbf{a} \cdot \nabla)\tilde{\mathbf{u}}_\mathbf{a} = -\frac{1}{n_a}\nabla P_a - q_a \nabla\phi + q_a u_{\theta\mathrm{a}} B\hat{\mathbf{n}} + m_a \frac{u_{\theta a}^2}{r}\hat{\mathbf{r}} \quad , \tag{1}$$

$$m_a(\tilde{\mathbf{u}}_\mathbf{a} \cdot \nabla) r u_{\theta\mathrm{a}} = q_a(\tilde{\mathbf{u}}_\mathbf{a} \times \mathbf{B}) \cdot r\hat{\vartheta} \quad . \tag{2}$$

Introducendo la coordinata magnetica ψ definita come

$$\mathbf{B} = \frac{1}{r}(\hat{\vartheta} \times \nabla\psi) \quad , \tag{3}$$

otteniamo che il moto azimutale influisce sull'equazione meridionale attraverso il termine

$$\mathbf{F}_\mathbf{a}^\theta = q_a u_{\theta\mathrm{a}} B\hat{\mathbf{n}} + m_a \frac{u_{\theta\mathrm{a}}^2}{r}\hat{\mathbf{r}} \quad . \tag{4}$$

Dall'eq. (4) possiamo ricavare delle condizioni sulla velocità azimutale in gola ($u_{\theta\mathrm{a}}^0$) affinché la forza $\mathbf{F}_\mathbf{a}^\theta$ abbia un effetto collimante ed accelerante per il flusso. Imponendo valore negativo per la componente radiale di $\mathbf{F}_\mathbf{a}^\theta$ in un plasma a due specie (elettroni e ioni a singola carica), si ottiene che la frequenza angolare della linea di flusso alla gola $\omega_a^0 = u_{\theta\mathrm{a}}/R_a^0$ è limitata da

$$\begin{cases} -\Omega_i^0 < \omega_i^0 < 0 \\ \\ 0 < \omega_e^0 < \Omega_e^0 \end{cases} \quad , \tag{5}$$

dove $\Omega^0_{\mathrm{i,e}}$ è la frequenza di ciclotrone alla gola dell'ugello. Quando queste disuguaglianze sono rispettate, la componente radiale della forza di Lorentz sovrasta la forza centrifuga e l'effetto è collimante. Il massimo effetto collimante si ottiene esattamente nel mezzo dell'intervallo ammissibile. Allo stesso modo, imponendo valore positivo alla componete assiale di $\mathbf{F}^{\theta}_{\mathbf{a}}$, si ottiene la condizione per cui l'interazione sia accelerante per il flusso:

$$-\frac{q_a}{|q_a|}\omega_a^0 > 0 \quad . \tag{6}$$

Modello Quasi-Monodimensionale

Seguendo una pratica diffusa nella scienza della propulsione aerospaziale, sviluppiamo un modello stazionario quasi-monodimensionale del flusso nell'ugello sotto l'influenza di correnti azimutali ioniche ed elettroniche. L'equazione di evoluzione assiale del numero di Mach assume la forma

$$\left(1-\frac{1}{M_z^2}\right)\frac{dM_z}{dz} = \frac{1}{AM_z}\frac{dA}{dz} + S(z) + L(z) \quad , \tag{7}$$

dove S(z) e L(z) rappresentano rispettivamente il recupero di energia cinetica azimutale e la componente assiale della forza di Lorentz.

$$S(z) = -\frac{1}{M_z}\frac{d}{dz}\left(\frac{1}{A}\int_A \frac{1}{2}M_{\theta\mathrm{i}}^2 dA\right) \quad , \tag{8}$$

$$L(z) = \frac{1}{M_z}\int_A \left(M_{\theta\mathrm{i}} - M_{\theta\mathrm{e}}\right)\Psi'_z(z)dA \quad . \tag{9}$$

Specializzando l'eq. (7) nella condizione di minima area ($dA/dz = 0$) verifichiamo che anche in questo caso il flusso transita in regime supersonico nella gola dell'ugello.

Risolvendo numericamente l'equazione (7) con condizioni iniziali consistenti con la condizione (5), otteniamo due importanti risultati. In primo luogo, notiamo che è molto più efficace agire sul fluido elettronico che su quello ionico a causa delle stringenti limitazioni sul moto di quest'ultimo derivanti dalla relazione (5). Inoltre, ricaviamo che la componente radiale della forza di Lorentz domina sempre ogni altra interazione. Dunque, per analizzare l'effetto della corrente azimutale sarà necessario espandere il modello ad una descrizione multidimensionale.

Capitolo 4
Flusso in Ugello Magnetico con Corrente Elettronica Azimutale

Nel presente capitolo, provvederemo a sviluppare una modellazione stazionaria multi-dimensionale assisimmetrica del flusso nella regione divergente dell'ugello in presenza di corrente elettronica azimutale nella regione di gola. Porremo particolare attenzione all'influenza di questa corrente sulle condizioni di equilibrio del plasma.

Approccio

Al fine di studiare il comportamento del flusso di plasma in un ugello magnetico sotto l'effetto di una corrente azimutale, introduciamo una foza di volume F azimutale nelle equazioni di governo di una colonna infinita di plasma magnetizzato. Questa forza, agendo sulla sola popolazione elettronica, induce una corrente azimutale nel plasma, modificandone le condizioni di equilibrio. Utilizzeremo poi la soluzione così ottenuta come condizione al contorno in gola per la risoluzione del flusso nell'ugello divergente.

Questo approccio è differente da quanto adottato in precedenza da Schmit e Fisch: essi infatti imposero un profilo arbitrario di velocità di swirl ad entrambe le specie nella sezione di gola, risolvendo poi il flusso in accordo con il modello di plasma freddo di Hooper. Tuttavia, recenti simulazioni hanno mostrato come le ipotesi di temperature trascurabile non permettono un'accurata descrizione della fisica dell'ugello. Di conseguenza, i termini di gradiente di densità non possono essere scartati e non è più possibile imporre un profilo di velocità azimutale senza prima introdurre una variabile addizionale nel sistema di Navier-Stokes.

Condizioni al Contorno per Ugello Divergente con Corrente Elettronica Azimutale

Assumendo geometria assisimmetrica, comportamento isotermico degli elettroni e trascurando i termini di inerzia elettronica, possiamo introdurre que-

sta forza F nel sistema di equazioni di governo di una colonna infinita di plasma confinata da campo magnetico assiale, così da ottenere un'equazione di diffusione modificata:

$$\frac{d^2\hat{n}}{d\hat{r}^2} + \left(\frac{1}{\hat{r}} + \frac{\hat{\omega}_{\mathrm{lh}}}{\hat{\nu}_e}\hat{F}\right)\frac{d\hat{n}}{d\hat{r}} + \left(a_0^2 + \frac{\hat{\omega}_{\mathrm{lh}}}{\hat{\nu}_e}\frac{d\hat{F}}{d\hat{r}} + \frac{\hat{\omega}_{\mathrm{lh}}}{\hat{\nu}_e}\frac{\hat{F}}{\hat{r}}\right)\hat{n} = 0 \quad , \tag{10}$$

dove $\hat{\omega}_{\mathrm{lh}}$ è la frequenza ibrida inferiore, che agisce da parametro di magnetizzazione, $\hat{\nu}_e$ è la frequenza di collisione tra elettroni ed altre popolazioni (ioni ed atomi neutri). La coordinata radiale è adimensionalizzata con la posizione dello sheath del plasma in caso di $F = 0$, ossia $R_s^0 = 1$. Le energie sono adimensionalizzate con la temperatura T_e, le velocità con la velocità sonica $c_s = \sqrt{T_e/m_i}$ e le frequenze con c_s/R_s.

Per poter proseguire con un'analisi quantitativa, imponiamo una forma alla forza $\hat{F}$:

$$\hat{F} = \hat{\Omega}\hat{r} - \hat{u}_{\theta\mathrm{e}} \quad . \tag{11}$$

Una forza così definita tende a muovere gli elettroni verso un moto rigido di frequenza agolare $\hat{\Omega}$. Sostituendo l'espressione (11) in (10) e risolvendo per $\hat{n}(\hat{r})$, otteniamo le nuove condizioni di equilibrio della colonna di plasma. Si nota così che una forza $\hat{F}$ positiva (cioè che induce una corrente diamagnetica) porta ad un maggiore confinamento del plasma.

Approssimazione Analitica Bidimensionale del Flusso nell'Ugello Magnetico

Ci proponiamo ora di risolvere il flusso bidimensionale nel tratto divergente dell'ugello, sfruttando le condizioni di equilibrio appena ottenute come condizioni al contorno in gola. A tal fine, riprendiamo ed estendiamo il modello di Little e Choueiri, che permette di ottenere un'approssimazione analitica della soluzione, basata sulla scrittura delle equazioni in coordinate magnetiche ψ e ζ:

$$\mathbf{B} = \frac{1}{r}(\hat{\vartheta} \times \nabla\psi) = -\nabla\zeta \quad . \tag{12}$$

Le equazioni di governo si ottengono proiettando le equazioni del modello multi-fluido lungo le linee di forza dei campi di velocità e magnetici,

utilizzando inoltre le assunzioni precedentemente introdotte.

$$\begin{cases} \hat{\mathbf{s}} \cdot \nabla \left(\frac{1}{2} M_i^2 + \phi \right) = 0 \\ \hat{\mathbf{b}} \cdot \nabla \left(\phi - \ln(n) \right) = 0 \\ \int_S n\tilde{M}\ \tilde{\mathbf{s}} \cdot \mathbf{dA} = 0 \\ \hat{\mathbf{b}} \cdot \nabla \left(M_{\theta \mathrm{e}} r \right) = 0 \\ \hat{\mathbf{b}} \approx \hat{\mathbf{s}} \end{cases} . \tag{13}$$

L'adimensionalizzazione sfrutta come grandezze di riferimento la temperatura T_e, la velocità sonica c_s, il campo magnetico al centro della sezione di gola B_0 ed il raggio della singola spira che genera il campo magnetico $a_e = 1$. L'ultima equazione prende il nome di approssimazione di campi quasi-allineati e permette di semplificare notevolmente la trattazione. Dato che le proiezioni di un vettore sulle due direzioni (velocità e campo magnetico) sono proporzionali a $1 - \cos(\alpha_{\mathrm{ei}})$, esse sono all'incirca identiche tra loro per $\alpha_{\mathrm{ei}} \ll 1$ occorrenza che si verifica in tutto l'ugello e che giustifica l'approssimazione introdotta. Il sistema può essere quindi riscritto come dipendente dalla sola variabile ϕ, ossia il potenziale elettrostatico, che trova una soluzione analitica anche nel caso di corrente elettronica azimutale non trascurabile.

Come condizioni al contorno in gola sfruttiamo la soluzione modificata dell'equilibrio della colonna infinita di plasma ottenuta tramite l'introduzione della forza F. Questo accoppiamento modella l'introduzione di uno stadio di collimazione del getto nella regione convergente dell'ugello. Dalle equazioni riscritte si ricava inoltre che l'unica influenza della corrente elettronica azimutale è concentrata alla sezione di gola e si propaga a valle in virtù della natura iperbolica delle equazioni dei fluidi supersonici. Risolvendo il flusso nell'ugello, osserviamo una significativa collimazione del getto ed una più rapida accelerazione del flusso lungo l'asse.

Capitolo 5
Applicazioni Propulsive

In questo capitolo valuteremo l'effetto della corrente azimutale sulle performance propulsive dell'ugello magnetico e sulle potenze caratteristiche del getto e dello stadio di collimazione. Successivamente, presenteremo tre architetture di stadio di collimazione in prospettiva di una verifica sperimentale del concetto, sviluppata nel Capitolo 6.

Performance Propulsive

Avendo risolto il flusso bidimensionale nell'ugello, ci è ora possibile caratterizzare l'effetto della corrente azimutale sulle prestazioni propulsive dell'ugello magnetico ed, in definitiva, dell'intero propulsore. Definiamo quindi l'efficienza di divergenza dell'ugello come il rapporto tra potenza assiale e potenza totale del getto, calcolata sulla ζ-superficie corrispondente al punto di inversione del campo magnetico, ed osserviamo che essa dipende dal semi-angolo di divergenza del getto, essendo proporzionale a $1 - \cos^2(\theta\text{div})$. Allo stesso modo, richiamiamo la definizione di coefficiente di spinta ed impulso specifico, normalizzando quest'ultimo con la velocità sonica. Usando l'approssimazione a campi quasi-allineati, otteniamo:

$$\begin{cases} \eta_{\text{div}} = \dfrac{\mathcal{P}_b^*}{\mathcal{P}_b} = \displaystyle\int_{\zeta_{tp}} nM^3 \frac{B_z^2}{B^2} dA \Big/ \int_{\zeta_{\text{tp}}} nM^3 dA \\ C_T = \dfrac{1}{\bar{n}_t A_t} \displaystyle\int_{\zeta_{tp}} n \left(M^2 + 1\right) \frac{B_z}{B} dA \\ \hat{I}_{\text{sp}} = \dfrac{g_0 I_{\text{sp}}}{c_s} = \eta_n C_T \end{cases} . \tag{14}$$

Tutti i parametri di performance analizzati mostrano un miglioramento con l'applicazione della forza confinante $\hat{F}$. In particolare, l'efficienza aumenta con il decrescere dell'angolo di divergenza del getto, principalmente a causa della variazione della coordinata di sheath. Ancora più evidente è l'incremento di coefficiente di spinta ed impulso specifico, poiché affetti anche dall'aumento del valore di picco del profilo di densità in gola. In generale, i maggiori miglioramenti di performance si osservano per alti valori di magnetizzazione $\hat{\omega}_{\text{lh}}$ e, soprattutto, per configurazioni inizialmente inefficienti, ossia

ad alto r_e. Poiché r_e indica il rapporto tra il raggio dell'area di gola e quello delle bobine dell'ugello, notiamo che il miglioramento di prestazioni influenza maggiormente propulsori con bobine piccole, a parità di area di gola. Dunque, possiamo pensare di sfruttare questa corrente azimutale per progettare propulsori più piccoli, a parità di efficienza, con tutte le conseguenze positive in termini di potenza e massa che ne conseguono.

Valutazione delle Potenze

Per verificare l'efficienza del sistema descritto nell'aumentare le performance dell'ugello, possiamo confrontare la potenza introdotta tramite la corrente azimutale con l'incremento di potenza assiale del getto dovuto alla maggiore collimazione. Inoltre, ci si potrebbe chiedere se l'applicazione di questo stadio di collimazione sia più efficiente di un semplice riscaldamento del plasma. Dall'analisi dei rapporti tra queste potenze, si nota che l'utilizzo dello stadio di collimazione permette una migliore conversione di potenza termica in potenza propulsiva, risultando anche significativamente più efficiente del semplice riscaldamento del getto.

Progettazione dello Stadio di Collimazione

Avendo valutato l'utilità di aggiungere uno stadio di collimazione al propulsore, presentiamo ora un progetto concettuale per tre diverse architetture di stadio di collimazione, mostrando vantaggi e svantaggi di ciascuna.

La prima architettura prevede l'utilizzo di un brusco innalzamento del campo magnetico assiale per indurre rotazione azimutale diamagnetica nelle popolazioni del plasma. Le particelle fluide, non potendo seguire le linee di campo in questo cambiamento repentino, accelerano in direzione azimutale per conservare il momento angolare. Questo sistema ha il vantaggio di essere passivo, cioè di non prevedere alcuna immissione di potenza nel plasma. La complessità nella realizzazione pratica di tale topologia di campo e la presenza di effetti di specchio magnetico sono i maggiori svantaggi di questo sistema.

In alternativa, è possibile ottenere il moto azimutale tramite l'effetto Hall indotto da un campo elettrico radiale tra due elettrodi cilindrici concentrici

immersi in un plasma ad alto parametro di Hall. La semplicità di realizzazione ed operazione rappresentano il principale vantaggio di questa architettura. Tuttavia, la presenza di sheath e strati limite, le perdite negli elettrodi ed i problemi termici e di sputtering riducono l'efficienza di questa opzione, rendendola poco adatta ad applicazioni di alta potenza.

La terza alternativa fa uso di un campo magnetico trasversale rotante (Rotating Magnetic Field - RMF) che, interagendo con gli elettroni, permette l'induzione di una corrente azimutale. Questo sistema ha il vantaggio di non essere intrusivo per la colonna di plasma e di concentrare l'effetto collimante nelle regioni periferiche del plasma, dove è più utile ai fini del confinamento. La necessità di una sorgente di radiofrequenza, di un variatore di fase e di un set di antenne, circuiti di adattamento ed amplificatori fanno della complessità implementativa il difetto più significativo di questa architettura.

Capitolo 6
Verifica Sperimentale

In questo capitolo descriveremo l'indagine sperimentale condotta presso il laboratorio di propulsione elettrica e fisica dei plasmi dell'Università di Princeton (EPPDyL) per lo studio di una delle tre architetture di stadio di focalizzazione descritte in precedenza. Dunque, presenteremo in breve gli obbiettivi ed i risultati dell'esperimento, evidenziandone poi i limiti e le possibilità di miglioramento.

Obbiettivi dell'Indagine Sperimentale

Per motivazioni tecnologiche ed economiche è stato convenuto internamente al laboratorio di realizzare l'architettura ad elettrodi concentrici. I principali obbiettivi dell'indagine sono: la verifica della capacità del sistema di creare una corrente azimutale nel plasma; la caratterizzazione del profilo radiale di densità e potenziale elettrostatico del plasma internamente allo stadio di focalizzazione; l'investigazione degli effetti dello stadio di focalizzazione sul getto esterno al propulsore.

Le misure interne allo stadio di collimazione sono state ottenute tramite una sonda Mach-emissiva combinata ed una sonda di Langmuir a singolo lato, mentre per le misure esterne al propulsore abbiamo utilizzato una sonda di Langmuir completa.

Risultati

Applicando un voltaggio tra gli elettrodi è possibile misurare una corrente tra di essi. Diagrammando a diversi valori di magnetizzazione, osserviamo questa corrente crescere inizialmente in maniera lineare con il voltaggio, per poi tendere verso un valore asintotico dipendente dal campo magnetico e che possiamo correlare con la corrente di saturazione elettronica all'anodo. Inoltre, si evidenzia la presenza di un valore di voltaggio diverso da zero perché la corrente tra gli elettrodi sia nulla. Tale voltaggio a corrente nulla è legato al potenziale del plasma a differenti valori di campo magnetico, nonché alle diverse dimensioni di anodo e catodo ed alla distribuzione radiale di densità all'interno dello stadio di collimazione.

I profili di densità misurati tra gli elettrodi mostrano chiaramente che il confinamento del getto aumenta al crescere del voltaggio applicato. Fenomeni erosivi sulla linea di alimentazione del gas hanno impedito una caratterizzazione completa della densità di corrente azimutale, tuttavia alcune misure mostrano che una corrente elettronica diamagnetica viene effettivamente indotta dal sistema di elettrodi. Gli andamenti del potenziale di plasma rispecchiano le previsioni, mostrando elevato potere schermante dello sheath attorno al catodo. A partire dalle caratteristiche del plasma e dai campi applicati e misurati è possibile ottenere una derivazione indiretta della corrente azimutale indotta nello stadio di collimazione. Da questi calcoli ne evince che la collimazione del getto, parametrizzata dal valore di picco della densità, cresce con l'aumentare della corrente azimutale introdotta, come concettualmente previsto dalla teoria.

Le misure all'esterno del propulsore mostrano che i profili di densità modificati dal sistema di focalizzazione effettivamente si propagano a valle della gola, così come previsto dalla teoria. Ne deriva un getto più collimato, con effetto a crescere con l'aumentare del voltaggio applicato tra gli elettrodi. Questo effetto osservato è significativo, nonostante la potenza introdotta

nello stadio di collimazione non superi mail 10 % della potenza totale della sorgente di plasma. Ne deriva che il sistema così implementato è un efficace metodo per incrementare le performance del propulsore, sebbene non sia nemmeno ottimizzato in disegno e materiali.

Possibili Miglioramenti e Lavori Futuri

Carichi termici sulla linea di alimentazione, erosione e deposizione di materiale eroso hanno posto le maggiori problematiche alle operazioni dell'esperimento descritto. Al fine di migliorare la riproducibilità delle misure e prolungare la vita operativa, è consigliabile una rivisitazione del sistema di alimentazione del gas. In particolare, le parti in acciaio dovrebbero essere sostituite con materiali più resistenti ad erosione, come il molibdeno, che ha mostrato ottimo comportamento a contatto con il plasma.

Dai risultati dell'analisi sperimentale possiamo identificare aree di interesse per un futuro proseguimento dell'indagine sperimentale. Una volta risolti i problemi di erosione, è assolutamente prioritario caratterizzare il profilo di corrente azimutale, per verificare che l'effetto di collimazione sia effettivamente dovuto all'interazione di Lorentz tra corrente e campo magnetico. Inoltre, riteniamo interessante investigare la transizione del plasma attorno alla gola dell'ugello, in quanto il confronto tra gli andamenti della densità dentro e fuori allo stadio di collimazione sembra suggerire la presenza di fenomeni di diffusione perpendicolare al campo magnetico. Infine, suggeriamo di effettuare una completa caratterizzazione del flusso al di fuori dell'ugello, per confrontarlo con la configurazione originaria senza elettrodi.

Capitolo 7
Conclusioni

Al termine di questo lavoro, possiamo trarre le seguenti conclusioni.
L'applicazione di una corrente azimutale al flusso di plasma in un ugello magnetico interagisce con la dinamica bidimensionale del getto tramite la modifica della distribuzione radiale di densità alla gola. Derivazioni teoriche mostrano che una corrente diamagnetica è in grado di aumentare significa-

tivamente le performance dell'ugello, in particolare coefficiente di spinta ed impulso specifico, tramite una migliore collimazione del flusso di plasma. Di conseguenza, è stato possibile avanzare alcune proposte per la progettazione di uno *stadio di collimazione*. L'investigazione sperimentale condotta su una di queste soluzioni ha mostrato chiaramente l'effetto benefico del sistema. In conclusione, riteniamo che il concetto di stadio di collimazione sia molto promettente come metodo per incrementare le prestazioni propulsive dell'ugello ed in quanto tale sia degno di ulteriori approfondimenti.

Acknowledgments
Ringraziamenti

Dunque, eccomi qui a fare il punto della situazione, guardando insieme indietro ed in avanti, in un mix di gioia, malinconia, eccitazione ed un (bel) po' di terrore. Ho passato molto tempo a riflettere su queste due pagine, forse anche più del dovuto. Tuttavia, dato che con ogni probabilità saranno di gran lunga la parte più letta di questa tesi, credo meritino qualche attenzione. Vorrei quindi rivolgermi direttamente a ciascuna di queste persone, a ciascuno di voi, come in una lettera che non ho mai avuto il tempo di scrivervi.

Parto ringraziando voi, Luisella e Claudio, mamma e papà, per avermi sostenuto sempre, per avermi aperto ogni porta possibile e soprattutto per essere l'esempio che intendo seguire. Non so con che parole ringraziarti, Andrea, ma forse con una frase posso riassumere tutto: grazie per essere il *mio* gigante che mi lasciato salire sulle spalle.
Grazie a voi, nonni Angela e Carletto, Maria e Franco. Grazie per avermi tenuto per mano da quando ancora non camminavo e per le innumerevoli volte che, guardandomi crescere, mi avete stuzzicato nella mie passioni.
Un grazie a voi della compagnia Gnah, a voi compagni di viaggio di GM, a voi famiglia di Ludosport ed a voi compagni di corso per aver condiviso con me gioie e dolori di questi anni. A tutti voi di D-Orbit ed in particolare a Luca, Giuseppe, Thomas e Renato: grazie per aver creduto in me prima ancora che potessi farlo io. E grazie specialmente a te, Elena, per avermi fatto da sorella maggiore in tante occasioni.
Grazie a tutti voi zii, cugini, amici ed a te che leggendo queste righe non

hai trovato il tuo nome, perchè chi sono è anche frutto delle esperienze che abbiamo condiviso.

To my labmates, thank you guys for sharing these months with me, and especially thank you Justin, for the invaluable guide, and Bob, for the precious help. A special thank to Mike, best housemate ever, for having literally saved me from the street on my very first day in the US.

Vorrei ringraziare anche il Prof. Passoni, che non credo se l'aspetti, per avermi fatto meravigliare ancora davanti alla fisica quando credevo di essere già sufficientemente maturo da non aver più nulla di cui stupirmi.

Un sentito ringraziameno al Prof. De Luca, per avermi seguito come relatore ed avermi dato la possibilità di vivere quest'esperienza, ed al Prof. Casalino per aver accettato il ruolo di Co-Relatore per il Politecnico di Torino. I wish to deeply thank Prof. Choueiri for having hosted me in his lab during these months and having believed in my ideas since the very beginning.

Infine, poichè la parte migliore arriva sempre alla fine, grazie a te, Veronica. Grazie per la felicità che mi hai donato crescendo insieme a me, ma che sono sicuro essere solo un riflesso di quella che ancora ci aspetta.

Ad Angela e Carletto,
esempio d'amore

Chapter 1

Introduction

1.1 Background and Motivation

Plasma Propulsion is one of the most promising branches of the broad Advanced Propulsion research field. Generally speaking, this architecture makes use of ionized gases (i.e. *plasmas*) as expellant to generate the propulsive thrust [38]. A plasma thruster is mainly composed by two stages: the plasma source and the acceleration stage. In the first, a neutral gas is injected and ionized using a number of techniques [14, 28]. The second stage, which may vary greatly between different technologies, accelerates the plasma to very high speed, in the order of tens of kilometers per second [29].

This high exhaust velocity leads to high specific impulse and constitutes the main advantage over conventional chemical rockets. [71] As biggest drawback, the thrust densities achieved by any electric propulsion device are orders of magnitude lower than those of the chemical engines for primary propulsion, limiting the applications to in-space operation [29].

Over the electric propulsion family, plasma propulsion shows higher thrust densities [38] and is suitable to be scaled to high power, opening the possibility of using this kind of device for highly efficient interplanetary transfer, even shortening the transfer time with respect to the most powerful chemical systems [37]. Moreover, the expelled plasma is neutral at scales greater than the Debye length [38] and no neutralizing system is required. This greatly increases the lifetime of the propulsive system since it removes the

most life-limiting component of electric thrusters [29, 76].

Within this framework, we can classify the plasma propulsion systems in two families: electromagnetic and electrothermal. In the first, the plasma is accelerated using electromagnetic fields either in steady [28] or in pulsed regimes [13]. In this group we find, for example, the Magnetoplasmadynamic thrusters (MPD).

An electrothermal plasma thruster, instead, uses electromagnetic fields to heat the plasma, while the acceleration takes place in a Magnetic Nozzle (MN) placed downstream [58], in analogy with other thermal propulsion systems. Variable Specific Impulse Magnetoplasma Rocket (VASIMR) [37, 58] and Helicon [12, 48] thrusters follow this paradigm. The absence of electrodes, often identified as the life-limiting components of other electric propulsion systems [76], and the ability to scale to high power [58] make MNs a desirable choice as acceleating stages for previously ionized gaseous propellants. Moreover, thermal plasma propulsion has been found to have high flexibility and applications range from micropropulsion systems for cubesat [50] to proposed fusion rockets [61, 62]. Beyond space propulsion, magnetic nozzles have been implemented for other fields of application, such as plasma surface processing [32, 60, 66] and fundamental physics experiment [20]

Understanding the physics underlying Magnetic Nozzles is of fundamental importance for the future of the thermal plasma propulsion. One of the most limiting factor of these devices is the tendency of the plasma to remain tight to the magnetic field lines, [9, 31, 56] necessarily closed on themselves. The result is an highly divergent plume, which yield to high thrust losses and performances lower than expected [3, 58].

Recently, Schmit and Fisch [65] proposed to introduce an azimuthal current at the nozzle throat to focus the jet and favor the separation. For solving the modified flow, Schmit and Fisch expanded Hooper's [31] model of cold plasma and showed the beneficial effect of their hypothesis. However, Ahedo and Merino [3] later showed that some of the hypotheses used by Hooper's model strongly reduces the understanding of the plasma expansion in magnetic nozzles. Therefore, we wish to translate Schmit's and Fisch's idea in a more comprehensive finite-temperature model, to understand the physics of the theorized collimation process and to assess its effect on the propul-

sive performance of the nozzle. Moreover, we wish to experimentally verify this positive effect, which, if confirmed, could open a novel architecture for MN-based thrusters.

1.2 Thesis Outline

This thesis is organized as follows. In Chapter 2 the fundamental physics governing plasmas is revised, and the theoretical models explained together with the respective domains of validity. In the same Chapter, the magnetic nozzles are described, the main properties and problematics explained and the current state-of-the-art research outlined. In the following Chapter 3, we assess the swirl-induced forces and we provide a quasi-one dimensional formulation for the expansion in MN under the regime previously discussed. Then, in Chapter 4, a two-dimensional theoretical model is exposed and the flow in the MN is solved. In Chapter 5, the effect of on the nozzle performance is assessed and the most promising techniques for introducing the desired swirling velocity profile are outlined. Subsequently, the set up for a proof-of-concept experiment is described in Chapter 6 and the experimental results are discussed. Finally, some conclusions are drawn.

This thesis has been developed within the Electric Propulsion and Plasma Dynamics Laboratory (EPPDyL) of Princeton University, Princeton, NJ, USA, under the supervision of Prof. Edgar Y. Choueiri. This work has been supported by the scholarship "Tesi all'Estero 2012-2013" of Politecnico di Milano.

Chapter 2

Magnetic Nozzles Theory

2.1 Introduction

In this first Chapter, we briefly review the physical and mathematical models used to describe the dynamics of a generic plasma, focusing our attention on the applicability limits of each model. Then, we introduce the physics governing Magnetic Nozzles, we present the hypotheses of work used in later computations and we outline the current state-of-the-art of the science of Magnetic Nozzles.

2.2 Plasma Models

Generally speaking, a plasma is a system composed by a macroscopic number of particles in which the concentration of free charges is high enough to produce effects relevant for defining the behavior of the system itself [59].

A number of models can be used for describing the motion of plasmas. Firstly, since a plasma is a multi-body system, it is always possible to write the classical Newton dynamic equations for each particle, following the Lagrangian paradigm. Considering a fully ionized plasma with only electromagnetic external forces, we write:

$$\begin{cases} \dfrac{d\mathbf{x}_{i,a}}{dt} = \mathbf{v}_{\mathrm{i,a}} \\ m_a \dfrac{d\mathbf{v}_{\mathrm{i,a}}}{dt} = q_a \left(\mathbf{v}_{\mathrm{i,a}} \times \mathbf{B}(\mathbf{x}_{\mathrm{i,a}}, t) + \mathbf{E}(\mathbf{x}_{\mathrm{i,a}}, t) \right) \end{cases} , \tag{2.1}$$

where i counts the particles of the $a-th$ population. Maxwell's equations are used for completing the set, considering both self-generated and externally imposed fields. Thus, a self-consistent model is derived.

This model is extremely dense of information as is the basis of some numerical simulation methods (PIC, Particles In Cell). However, it requires to solve six differential equations for each particle, easily leading to huge system and poor physical understanding. Therefore, some other models have been developed for providing a more manageable description.

2.2.1 Kinetic Model

In the kinetic model, a distribution function $f_a(\mathbf{x}, \mathbf{v}, t)$ is defined for each population as the space-average of the microscopic distribution function. The result is the Boltzmann's equation for plasmas:

$$\frac{\partial f_a}{\partial t} + \mathbf{v} \cdot \frac{\partial f_a}{\partial \mathbf{x}} + \frac{q_a}{m_a} \left(\mathbf{v} \times \mathbf{B}(\mathbf{x}, \mathbf{t}) + \mathbf{E}(\mathbf{x}, \mathbf{t}) \right) \cdot \frac{\partial f_a}{\partial \mathbf{v}} = C_a \quad , \tag{2.2}$$

where we considered the same kind of external forces as for the particle description. As seen by the dependency of $f_a(\mathbf{x}, \mathbf{v}, t)$, the Boltzmann's equation is defined in the phase space. To complete the set, the space-averaged Maxwell's equations are used.

$$\begin{cases} \nabla \cdot \mathbf{E} = \dfrac{1}{\epsilon_0} \left(\rho_{\text{ext}} + \sum_a q_a \displaystyle\int_{-\infty}^{\infty} f_a d^3 v \right) \\ \nabla \cdot \mathbf{B} = 0 \\ \nabla \times \mathbf{E} = -\dfrac{\partial \mathbf{B}}{\partial t} \\ \nabla \times \mathbf{B} = \mu_0 \left(\mathbf{J}_{\text{ext}} + \sum_a q_a \displaystyle\int_{-\infty}^{\infty} \mathbf{v} f_a d^3 v + \epsilon_0 \dfrac{\partial \mathbf{B}}{\partial t} \right) \end{cases} , \tag{2.3}$$

here the effect of the plasma on the electromagnetic field is clear from the presence of internal charge and current densities.

Since a space average has been performed, this model loses its validity for describing phenomena with space-scale lower than the characteristic length of the averaging convolution integral.

2.2.2 Multi-Fluid Model

While the kinetic equation is far more manageable than the system (2.1), one may wish to deal with a set of equations that resemble the *fluid* nature of the plasma.

Thus, a fluid model can be derived by multiplying the Boltzmann's equation by a function $\psi(\mathbf{v})$ and then by performing the integration over the velocities. The resulting relations imply functions of space and time only.

By choosing the form of $\psi(\mathbf{v})$ as moments of $\mathbf{v}$, we can write the equations for the density, the momentum and the energy for the *a-th* population as

$$\begin{cases} \dfrac{dn_a}{dt} + n_a \nabla \cdot \mathbf{u}_a = S_a \\ m_a n_a \dfrac{d\mathbf{u_a}}{dt} = -\nabla P_a - \nabla \cdot \mathbf{\Pi}_a + q_a n_a \left(\mathbf{u}_a \times \mathbf{B} + \mathbf{E}\right) + \mathbf{R}_a \\ \dfrac{3}{2} n_a \dfrac{dT_a}{dt} = -\nabla \cdot \mathbf{Q}_a - P_a \nabla \cdot \mathbf{u}_a - \mathbf{\Pi}_a : \nabla \mathbf{u}_a - \mathbf{u}_a \cdot \mathbf{R}_a + \dfrac{1}{2} \displaystyle\int_{-\infty}^{\infty} C_a m_a v^2 d^3 v \end{cases} , \tag{2.4}$$

where n_a is the number density. $\mathbf{u}_a$ is the flow velocity field, P_a is the scalar pressure, $\mathbf{\Pi}_a$ is the viscous tensor, $\mathbf{R}_a$ is the inter-species collisional term, C_a is the Boltzmann collisional term, T_a is the temperature and $\mathbf{Q}_a$ is the thermal flux, each quantity referring to the *a-th* population.

As said, these equations are actually equations for *moments* of $f_a(\mathbf{x}, \mathbf{v}, t)$ and every equation requires to know the dynamics of the moments of higher order. Hence, we would need an infinite set to close the system and recover the same informative content of the Boltzmann's equation. Alternatively, we can close this set by means of Fick's equations, such as the Fourier's law for the heat flux and the Newton's law for the viscous tensor. Moreover, the quantities of each populations are defined over the whole volume domain, hence the fluids interpenetrate and interact with each through induced electromagnetic fields and collisions. Of course, the Maxwell's equations must be included to assure the self consistency of the model.

Since this model does not consider the velocity distribution of the particles, it is unable to model some phenomena based on the interaction of portion of the distribution function with external fields, such as Landau's damping or micro-instabilities. In most of the cases, a *quasi-neutrality* holds

everywhere in the domain for spatial scale larger than the Debye length. For a two-fluid plasma (electrons and singly charged ions), this assumption will lead to $n_e = n_i$.

2.2.3 Single-Fluid Model, the MagnetoHydroDynamics

By performing a mass-average of the multi-fluid description, it is possible to write a single set and to describe the plasma as a single fluid. The laws of the Magnetohydrodynamics (MHD) will read

$$\begin{cases} \dfrac{d\rho_m}{dt} + \rho_m \nabla \cdot \mathbf{u} = 0 \\ \rho_m \dfrac{d\mathbf{u}}{dt} = -\nabla P - \nabla \cdot \mathbf{\Pi} + (\mathbf{J} \times \mathbf{B} + \rho \mathbf{E}) \\ \dfrac{3}{2} n \dfrac{dT}{dt} = -\nabla \cdot \mathbf{Q} - P \ \nabla \cdot \mathbf{u} - \mathbf{\Pi} : \nabla \mathbf{u} - \mathbf{J} \cdot (\mathbf{u} \times \mathbf{B} + \mathbf{E}) \end{cases} , \tag{2.5}$$

where we distinguish the mass density ρ_m from the charge density ρ. For two-species plasmas in quasi-neutrality condition, the mass density ρ_m can be approximated as $\rho_m = (m_i + m_e)n \approx m_i n$. Therefore, the velocity $\mathbf{u}$ will be very well approximated by the ion velocity $\mathbf{u}_i$. The current density is $\mathbf{J} = en\,(\mathbf{u}_i - \mathbf{u}_e)$.

The application of MHD is limited for conditions in which the quasi-neutrality is strictly conserved and where the physics of the system do not excite different responses of the species constituting the plasma. Thus, for assuring the applicability of MHD, the frequency ω_{MHD} of any perturbation shall be lower than the lowest resonance frequency, generally identified with the ion cyclotron frequency, Ω_{ci}, and the characteristic length of the system L_{MHD} shall be greater than the highest characteristic length of the plasma, usually the ion Larmor radius $\rho_{\mathrm{L,i}}$ or the Debye length, λ_D.

$$\begin{cases} \omega_{\mathrm{MHD}} \ll \Omega_{\mathrm{ci}} \\ \\ L_{\mathrm{MHD}} \gg \rho_{\mathrm{L,i}}, \lambda_D \end{cases} . \tag{2.6}$$

Frozen-In Magnetic Field Lines The Generalized Ohm's law is a fundamental equation for the MHD and links the electric and magnetic fields to the current density. In the most commonly used form, this equation reads

$$\mathbf{E} + \mathbf{u} \times \mathbf{B} = \underline{\underline{\eta}}\mathbf{J} \quad , \tag{2.7}$$

where $\underline{\underline{\eta}}$ is the resistivity tensor of the plasma, proportional to the electron-ion collision frequency ν_{ei}. Thus, an *ideal plasma*, where binaries collisions are negligible, has zero resistiviy and the law will read

$$\mathbf{E} + \mathbf{u} \times \mathbf{B} = 0 \quad . \tag{2.8}$$

It can be proven easily [59] that eq. (2.8) leads to the conservation of magnetic flux in flow surfaces. In other words, magnetic and flow stream surfaces of an ideal plasma coincide. This phenomenon is referred to as *frozen-in magnetic field lines* and is of fundamental importance for Magnetic Nozzles, as explained in section 2.3.

2.3 Electron Driven Magnetic Nozzle

2.3.1 Introduction and Functioning Mechanism

A Magnetic Nozzle (MN) is a steady state propulsive device used for converting thermal energy to direct kinetic energy, much similarly to a De Laval nozzle for chemical propulsion systems. Magnetic nozzles are also known as asymmetric plasma mirrors.

While in conventional nozzles the flow is driven by the physical walls of a converging/diverging duct, in a magnetic nozzle the frozen-in plasma follows the magnetic surfaces created by a proper disposition of coils. Thus, the thermal plasma accelerates along the converging/diverging magnetic duct to high speeds, up to one order of magnitude higher than those achievable by chemical means, if the working plasma is properly energized [58].

The thrust is transmitted to the spacecraft thanks to the mutual interaction of the nozzle coil current and the azimuthal currents induced inside the plume.[46] Another component of the thrust comes the pressure on the backplate of the plasma source, or on an eventual magnetic mirror as in fig. 2.1.

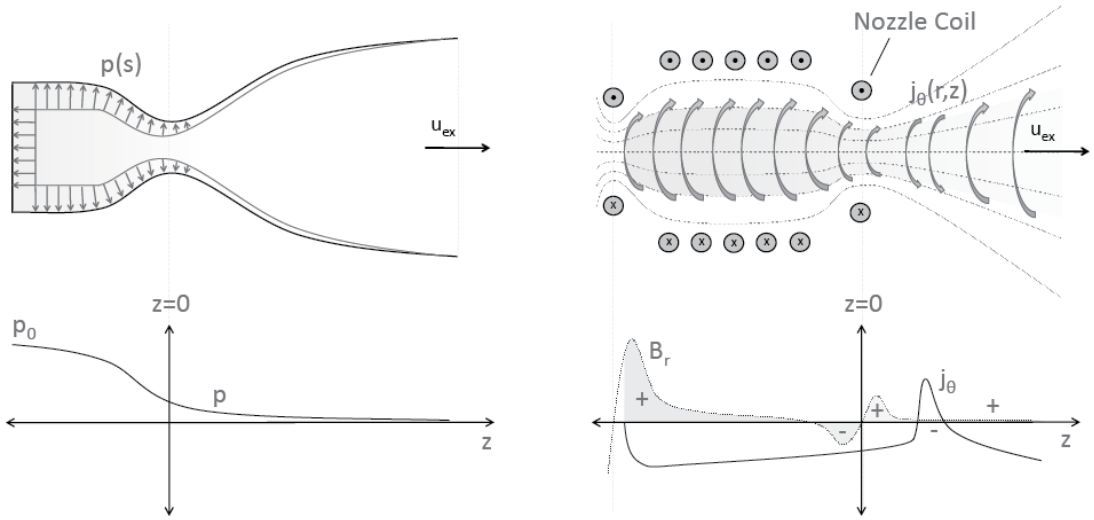

Figure 2.1: *Comparison between conventional nozzle (left) and magnetic nozzle (right) and the respective pressure and magnetic field and current density profiles [46].*

Generally speaking and for all purposes of this thesis, the plasma flowing in a MN is composed by electrons and singly charged ions. Some neutral particles are present due to incomplete ionization of the gas and background pressure. Since these neutrals are not affected by electromagnetic fields, they reduce the performance of the accelerating stage of the thruster. Is therefore clear that an high ionization rate is desirable for any electric propulsion system [29, 38].

For magnetic nozzle experiments, this high ionization rate is usually achieved using RF helicon plasma source, which showed higher efficiencies and longer lifetimes than other, more conventional discharge configurations [14, 39].

When the thermal energy is stored mainly in the electronic population ($T_e \gg T_i$), the functioning mechanism can be described as *thermal* for the electrons, and *electrostatic* for the ions. We call such devices Electron Driven Magnetic Nozzle (EDMN), recalling the definition given by Little and Choueiri.[49] In this class of magnetic nozzles, the thermal energy stored in the electrons drives them in a thermal expansion in the direction of the free end of the thruster, while the ions, much colder, tend to remain confined in the plasma source. Therefore, an ambipolar electric field arises for conserv-

ing local quasi-neutrality [3] and the ions are pulled by the electrons and accelerate outwards, generating most of the thrust in virtue of the high ion to electron mass ratio.

Using Hall thrusters as reference, we can intuitively describe the physics of the phenomenon as follows. In a hall thruster, the ions are accelerated by the electric field created by the electrons, magnetically confined at the channel edge [29]. Once the ions have left the accelerating chamber they have to be neutralized to avoid them from being braked by the same electrons that provided their acceleration. In an EDMN, on the contrary , the thermal energy of the electrons pushes them away from the thruster, selft-neutralizing the plume and removing the need of a neutralizing cathode.

2.3.2 Working Assumptions

We present here the most common assumptions lately used during our analysis of electron-driven magnetic nozzles, justifying each of them according to our working conditions. Other assumptions may be introduced in specific derivations, and will be described once they are presented the first time. In general, we will make use of a two-fluid model to describe the physics of the plasma in the mangetic nozzle.

Assumption 1: Negligible Electron Inertia A generally well accepted approximation neglects the electron inertia [3, 4, 6, 49]. Thus, the electrons are considered completely magnetized and their motion is constrained to the magnetic field surfaces. The ions velocity field, on the contrary, can separate from the magnetic field lines.

Effects of finite electron inertia have been studied by Ahedo and Merino [6] showing that, contrarily to previous beliefs [31], the electrons separate from the magnetic field lines in a divergent manner, thus reducing the efficiency of the nozzle. However, the same simulations show that these finite-electron-mass effects have limited importance on the performance of the EDMN [6].

Assumption 2: Isothermal Electrons and Cold Ions Another assumption for EDMN considers the electron flow to be isothermal and neglects

the thermal content of the ionic population. The first hypothesis recalls the high thermal conductivity of the electronic population along the magnetic surfaces of the nozzle [51] and contrasts with the flow of conventional rocket nozzles. A study [7] on an eventual non-isothermal expansion showed that a polytropic expansion reduces the performance of the nozzle and the isothermal case represents the upper boundary of the nozzle efficiency. The physical explanation directly comes from energetic consideration: in an adiabatic flow the total energy is limited to the initial value of enthalpy, while an isothermal flow shows an energy flux from the plasma source to the nozzle, increasing the total enthalpy content of the flow along the nozzle.

The ionic thermal content is usually neglected ($T_i \ll T_e$) since helicon plasma sources used for thermal plasma thrusters excite mainly the electronic population [39]. A remarkable exception is represented by the VASIMR concept, where a significant portion of thermal energy is carried by the ions since an ion cyclotron frequency heating mechanism is implemented between the helicon plasma source and the magnetic nozzle [8].

Assumption 3: Uncollisional, Inviscid Flow Being the inter-species collisions a phenomenon with negative outcome for the propulsive performance, we ideally wish to operate with quasi-collisionless plasmas [3]. Therefore, we will use an uncollisional formulation for the equations governing the magnetic nozzle. However, this hypothesis will be relaxed when computing the conditions at the nozzle throat, where the highest plasma density is recorded, and the collisions are of great importance.

Assumption 4: Low-Beta Regimes A generally accepted simplifying hypothesis of work for MNs makes use of the so-called $low-\beta$ plasma regime [3, 49]. Recalling the definition of β:

$$\beta = \frac{P}{P_{\text{mag}}} = \frac{nk_bT}{B^2/2\mu_0} \quad , \tag{2.9}$$

we get that $\beta \ll 1$ implies that the applied magnetic field is always much greater than any induced field in the plasma. This allows to decouple the magnetic field soution to the plasma dynamics, greatly simplifying the computations. Generally, from a low-β approximation is possible to compute the

complete finite-β solution by means of an iterative method.[5, 44]

Assumption 5: Steady State In their operational regime, MNs are typically steady-state devices, thus we will model the flow in such magnetic duct as steady state, with all unsteady phenomena already faded out.

Assumption 6: Axisymmetry The axisymmetry of the problem suggests to use cylindrical coordinates (r, ϑ, z), dropping the azimuthal derivatives: $\partial/\partial\vartheta = 0$. Given a vectorial field $\mathbf{v}$, we will decompose it into its meridional and azimuthal components: $\mathbf{v} = \tilde{\mathbf{v}} + v_\theta \hat{\vartheta}$.

According to this hypothesis, we introduce the magnetic intrinsic tern $(\mathbf{b}, \mathbf{n}, \mathbf{t})$ defined as in fig. 2.2.

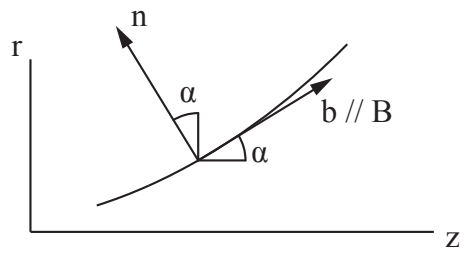

Figure 2.2: *Magnetic intrinsic tern in the divergent section of the nozzle.*

Assumption 7: Magnetic Field Topology For comparing the results of the present analysis to previous works and experimental results, we adopt the simple single-loop magnetic field topology for the divergent part of the magnetic nozzle, as in fig. 2.3. While this configuration may lead to non-optimal expansion, whose existence is still under debate [49], it has been adopted for all the previous studies and allow treatable analytical expressions for streamlines and magnetic iso-gradient surfaces, which will become useful in the analytical approximation of the nozzle flow.

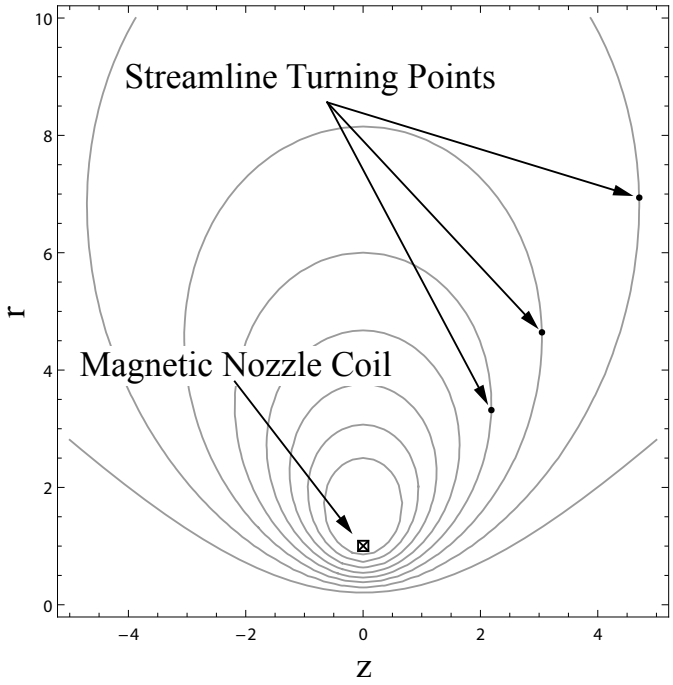

Figure 2.3: *Projection on the meridional (r, z) plane of the magnetic field streamlines induced by a single coil located in $r = 1$, $z = 0$.*

2.3.3 Governing Equations

Using the subscripts e and i for electrons and ions respectively and keeping the electron mass, the governing equations in steady state read:

$$\begin{cases} \nabla \cdot (n\tilde{\mathbf{u}}_\mathbf{i}) = 0 \\ \nabla \cdot (n\tilde{\mathbf{u}}_\mathbf{e}) = 0 \\ m_i n(\tilde{\mathbf{u}}_\mathbf{i} \cdot \nabla)\tilde{\mathbf{u}}_\mathbf{i} = -en\nabla\phi + enu_{\theta\mathrm{i}}B\hat{\mathbf{n}} + nm_i\dfrac{u_{\theta\mathrm{i}}^2}{r}\hat{\mathbf{r}} \\ m_e n(\tilde{\mathbf{u}}_\mathbf{e} \cdot \nabla)\tilde{\mathbf{u}}_\mathbf{e} = -\nabla P_e + en\nabla\phi - enu_{\theta\mathrm{e}}B\hat{\mathbf{n}} + nm_e\dfrac{u_{\theta\mathrm{e}}^2}{r}\hat{\mathbf{r}} \\ m_i n(\tilde{\mathbf{u}}_\mathbf{i} \cdot \nabla)ru_{\theta\mathrm{i}} = en(\tilde{\mathbf{u}}_\mathbf{i} \times \mathbf{B}) \cdot r\hat{\vartheta} \\ m_e n(\tilde{\mathbf{u}}_\mathbf{e} \cdot \nabla)ru_{\theta\mathrm{e}} = -en(\tilde{\mathbf{u}}_\mathbf{e} \times \mathbf{B}) \cdot r\hat{\vartheta} \\ \nabla P_e = T_e\ \nabla \ln(n) \end{cases} , \qquad (2.10)$$

where all symbols are conventional. These equations must be correlated by the steady state Maxwell's equation for closing the system, considering the quasi neutrality condition $n_i = n_e$.

$$\begin{cases} \nabla^2 \phi = 0 \\ \nabla \cdot \mathbf{B} = 0 \\ \nabla \times \mathbf{B} = \mu_0 \mathbf{J}_{\text{ext}} \end{cases} . \tag{2.11}$$

The negligible electron inertia and low-β assumptions would allow to drop m_e and the induced currents term in Ampère's law, respectively.

2.3.4 Plasma Detachment Theories

Despite the promises of the magnetic nozzles, these devices are not exempt from physical and technical problems. The most significant drawback comes from the same frozen-in condition of the plasma. Indeed, since the magnetic field lines forming the magnetic nozzle are closed, the plasma tends to diverge from the nozzle axis, following the applied field [9].

Eventually, a separation between the plasma and the magnetic field occurs, as shown by simulations [3, 5, 6] and experiments [21] , but the plume shows a high divergence at the expenses of the nozzle efficiency [3, 49]. However, how and where this separation occurs is still an open point of research. A number of theories on separation mechanism have been developed for describing the phenomenon. Specifically, it has been theorized that cross-field diffusion occurs due to resistivity [56], electron inertia [31], magnetic stretch [9] , demagnetization and cross-field electrostatic gradients [4].

However, the first mechanism seems to be too weak to predict the observed cross-field diffusion [4] and the second has been recently questioned by simulations by Ahedo and Merino [6]. The magnetic stretch [9] theory predicts that the transition of the plasma flow from sub to super-alfvenic would demagnetize the flow, freeing it from the influence of the applied magnetic field. This transition should occur for the combination of plasma acceleration inside the nozzle and applied field weakening, as the flow travels far from the nozzle throat. This theory found some experimental agreement in

predicting the location of plume detachment [21], but its validity is discussed since it should lead to divergent separation [4], in opposition to experimental observation[21] and simulations [3, 43], and the predicted stretch of the magnetic field lines to the infinite has not been observed [58].

The demagnetization theory [4], on the other hand, leads to convergent detachment due to the contemporary weakening of the magnetic field and acceleration of the plume. The combined action of these two phenomena in the far-field plume region eventually leads to the demagnetization of electrons and to their separation from magnetic streamlines [5]. This demagnetization is measured by the ratio l_e/L_∇, where l_e is the electron gyroradius and L_∇ is the characteristic length of magnetic field variation. However, simulations [6] with non-zero electron inertia show that, due to isorotation of the electronic flow, the electron separation is divergent rather than convergent, in opposition to the prediction of this electron demagnetization theory.

Finally, another proposed convergent detachment mechanism relies on the low magnetization of ions, common to most of the magnetic nozzle applications [45]. In such plasma flows, the ionic inertia and the low magnetization reduces the tendency of ions to follow the magnetic streamline, while the much lighter electrons would remain attached to the magnetic stream surfaces. Thus, a cross-field ambipolar electric field arises [4] Consequence of such separation mechanism is the induction of meridional currents, observed in some simulations [3].

Other problems affecting MNs-based thrusters are poor thermal-kinetic power conversion efficiency [2] at low power and magnetic field, and poor ionization.

Chapter 3

Effects of Swirling Motion in Magnetic Nozzles

3.1 Introduction

In this Chapter, we start to introduce a theoretical framework for the description of the governing physics of an Electron-Driven Magnetic Nozzle under the hypothesis of significant azimuthal motion of the species. First, we discuss the influence of such a motion on the equations in a two-fluid model. Then, a quasi-one dimensional formulation is presented and its validity discussed, leading to useful consideration for the subsequent Chapters.

3.2 Swirling Induced Forces

3.2.1 Momentum Equations

We start the assessment of the effect of the swirling motion by taking the momentum equations for the generic *a-th* species of a plasma in motion in a diverging magnetic field.

As already explained in section 2.3.2, axisymmetry holds everywhere, therefore $\partial / \partial \vartheta = 0$, and the plasma is low-Beta ($\beta \ll 1$), thus the induced magnetic field can be neglected. No external electric field is applied. The assumptions of quasi neutrality, isothermality of electrons and negligible ion thermal content are not required in this first section.

In cylindrical coordinates $(\hat{\mathbf{r}}, \hat{\vartheta}, \hat{\mathbf{z}})$, a generic vectorial quantity $\mathbf{v}$ can be decomposed into a meridional and an azimuthal components: $\mathbf{v} = \tilde{\mathbf{v}} + v\ \hat{\vartheta}$. The momentum equations for the *a-th* species are [3]

$$m_a(\tilde{\mathbf{u}}_\mathbf{a} \cdot \nabla)\tilde{\mathbf{u}}_\mathbf{a} = -\frac{1}{n_a}\nabla P_a - q_a \nabla\phi + q_a u_{\theta\mathrm{a}} B\hat{\mathbf{n}} + m_a \frac{u_{\theta\mathrm{a}}^2}{r}\hat{\mathbf{r}} \quad , \tag{3.1}$$

$$m_a(\tilde{\mathbf{u}}_\mathbf{a} \cdot \nabla) r u_{\theta\mathrm{a}} = q_a(\tilde{\mathbf{u}}_\mathbf{a} \times \mathbf{B}) \cdot r\hat{\vartheta} \quad , \tag{3.2}$$

where $\hat{\vartheta}$ is the azimuthal unit vector and $\hat{\mathbf{n}}$ is a unit vector normal to the magnetic field oriented as in fig. 3.1.

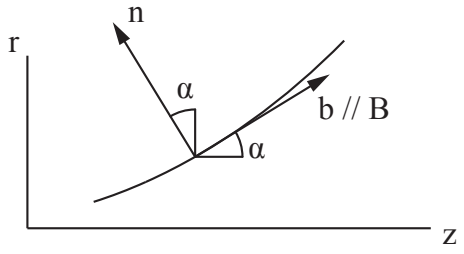

Figure 3.1: *Magnetic intrinsic tern in the divergent section of the nozzle.*

We introduce the magnetic streamfunction ψ, defined by the relation

$$\mathbf{B} = \frac{1}{r}(\hat{\vartheta} \times \nabla\psi) \quad , \tag{3.3}$$

for describing the magnetic field in the momentum equations. The magnetic field has components

$$\mathbf{B} = \begin{pmatrix} -\frac{1}{r}\frac{\partial\psi}{\partial z} \\ 0 \\ \frac{1}{r}\frac{\partial\psi}{\partial r} \end{pmatrix} \quad , \tag{3.4}$$

and the azimuthal momentum equation becomes the conservation of angular momentum along the streamline of the *a-th* species [3]:

$$r m_a u_{\theta\mathrm{a}} + q_a\psi = R^0 m_a u_{\theta\mathrm{a}}^0 + q_a\psi^0 \quad , \tag{3.5}$$

where the superscript *0* indicates the reference (e.g. throat plane) conditions. Through eq. (3.5) we can relate the azimuthal velocity $u_{\theta\mathrm{a}}$ to the current

position on the streamline and its value on the throat plane.

$$u_{\theta \mathrm{a}} = \frac{R^0}{r} u^0_{\theta \mathrm{a}} + \frac{q}{r m_a}(\psi^0 - \psi) \quad . \tag{3.6}$$

From eq. (3.1) we see that the motion of the *a-th* species depends on its swirling velocity $u_{\theta \mathrm{a}}$ in the term:

$$\mathbf{F}^{\theta}_{\mathbf{a}} = q_a u_{\theta \mathrm{a}} B \hat{\mathbf{n}} + m_a \frac{u^2_{\theta \mathrm{a}}}{r} \hat{\mathbf{r}} \quad , \tag{3.7}$$

which is the vectorial sum of the Lorentz and the centrifugal forces. It is clear how the direction of the Lorentz force depends on the mutual sign of q_a and $u_{\theta \mathrm{a}}$, while the centrifugal push is always directed away from the nozzle axis (i.e. in the $+r$ direction).

From the analysis of eq. (3.7) is possible to derive some conditions by which the swirling motion is favorable for the propulsive performances of the escaping plume. In other words, we want to find the regime of $u^0_{\theta \mathrm{a}}$ by which the force $\mathbf{F}^{\theta}_{\mathbf{a}}$ collimates (focuses) and accelerates the plasma in the magnetic nozzle.

3.2.2 Focusing Condition

The focusing condition can be derived by imposing the radial component of $\mathbf{F}^{\theta}_{\mathbf{a}}$ to be negative:

$$F^{\theta}_{a\, r} = q_a B_z u_{\theta \mathrm{a}} + m_a \frac{u^2_{\theta \mathrm{a}}}{r} < 0 \quad . \tag{3.8}$$

Substituting eq. (3.6) into (3.8) and solving the inequality for $u^0_{\theta \mathrm{a}}$ assuming $q_a > 0$, we get

$$-\left(\frac{q_a}{m_a R^0_a} \left(B_z r^2 + 2 \left(\psi^0 - \psi \right) \right) \right) < u^0_{\theta \mathrm{a}} < 0 \quad , \tag{3.9}$$

which means that the angular frequency of the streamline at the throat, $\omega^0_a = u^0_{\theta \mathrm{a}} / R^0_a$, is bounded by

$$-\Omega_z \frac{r^2}{R^{0\,2}_a} - 2 \frac{q_a}{m_a R^{0\,2}_a} \left(\psi^0 - \psi \right) < \omega^0_a < 0 \quad , \tag{3.10}$$

where Ω_z is the local cyclotron frequency magnitude of the *a-th* species, computed with B_z. We can specialize the equations for a two species (electrons and ions) plasma. In this situation, we know that $\psi^0 - \psi \geq 0$ for the

ions, due to their inward separation from the magnetic streamlines [3], and $\psi^0 - \psi \approx 0$ for the electrons [6], due to their high magnetization. Therefore, since $r \geq R^0$ along all the divergent streamline, the strictest condition is found at the nozzle throat, which is

$$\begin{cases} -\Omega_i^0 < \omega_i^0 < 0 \\ \\ 0 < \omega_e^0 < \Omega_e^0 \end{cases} . \tag{3.11}$$

If these inequalities are met, the Lorentz component of $F^{\theta}_{a\,r}$ dominates over the centrifugal force, leading to a net collimating effect.

Extending the collimation analysis further in plume would require to consider the full set of equations for each species. Is has been observed by simulations [6] that an electron swirl at the nozzle throat would lead to a divergent separation of the electron fluid from the magnetic streamline. This can be seen as conseguence of the isorotational theorem, [25] that leads the electron to azimuthally accelerate while moving along the divergent electron streamline. In this case, the velocity would eventually exceed the limits given by eq. (3.9) and the electron fluid would diverge even more from the magnetic streamtube. However, Ahedo and Merino showed [6] that the consequent reduction of nozzle efficiency is rather low due to the limited ion density at the plume edge.

Little and Choueiri [49] noted that the ion-magnetic and electron-magnetic separation angles never exceed some degrees. Therefore, the derivatives of the quantities along the flow and magnetic streamlines are almost equal since $\mathbf{b} \cdot \tilde{\mathbf{s}} = cos(\alpha) \sim 1$. Making use of the such a hypothesis, we can simplify eq. (3.9) and solve for r to find the regions of net collimation:

$$r > R_a^0 \sqrt{-\left(\frac{q_a}{|q_a|}\right)\frac{\omega_a^0}{\Omega_a^0}} \quad . \tag{3.12}$$

Since along the streamline $r \geq R^0$, the inequality implies $|\omega_a^0| < \Omega_{\mathrm{a}}^0$ and opposite in sign to q_a, which is equivalent to eq. (3.11). If these conditions are met, then $F^{\theta}_{i\,r} < 0$ along all the streamline.

3.2.3 Acceleration Condition

The accelerating condition is derived by imposing

$$F^{\theta}_{a\,z} = -q_a B_r u_{\theta \mathrm{a}} > 0 \quad , \tag{3.13}$$

which leads to the simple and less restrictive condition

$$-\frac{q_a}{|q_a|} u_{\theta \mathrm{a}} > 0 \quad , \tag{3.14}$$

or, in quasi field aligned hypothesis,

$$-\frac{q_a}{|q_a|} \omega_a^0 > 0 \quad . \tag{3.15}$$

Due to the topology of the magnetic field in the nozzle, it can be observed that the magnitude of this component of the Lorentz force is usually lower than the radial part up to the point where the magnetic field steep overcome $\pi/4$ radians. However, for most of initial conditions this condition occurs far in the plume, where the decrease of the magnetic field is already relevant [49]. Thus, we could conclude that the main effect of the species swirling is radial, focusing or de-focusing depending on the azimuthal velocity magnitude and sign.

Finally, it is clear that a differential rotation of the species according to their sign is required for the insurgence of a net current, or the Lorentz forces due to the different species would mutually cancel out, leaving only the always de-focusing centrifugal term.

3.2.4 Effects on Flow Meridional Curvature

As another approach to look at the same phenomenon, we can analyze the effect of the swirling on the meridional flow curvature, which is $\kappa = 1/R_c$ where R_c is the local radius of curvature of the meridional flow streamline $\tilde{\mathbf{s}} \parallel \tilde{\mathbf{u}} \approx \tilde{\mathbf{u}}_{\mathbf{i}}$

We can assess this analysis from the mass-averaged sum of the momentum equation of the two populations, neglecting the electron inertia in the convective derivative:

$$n m_i (\tilde{\mathbf{u}}_{\mathbf{i}} \cdot \nabla) \tilde{\mathbf{u}}_{\mathbf{i}} = -\nabla P + qn \left(u_{\theta \mathrm{i}} - u_{\theta \mathrm{e}}\right) B \hat{\mathbf{n}} + \frac{n}{r} \left(m_i u_{\theta \mathrm{i}}^2 + m_e u_{\theta \mathrm{e}}^2\right) \quad , \tag{3.16}$$

which can be rearranged using the magnetic intrinsic tern $(\hat{\mathbf{b}}, \hat{\mathbf{n}}, \hat{\vartheta})$ and the dual flow meridional intrinsic tern $(\hat{\mathbf{s}}, \hat{\mathbf{p}}, \hat{\vartheta})$

$$\frac{\partial \tilde{u}_i}{\partial s}\hat{\mathbf{s}} = -\frac{\nabla P}{n m_i \tilde{u}_i} + \frac{\Omega_i}{\tilde{u}_i}\left(u_{\theta \mathrm{i}} - u_{\theta \mathrm{e}}\right)\hat{\mathbf{n}} + \left(u_{\theta \mathrm{i}}^2 + \frac{m_e}{m_i}u_{\theta \mathrm{e}}^2\right)\frac{\hat{\mathbf{r}}}{\tilde{u}_i\, r} - \frac{\tilde{u}_i}{R_c}\hat{\mathbf{p}} \quad . \tag{3.17}$$

Thus, the curvature can be derived from the dot product of eq. (3.17) with $\hat{\mathbf{p}}$. We can simplify the expression by considering small electron-ion meridional divergence angle, which leads to $\cos\left(\tilde{\alpha}_{\mathrm{ei}}\right) \approx 1$. This hypothesis well approximate the actual separation up to fairly high angles, like the quasi-field aligned assumption. Thus, the curvature κ will be

$$\kappa = -\frac{\nabla P \cdot \hat{\mathbf{p}}}{n m_i \tilde{u}_i^2} + \frac{\Omega_i}{\tilde{u}_i^2}\left(u_{\theta \mathrm{i}} - u_{\theta \mathrm{e}}\right) + \frac{\cos(\tilde{\alpha})}{r}\frac{u_{\theta \mathrm{i}}^2 + \dfrac{m_e}{m_i}u_{\theta \mathrm{e}}^2}{\tilde{u}_i^2} \quad , \tag{3.18}$$

In the first term of the right-hand side of eq. (3.18), we see the transverse pressure $-\nabla P \cdot \hat{\mathbf{p}}$ tending to expand radially the jet and counteracted by the meridional inertia. The second and third terms are the Lorentz force, clearly mass-independent and stronger for high magnetization (Ω_i), and and the centrifugal effect, where the electron centrifugal effect is reduced by the mass ratio $m_e/m_i \ll 1$.

From the same eq. (3.18), imposing the swirl-dependent terms to be negative, we can find again the condition of eq. (3.11). We can also find the condition of maximum effect of the swirling motion by applying the derivative to the two swirl-dependent terms of eq. (3.18) with respect to the azimuthal velocity of each species. Imposing the derivative to be equal to zero, we get that the condition of maximum effect is achieved for

$$\begin{cases} u_{\theta \mathrm{i}}\big|_{F^{\theta}_{\mathrm{i\,r\,,\,max}}} = -\dfrac{1}{2}\dfrac{\Omega_i r}{\cos(\tilde{\alpha})} = \dfrac{1}{2}u_{\theta \mathrm{i,max}} \\ u_{\theta \mathrm{e}}\big|_{F^{\theta}_{\mathrm{e\,r\,,\,max}}} = \dfrac{1}{2}\dfrac{\Omega_e r}{\cos(\tilde{\alpha})} = \dfrac{1}{2}u_{\theta \mathrm{e,max}} \end{cases} , \tag{3.19}$$

where $u_{\theta \mathrm{i,max}}$ and $u_{\theta \mathrm{e,max}}$ are the maximum allowed azimuthal velocities according to the condition of eq. (3.11).

3.3 Quasi-One Dimensional Flow Model

Thanks to their relative simplicity, quasi-one dimensional models are widely used in rocket nozzles theory [71] for describing the behavior of cross section-averaged quantities such as density and Mach number. The same approach has been introduced also in Magnetic Nozzles [18] and their accuracy has been proved also by recent simulations [3, 6, 49] based on more complex multi dimensional models.

Therefore, it is natural for us to start from a quasi-one dimensional modeling of the magnetic nozzle for studying the flow under our condition of relevant azimuthal motion.

3.3.1 Quasi 1D Equations

Before writing the governing equation for the quasi-one dimensional model and to get general and scalable results, we nondimensionalize the quantities involved. The reference quantities are the nozzle throat radius r_e, the sonic speed c_s and the ion mass m_i. The expansion is isothermal, according to the hypothesis of section 2.3.2, thus c_s is constant throughout the nozzle.

$$\begin{cases} dz = r_e dz' \\ u_z = c_s M_z \\ u_\theta = c_s M_\theta \\ A = r_e^2 \end{cases} . \tag{3.20}$$

We define also $\Psi'_z(z)$ as the non dimensional derivative of the magnetic stream coordinate ψ

$$\Psi'_z(r,z) = \frac{c_s r_e}{m_i} \frac{\partial \psi(r,z)}{\partial z} \quad . \tag{3.21}$$

The governing equation reads

$$\left(1 - \frac{1}{M_z^2}\right) \frac{dM_z}{dz} = \frac{1}{AM_z} \frac{dA}{dz} + S(z) + L(z) \quad , \tag{3.22}$$

where S(z) and L(z) are the kinetic energy recovery and the is the axial

Lorentz force terms, respectively.

$$S(z) = -\frac{1}{M_z}\frac{d}{dz}\left(\frac{1}{A}\int_A \frac{1}{2}M_{\theta \mathrm{i}}^2 dA\right) \quad , \tag{3.23}$$

$$L(z) = \frac{1}{M_z}\int_A \left(M_{\theta \mathrm{i}} - M_{\theta \mathrm{e}}\right)\Psi'_z(z)dA \quad . \tag{3.24}$$

As clear from eq. (3.22), a relation for each azimuthal velocity has to be introduced to close the system. We will use the quasi-field aligned hypothesis and the conservation of angular momentum to state that

$$\begin{cases} ru_{\theta i} = H_i(R^0) \\ \\ ru_{\theta e} = H_e(R^0) \end{cases} \quad . \tag{3.25}$$

Thus, the integrals in eq. (3.23) and (3.24) are functions of z only, as required for a quasi-one dimensional modeling. We observe from eq. (3.22) that in a quasi-one dimensional model it is not possible to see bidimensional effects such as the collimating action of $\mathbf{F}^{\theta}_{\mathrm{i,e}}$. Moreover, as will be described in section 4.2, the introduction of an imposed swirling velocity profiles in each species may arise mathematical and physical inconsistencies in the radial equilibrium of the plasma flow. However, since the quasi-one dimensional description focuses on the axial behavior only, the mean by which such a swirl is introduced does not affect the final results.

3.3.2 Sonic Condition

One of the basic concept of the theory of converging-diverging nozzles for rocket propulsion is that the flow achieves sonic condition, that is $M_z = 1$, at the nozzle throat, where $dA/dz = 0$ [71]. This condition has also been observed in Magnetic Nozzles [18, 58]. Thus, we think it is straightforward to investigate whether the swirling regime modifies the sub-to-supersonic transition. To do so, we analyze the behavior of eq. (3.22) at the nozzle throat. First, we note that in a converging duct the conservation of angular momentum in quasi-field aligned regime requires the swirling velocity to increase linearly with the reduction of the radius. This leads to the increase of the swirling kinetic energy and to a negative swirling term $S < 0$. On the other

hand, in a diverging duct the swirling term is positive and contributes to the increase of the Mach number $S > 0$. We can conclude that, at the throat, the swirling term must change sign, or S = 0. We also note that the Lorentz term follows the same trend and is null the throat, where the Lorentz force is totally radial. Thus, the Mach eq. (3.22) reduces to

$$\left(1 - \frac{1}{M_z^2}\right) \frac{dM_z}{dz} = 0 \quad . \tag{3.26}$$

Since in general $dM_z/dz \neq 0$, we get $M_z = 1$, which means that the sonic velocity is achieved at the nozzle throat, as in conventional De-Laval nozzles. However, the flow properties (e.g. critical-to-total pressure ratio) may differ since the plasma is slowed down by the Lorentz force and the conversion of part axial kinetic energy into swirling energy for angular momentum conservation.

3.3.3 Results and Discussion

We can now solve the quasi-one dimensional equation in a representative case. From eq. (3.22), we see that the electrons influences the flow only in the Lorentz term, while the ions in both the kinetic energy recovery. Therefore, we choose to start by looking at the case of ion motion and still electrons. By using common values for magnetic field and electron temperature [48], and Argon as propellant, we get nondimensional ion and electron cyclotron frequencies of $\Omega_i = 1.3206$ and $\Omega_e = 82160$, respectively. We impose a swirling profile to the ions as $u^0_{\theta \mathrm{i}} = \omega^0_i r$, where $\omega^0_i = -0.5$ and we plot in fig. 3.2 the Mach number in the swirling and in the reference, non-swirling, case. For this analysis, the nozzle geometry described in section 2.3.2 has been used for determining the area law $A(z)$.

As clear from fig. 3.2, the two cases are indistinguishable and no relevant effect is felt by the plasma expansion in the magnetic nozzle even if the imposed ω^0_i is very close to the optimal value dictated by eq. (3.19). We can also plot the right-hand side terms of eq. (3.22) to identify the most relevant non-dimensional forces in this case.

We see from fig. 3.3 that all the axial components of the swirling-related terms are about two orders of magnitude lower than the thermal expansion,

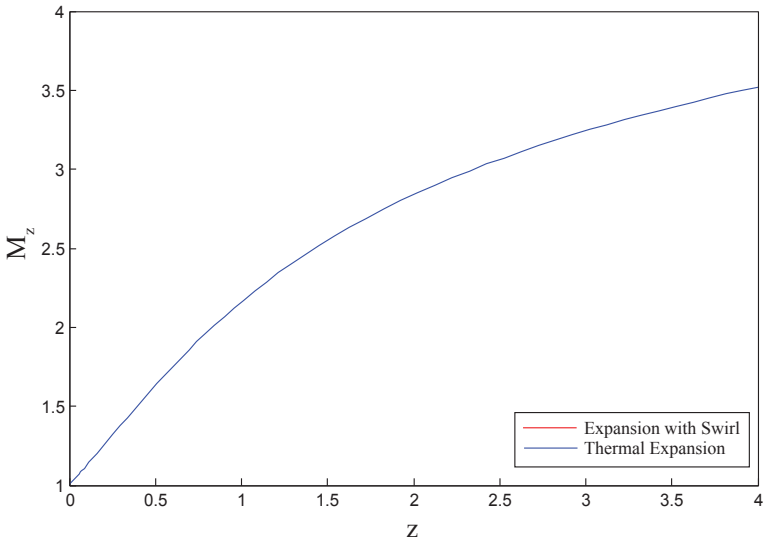

Figure 3.2: *Axial Mach number in the divergent portion of quasi-one dimensional magnetic nozzle flow. Ion throat swirl frequency* $\omega_i^0 = -0.5$*, electron throat swirl frequency* $\omega_e^0 = 0$*. Nondimensional ion cyclotron frequency* $\Omega_i = 1.3206$*, corresponding to argon ions in* $450\ G$ *magnetic field and* $cs = 4108\ m/s$*. Nondimensional electron cyclotron frequency* $\Omega_e = 82160$*.*

clearly explaining why the swirled flow shows no relevant difference with respect to the reference case. However, the radial term of the Lorentz force, computed according to

$$L_r(z) = \frac{1}{M_z} \int_A \left(M_{\theta \mathrm{i}} - M_{\theta \mathrm{e}}\right) \Psi_r'(z) dA \quad , \tag{3.27}$$

is one order of magnitude higher than any radial swirl-induced term.

If we choose to swirl the electrons to the frequency $\omega_e^0 = 500$ (much higher than the ionic case, but still well below Ω_e), we get the results reported in fig. 3.4. From fig. 3.4(a), we see a clear difference between the swirled and the non-swirled regimes. In the swirled case, a stronger acceleration of the plume takes place in the first part of the divergent section, as clear also from fig. 3.4(b). After some throat radii, the Lorentz force and kinetic energy recovery vanish, leaving only the thermal expansion to further accelerate the flow, thus the two profiles become more and more parallel to each other.

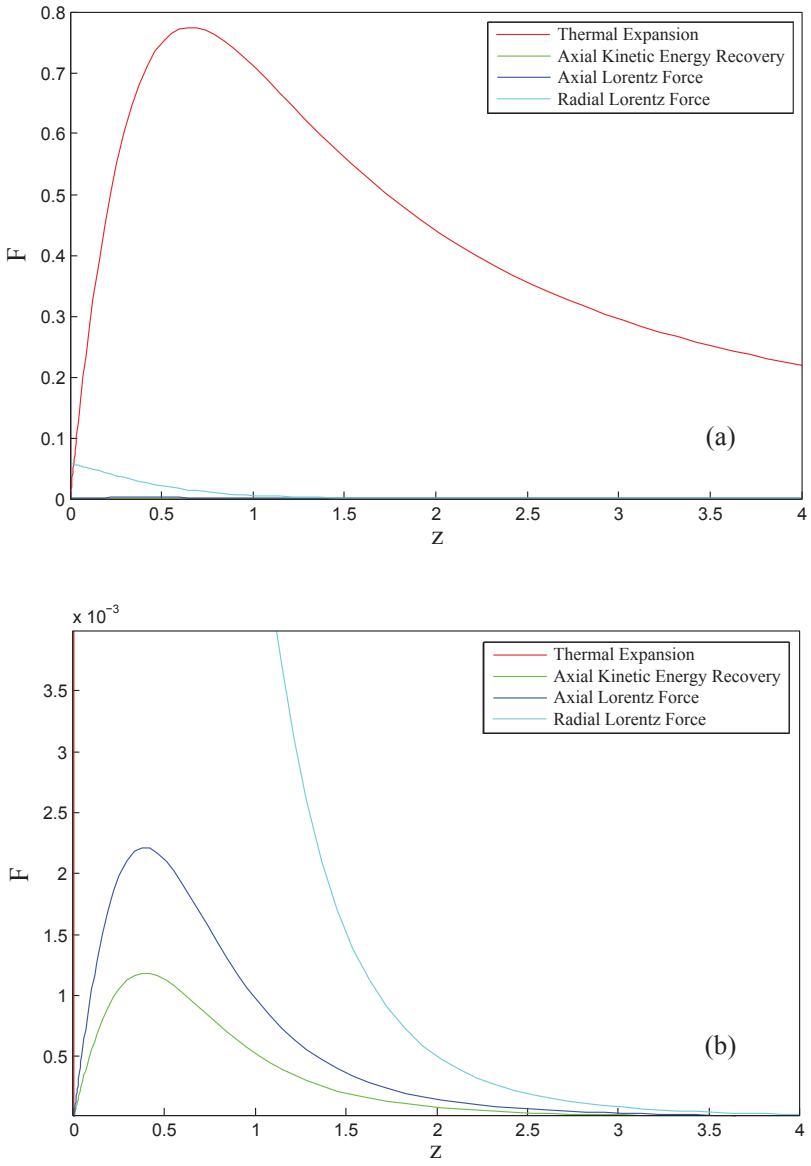

Figure 3.3: *Nondimensional force terms acting in the divergent portion of quasi-one dimensional magnetic nozzle flow. The fig. (b) is a focus of fig. (a) to show the non-pressure terms. Ion swirl frequency* $\omega_i^0 = -0.5$*, electron swirl frequency* $\omega_e^0 = 0$*. Nondimensional ion cyclotron frequency* $\Omega_i = 1.3206$*, corresponding to argon ions in* $450\ G$ *magnetic field and* $c_s = 4108\ m/s$*. Nondimensional electron cyclotron frequency* $\Omega_e = 82160$*.*

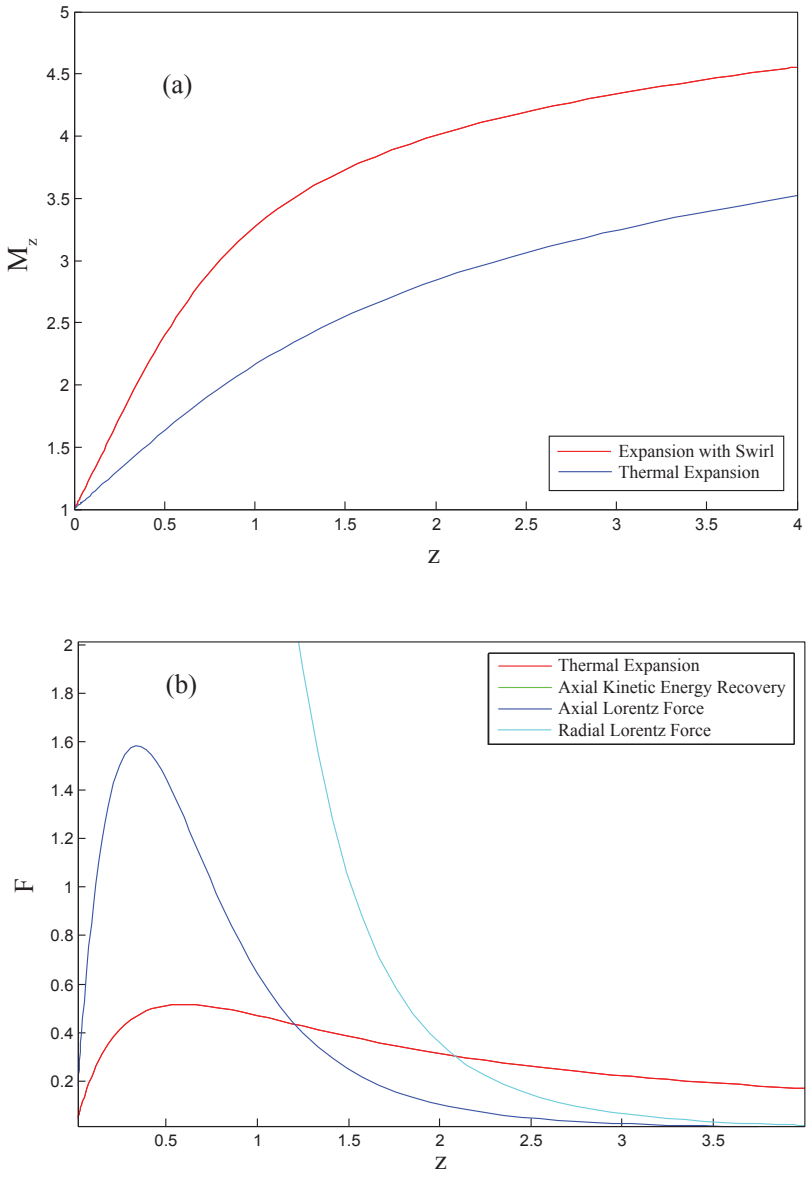

Figure 3.4: *Axial Mach number and nondimensional force terms in the divergent portion of quasi-one dimensional magnetic nozzle flow for ion swirl frequency* $\omega_i^0 = 0$ *and electron swirl frequency* $\omega_e^0 = 500$. *Nondimensional ion cyclotron frequency* $\Omega_i = 1.3206$, *corresponding to Argon ions in* $450\ G$ *magnetic field and* $cs = 4108\ m/s$. *Nondimensional electron cyclotron frequency* $\Omega_e = 82160$.

As in fig. 3.3, also in this swirled electrons case we observe that the radial term of the Lorentz interaction is one order of magnitude higher than the axial one, suggesting that a strong radial confinement effect is in place, which cannot be modeled by a quasi-one dimensional analysis. By looking at the axial decay of the Lorentz term and comparing the fig. 3.3(b) and 3.4(b), we see that both the axial and the radial vanishes after about 3.5 throat radii, where the effect of the swirl becomes negligible.

With the results of this quasi-one dimensional analysis, we can draw some conclusion to guide the next steps in the assessment of the effect of differential swirling in the magnetic nozzle flow. Firstly, we proved quantitatively that the condition of eq. (3.11) makes of the electrons the species on which to focus our attention, since they are capable to provide much stronger acceleration and focusing to the nozzle jet. This is definitely due to their higher cyclotron frequency, which allows to raise the swirling to regimes where the absence of the azimuthal kinetic energy recovery is easily overcome. Finally, we note that a quasi-one dimensional model cannot fully describe the effect of the swirl on the magnetic nozzle flow because of the difference in order of magnitude between the axial and radial Lorentz terms. Moreover, we found that the strongest collimating action occurs at the nozzle throat, so that. Thus, more complex multi-dimensional models shall be adopted. However, in such models it will be no longer possible to neglect the radial equilibrium of the plasma flow and the influence of the swirling on such configuration, as will be described in detail in section 4.2.

Chapter 4

Nozzle Flow With Electron Azimuthal Current

4.1 Introduction

From the results of section 3.3, we see that the most significant effect of an externally induced azimuthal current is a radial compression or expansion of the plasma plume, depending on the sign of the current. As such, a quasi-one dimensional model cannot describe this phenomenon. Therefore, we need to expand our analysis to a two-dimensional axysimmetric geometry.

In their recent work, Schmit and Fisch [65] deal with the problem of solving the MN flow with azimuthal current by imposing a swirling velocity profile to each of the two species at the nozzle throat and then solving using the so modified Hooper's model [31]. Schmit and Fisch then show that such an azimuthal motion strongly affects the beam divergence of the magnetic nozzle, thus increasing the collimation of the jet. However, through numerical solution of a finite temperature plasma flow model, Ahedo and Merino [3] showed that the hypotheses of negligible pressure effect and absent ambipolar current used by Hooper's model prevents from really understand the thermal-electrostatic nature of the plasma expansion in magnetic nozzles. As consequence of this analysis, it became clear that the radial density distribution on the nozzle throat plane strongly affects the acceleration in the divergent of the nozzle and, eventually, the propulsive performances of the

nozzle itself.

Therefore, we wish to apply the concept of an externally induced azimuthal current to the more comprehensive model of Ahedo and Merino, to better understand the physics ruling the effect observed by Schmit and Fisch. Then, in the next Chapter, we will use the so derived solution of the flow to assess the effect of such an azimuthal current on the propulsive performances of the nozzle.

4.2 Approach

The presence of a net azimuthal current at the nozzle throat modifies the radial equilibrium of the plasma due to the interaction of the Lorentz force with the radial pressure term. Since the density distribution is neglected in Hooper's equations, such an approach cannot model this modified equilibrium state. Therefore, in this zero-temperature model, no particular care has to be taken while introducing a swirling in the plasma species. However, if we choose to apply an externally induced swirl in the full set of Navier-Stokes equations and we forget to modify the density distribution in order to restore the radial equilibrium, we would get to an over-determination of the system, thus to an unphysical solution, or no solution at all.

Therefore, as first step, we are asked to derive self-consistent conditions for the section where the current is applied, that is for the nozzle throat. To achieve such a goal, we solve the equations of an infinite plasma column in steady equilibrium, confined by a theta-pinch external magnetic field configuration, with an externally applied body force in the azimuthal equation. Mathematically speaking, we are adding a variable (the azimuthal force) we will eventually define through an additional equation. Once the new throat boundary conditions are defined, we solve the two dimensional axysimmetric flow in the nozzle.

From the results of Chapter 3, we choose to focus our attention on swirling the electron fluid only, which also shows an higher interaction with commonly used external body forces [19, 33, 34].

4.3 Nozzle Throat Boundary Conditions in Swirling Regime

4.3.1 Equilibrium Equations for an Infinite Column of Magnetized Plasma

Let's consider an infinite cylindrical plasma column, with an externally-applied axial magnetic field. In this section we will write the modified equilibrium equation for such a plasma configuration under the effect of an externally applied azimuthal body force F. We also make the assumption of low-β on a two species plasma (electrons and singly charged ions) where local quasi-neutrality $n_e = n_i = n$ holds everywhere. Following Ahedo [1], we assume equal radial velocities of electrons and ions $u_{ri} = u_{re} = u_r$. This is generally true in the plasma central region, where the charge separating electric field of the sheath is not yet significant. Finally, since the propulsive parameters defined in section 5.2 are mostly influenced by the densest region of the plume, we will limit our investigation to that region.

The modified momentum equation in cylindrical coordinates (r, ϑ, z), assuming axysimmetry $(\partial/\partial\vartheta = 0)$ and dropping the axial derivatives $(\partial/\partial z = 0)$ in the azimuthal direction for the electrons is [1] :

$$\begin{aligned} m_e u_r \frac{du_{\theta\mathrm{e}}}{dr} + m_e \frac{u_{\theta\mathrm{e}} u_r}{r} = \; & eBu_r - m_e(\nu_{\mathrm{en}} + \nu_w)u_{\theta\mathrm{e}} \\ & -m_e \nu_{\mathrm{ei}}(u_{\theta\mathrm{e}} - u_{\theta\mathrm{i}}) + F \quad , \end{aligned} \tag{4.1}$$

where ν_{en}, ν_{ei} are the electron-neutral and electron-ion collision frequencies, respectively, and ν_w is the ion production frequency due to axial diffusion and ionization of neutrals. We introduce F in eq. (4.1) as a generalized body force that, acting on electrons only, induces the differential motion in the two species required to create a net azimuthal current. The other three momentum equations and the continuity equation are left unchanged:

$$\begin{aligned} m_e u_r \frac{du_r}{dr} - m_e \frac{u_{\theta\mathrm{e}}^2}{r} = \; & -\frac{1}{n}\frac{d}{dr}(T_e n) + e\frac{d\phi}{dr} - eBu_{\theta\mathrm{e}} \\ & -m_e(\nu_{\mathrm{en}} + \nu_w)u_r \quad , \end{aligned} \tag{4.2}$$

$$\begin{aligned} m_i u_r \frac{du_r}{dr} - m_i \frac{u_{\theta\mathrm{i}}^2}{r} = & -\frac{1}{n}\frac{d}{dr}(T_i n) + e\frac{d\phi}{dr} + eBu_{\theta\mathrm{i}} \\ & -m_i(\nu_{\mathrm{in}} + \nu_w)u_r \quad , \end{aligned} \tag{4.3}$$

$$\begin{aligned} m_i u_r \frac{du_{\theta\mathrm{i}}}{dr} + m_i \frac{u_{\theta\mathrm{i}} u_r}{r} = & -eBu_r - m_i(\nu_{\mathrm{in}} + \nu_w)u_{\theta\mathrm{i}} \\ & +m_i\nu_{\mathrm{ei}}(u_{\theta\mathrm{e}} - u_{\theta\mathrm{i}}) \quad , \end{aligned} \tag{4.4}$$

$$\frac{1}{r}\frac{d}{dr}(rnu_r) = n\nu_w \quad . \tag{4.5}$$

We follow Ahedo by dropping the electric potential gradient in the plasma bulk region ($\nabla\phi = 0$) and the ion azimuthal velocity, and nondimensionalizing the equations using the sheath coordinate R_s, the sonic speed $c_s = \sqrt{T_e/m_i}$, the density on the axis n_0, the electron energy T_e, which is considered constant. The frequencies are nondimensionalized by c_s/R_s. We define also the nondimensional azimuthal velocity of electrons as

$$\hat{u}_{\theta\mathrm{e}} = \frac{u_{\theta\mathrm{e}}}{c_s}\sqrt{\frac{m_e}{m_i}} \tag{4.6}$$

and the nondimensional lower-hybrid frequency as

$$\hat{\omega}_{\mathrm{lh}} = \frac{eB}{\sqrt{m_i m_e}}\frac{R_s}{c_s} \quad . \tag{4.7}$$

Manipulating eq. (4.1) dropping the inertia terms and under the hypotheses of cold ions ($T_i \approx 0$) and negligible ionic azimuthal motion ($u_{\theta\mathrm{i}} \approx 0$),[1] we get the modified expression for the radial velocity

$$\hat{u}_r = \frac{\hat{\nu}_e}{\hat{\omega}_{\mathrm{lh}}} - \frac{\hat{F}}{\hat{\omega}_{\mathrm{lh}}} \quad , \tag{4.8}$$

where $\hat{\nu}_e = \hat{\nu}_{\mathrm{ei}} + \hat{\nu}_{\mathrm{en}} + \hat{\nu}_w$. From eq. (4.8) we can immediately see how the azimuthal body force $\hat{F}$ couples with the magnetic field, parametrized by $\hat{\omega}_{\mathrm{lh}}$, to modify the radial velocity profile. Indeed, it is clear that a positive force $\hat{F}$ would reduce the outward-directed radial velocity by inducing a diamagnetic current that, coupling with the axial magnetic field, gives an inward-directed Lorentz force that radially confines the plasma.

From the radial momentum balance on the electrons we get

$$\hat{\omega}_{\mathrm{lh}}\hat{u}_{\theta\mathrm{e}} = -\frac{d\ln\hat{n}}{d\hat{r}} \quad , \tag{4.9}$$

which, together with the continuity equation, leads to the modified diffusion equation:

$$\frac{d^2\hat{n}}{d\hat{r}^2} + \left(\frac{1}{\hat{r}} + \frac{\hat{\omega}_{\mathrm{lh}}}{\hat{\nu}_e}\hat{F}\right)\frac{d\hat{n}}{d\hat{r}} + \left(a_0^2 + \frac{\hat{\omega}_{\mathrm{lh}}}{\hat{\nu}_e}\frac{d\hat{F}}{d\hat{r}} + \frac{\hat{\omega}_{\mathrm{lh}}}{\hat{\nu}_e}\frac{\hat{F}}{\hat{r}}\right)\hat{n} = 0 \quad , \tag{4.10}$$

where

$$a_0 = \hat{\omega}_{\mathrm{lh}}\sqrt{\frac{\hat{\nu}_w}{\hat{\nu}_e}} \quad . \tag{4.11}$$

This equation is a second-order ODE, with boundary conditions on the axis $\hat{n}(0) = 1$ and $\hat{n}'(0) = 0$, whose solution clearly depends on the particular choice of $\hat{F}$. The integration is stopped when the sheath is reached, thus for $\hat{u}_r = 1$ in accordance with the Bohm criterion [16].

From eq. (4.10) we see that the net effect of the body force is scaled by the ratio $\hat{\omega}_{\mathrm{lh}}/\hat{\nu}_e$, which is the ratio of the non-dimensional magnetic field parameter and the electron global collisional term. In other words, the effect of the body force is proportional to the magnetization, which rules the strength of the Lorentz interaction, and is inversely proportional to the electron collisional term, which acts as momentum sink for the electronic population.

The solution of eq. (4.10) in the unforced case, that is when $\hat{F} = 0$, is a 0-th order Bessel function

$$\hat{n}(\hat{r}) = J_0(a_0\hat{r}) \quad , \tag{4.12}$$

with the first zero at the sheath coordinate $\hat{n}(\hat{r} = 1) = 0$ [1]. The resulting plasma density profile peaks on the axis and is a direct consequence of the θ-pinch confinement configuration we imposed in the plasma column [30]. We will use the case of $\hat{F} = 0$ as reference for the evaluation of the solution in the $\hat{F} \neq 0$ case.

4.3.2 Specialization for Particular Force Formulation

The solution of eq. (4.10) depends on the definition of the body force. Thus, for proceeding with the analysis, we have to assume a form of $\hat{F}$. The quantitative results will depend strictly on this choice, but some consideration on the behavior of the plasma can be generalized to a broader class of interactions. We choose to introduce a $\hat{F}$ defined as follows

$$\hat{F} = \hat{\Omega}\hat{r} - \hat{u}_{\theta\mathrm{e}} \quad . \tag{4.13}$$

An $\hat{F}$ so defined is a generalized force that drags the azimuthal motion of the electrons towards a rigid body motion of angular frequency $\hat{\Omega}$. Clearly, this generalized force vanishes when the electrons are moving collectively at the desired angular frequency and changes sign for higher $\hat{u}_{\theta \mathrm{e}}$. Secondly, we observe that a positive $\hat{\Omega}$ would induce a diamagnetic electron current, while a negative $\hat{\Omega}$ would induce a paramagnetic one.

Such a definition of $\hat{F}$ resembles the effect of Rotating Magnetic Field (RMF) devices used in current-drive Reversed Field Configuration (RFC) fusion experiments.[69] Indeed, it has been observed that a RMF tends to interact well with the electrons, but are generally ill-coupled with the ions [69]. It is known that the magnitude of the interaction of RMF with the electron azimuthal motion depends linearly on the slip factor $S = (1-\hat{u}_{\theta e}/\Omega\hat{r})$ between the RMF and the azimuthal motion of the electrons [33]. Therefore, such a definition of $\hat{F}$ correspond to a generalization of the RMF-electrons force within the approximation of fixed ions [33] and of $\hat{\Omega}_{\mathrm{ce}}^2 \gg \nu_{\mathrm{ei}}^2$. For the purposes of this thesis, we can assume the axial residency time of the flow to be much lower than the ion-electron relaxation time, thus we will neglect the reduction of net current due to azimuthal ion acceleration. This consideration further justifies our assumption of azimuthally-fixed ions.

Therefore, we can substitute eq. (4.13) into eq. (4.8)

$$\hat{u}_r = \frac{\hat{\nu}_e + 1}{\hat{\omega}_{\mathrm{lh}}} - \frac{\hat{\Omega}\hat{r}}{\hat{\omega}_{\mathrm{lh}}} \quad , \tag{4.14}$$

and eq. (4.10)

$$\frac{d^2\hat{n}}{d\hat{r}^2} + \left(\frac{1}{\hat{r}} + \left(\frac{\hat{\omega}_{\mathrm{lh}}\hat{\Omega}}{\hat{\nu}_e + 1} \right) \hat{r} \right) \frac{d\hat{n}}{d\hat{r}} + \left(a_{\hat{\Omega}}^2 + 2 \left(\frac{\hat{\omega}_{\mathrm{lh}}\hat{\Omega}}{\hat{\nu}_e + 1} \right) \right) \hat{n} = 0 \quad , \tag{4.15}$$

where

$$a_{\hat{\Omega}} = \hat{\omega}_{\mathrm{lh}} \sqrt{\frac{\hat{\nu}_w}{\hat{\nu}_e + 1}} \quad . \tag{4.16}$$

As said, other definitions of $\hat{F}$ are valid as well and their effect can be analyzed in the same way of the specific $\hat{F}$ here presented. However, we point that other forms of $\hat{F}$ should respect the sheath boundary conditions, which means that $\hat{u}_r$ shall raise to the unity at the sheath coordinate, in order to respect the Bohm criterion. A viable way for assuring such occurrence may

be to introduce a piecewise definition of $\hat{F}$, where the mathematical form of the body force transitions with continuity from the bulk to an external region capable of modeling the physics ruling the sheath boundary.

4.3.3 Solution for Plasma Bulk Region

Equation (4.15) has an analytical solution for the given boundary conditions

$$\hat{n}(\hat{r}) = \frac{N(Z)H(-Y\hat{r}^2, Z) - (Z+1)M(Y\hat{r}^2, Z)}{N(Z)H(0, Z) - (Z+1)M(0, Z)} \quad , \tag{4.17}$$

where M and N are Meijer G-Functions and H is a Kummer's confluent hypergeometric function

$$M(w, Z) = G^{2,0}_{1,2}\left(w \middle| \begin{matrix} -Z \\ 0, 0 \end{matrix}\right) \quad , \tag{4.18}$$

$$N(Z) = G^{2,0}_{1,2}\left(0 \middle| \begin{matrix} -1-Z \\ -1, 0 \end{matrix}\right) \quad , \tag{4.19}$$

$$H(w, Z) = {}_1F_1\left(1+Z; 1; w\right) \quad . \tag{4.20}$$

The functions Y and Z depends on the plasma parameters and $\hat{\Omega}$:

$$Y = \frac{\hat{\omega}_{\mathrm{lh}}\hat{\Omega}}{2(1+\hat{\nu}_e)} \quad , \tag{4.21}$$

$$Z = \frac{a^2_{\hat{\Omega}}(1+\hat{\nu}_e)}{2\hat{\omega}_{\mathrm{lh}}\hat{\Omega}} = \frac{\hat{\nu}_w\hat{\omega}_{\mathrm{lh}}}{2\hat{\Omega}} \quad . \tag{4.22}$$

In accordance with the results of thin-inertia layer of Ahedo [1], we impose $a_{\hat{\Omega}}$ to be the first zero of the *0-th* Bessel function J, thus $a_{\hat{\Omega}} \approx 2.405$ and $\hat{\nu}_w = 2.405^2(\hat{\nu}_e + 1)/\hat{\omega}_{\mathrm{lh}}$, and the solution simplifies to

$$\hat{n}(\hat{r}) = J_0(a_{\hat{\Omega}}\hat{r}) \quad . \tag{4.23}$$

Reporting in fig. 4.1 the solutions for $\log_{10}(\hat{n})$, $\hat{u}_{\theta\mathrm{e}}$ and $\hat{u}_{\mathrm{re}}$, parameterized by different values of $\hat{\Omega}$, we can now draw some considerations on the modified equilibrium state.

First, it is clear from fig. 4.1(a) that the radial density profile of the plasma column changes significantly even for low values of $\hat{\Omega}$. The resulting

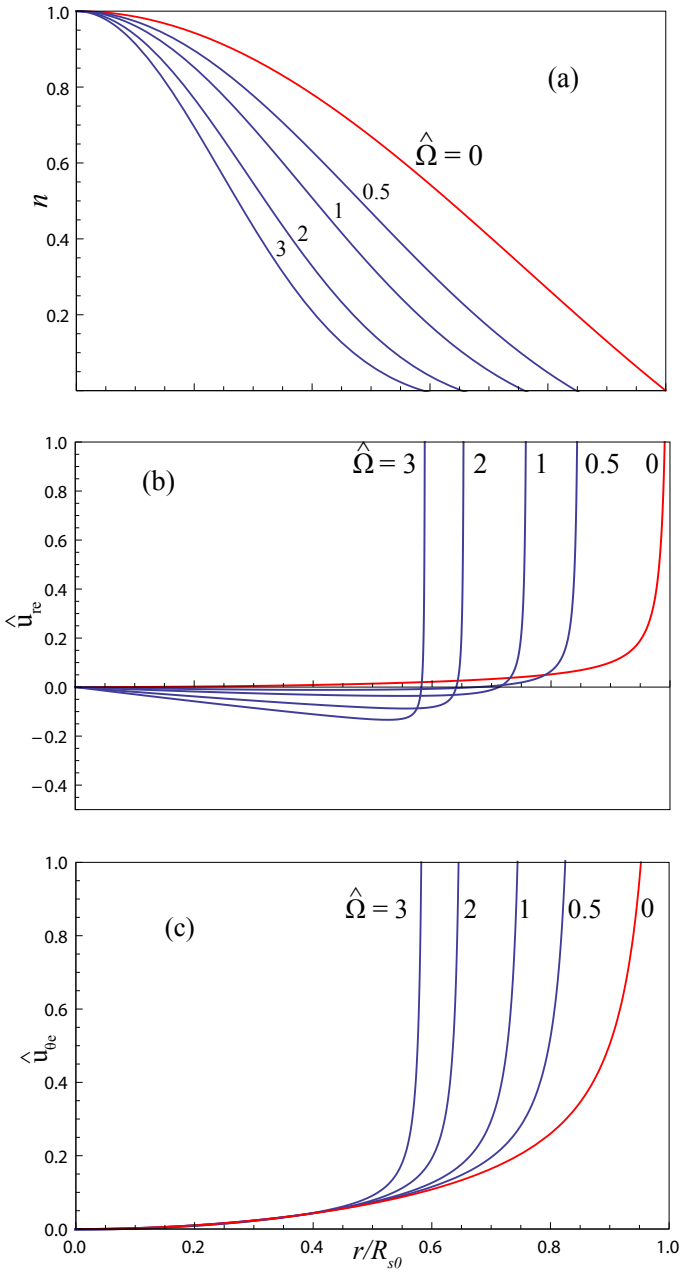

Figure 4.1: *Radial profile of different plasma quantities at different values of $\hat{\Omega}$. The radial coordinate is normalized on R_{s0}, which is the sheath position in case of $\hat{\Omega} = 0$. All other radial profiles are normalized on the respective $R_s(\hat{\Omega})$. Reference parameters $\hat{\omega}_{lh} = 10$, $\hat{\nu}_e = \hat{\nu}_i = 1$. The profiles marked in red are the reference solution for $\hat{\Omega} = 0$.*

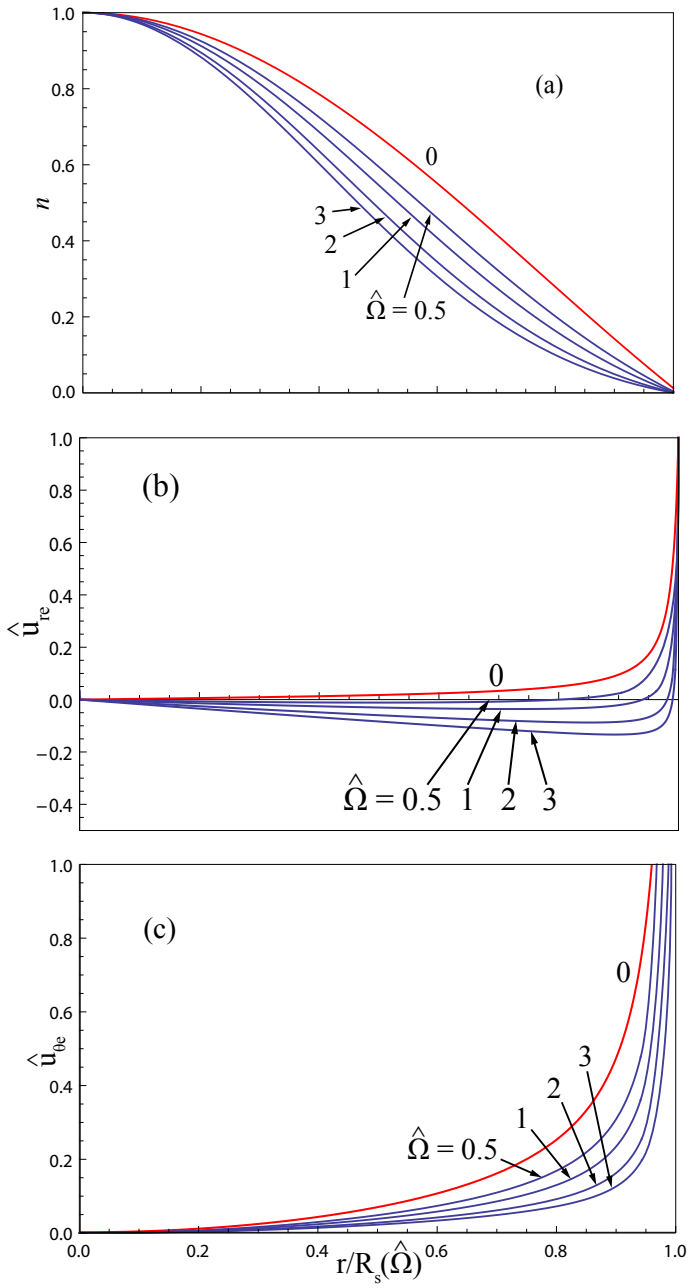

Figure 4.2: *Radial profile of different plasma quantities at different values of $\hat{\Omega}$. The radial coordinate normalized on the respective $R_s(\hat{\Omega})$, which decreases as $\hat{\Omega}$ raises, as reported in fig. 4.3. Reference parameters $\hat{\omega}_{lh} = 10$, $\hat{\nu}_e = \hat{\nu}_i = 1$. The profiles marked in red are the reference solution for $\hat{\Omega} = 0$.*

shape of the density distribution shows an inflection point which leads to a steeper radial decay. Thus, the density profile is more peaked at the center of the cylinder, and rarefied in the external bulk region.

Even more importantly, fig. 4.1(a) and (b) show that the position of the sheath coordinate R_s depends on $\hat{\Omega}$ and decreases monotonically with the raise of the force parameter. This implies that the bulk of the plasma is contained in a smaller cylinder, and the resulting axial flow is more pinched along the axis. By plotting this dependency in fig. 4.3, we see a strong decrease of R_s for $\hat{\Omega} < 2$, with the decrease rate reducing after the knee. This knee is more marked for higher value of magnetization $\hat{\omega}_{\rm lh}$. No horizontal asymptote has been identified, and R_s decreases monotonically to 0 for $\hat{\Omega} \to \infty$. However, increasing the electron azimuthal current would eventually lead to the rise of the dropped electron inertia terms and of the diamagnetically-induced magnetic field, causing the loss of validity to this model.

It has been observed[12, 15] that helicon waves concentrate in the center of the column. Therefore, a more peaked radial density profile increases the power absorption, eventually leading to higher ionization and heating efficiencies of helicon-based plasma source. Furthermore, by lowering the density close to the plasma boundary we expect also fewer wall losses and weaker radial energy transport.

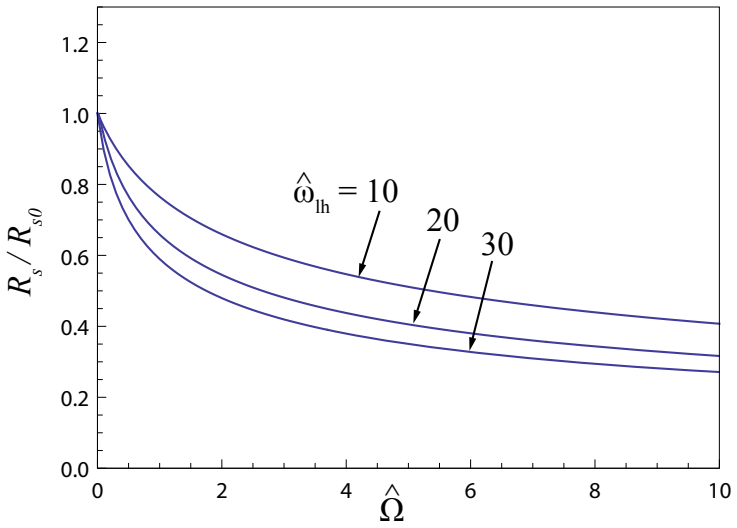

Figure 4.3: *Sheath coordinate variation with $\hat{\Omega}$ at different values of $\hat{\omega}_{lh}$. Reference parameters $\hat{\nu}_e = \hat{\nu}_i = 1$.*

In fig. 4.1(c), we see that the azimuthal velocity profile $\hat{u}_{\theta \mathrm{e}}$ shows a strong difference between a central region of roughly linear radial dependency, and a sharp increase nearby the sheath. This eventually mean that the body force has little effect on the central region of the plasma column, but strong influence in a thin external region. Moreover, the size of this high-current layer decreases with the increase in magnitude of the body force.

The radial velocity profile depicted in fig. 4.1(c) shows a marked difference with respect to the reference $\hat{\Omega} = 0$ condition. We see that, for any $\hat{\Omega} > 0$, we can identify two regions within the plasma bulk. Internally, the radial Lorentz force due to the swirl-magnetic field coupling dominates over the sheath pull, and the radial velocity is negative. Consequently, the particles that arise due to axial diffusion and ionization are pushed toward the axis of the column. We also see that the magnitude of this negative $\hat{u}_{\mathrm{r\,e}}$ increases with the radius, following the approximately linear increase of the radial Lorentz force, as clear from eq. (4.8). Eventually, when the density decreases in the vicinity of the sheath, the magnitude of the confining effect diminishes and the density gradient pushes away the few particles present in that region, allowing them to reach the sonic condition and enter the plasma sheath.

The electric potential $\hat{\phi}$ is roughly constant for the bulk plasma region, showing a sudden and steep decrease nearby the sheath, in accordance with the sheath theory and what noted by Ahedo [1].

4.3.4 Body Force Power Validity Domain

By introducing the body force $\hat{F}$, we are providing additional power to the plasma column, which can be computed by integrating the dot product $\hat{\mathbf{F}} \cdot \hat{\mathbf{u}}_e$ over the cross section. Being $\hat{F}$ purely azimuthal, the integral simplifies to

$$\hat{\mathcal{P}}_{\hat{F}} = \int_A \hat{F}\ \hat{n}\ \hat{u}_{\theta \mathrm{e}} \sqrt{\frac{m_i}{m_e}} dA \quad , \tag{4.24}$$

where the scaling term $\sqrt{m_i/m_e}$ is introduced for accounting for the definition of $\hat{u}_{\theta \mathrm{e}}$ given in eq. (4.6).

By computing this integral we find that the result can be negative for low enough value of $\hat{\Omega}$. A negative value of $\mathcal{P}_{\hat{F}}$ means that the body force is slowing down the azimuthal motion of electrons. This unphysical result is

related to the definition of $\hat{F}$ of eq. (4.13), where is clear that the sign of the body force depends on the relative magnitudes of $\hat{\Omega}r$ and $\hat{u}_{\theta e}$ Thus, we limit the validity of the analysis on the jet and body force powers for $\hat{\Omega} \geq 0.5$. All the other quantities show well-behaved trends even for lower values of $\hat{\Omega}$, thus we retain the full solutions in these cases for completeness.

4.4 Nozzle Flow Approximated Analytical 2D Model

Armed with the modified solution of the magnetized plasma column, we may now proceed to compute the new nozzle flow solution. Specifically, we will use the new radial density profile as boundary condition at the throat of an electron-driven magnetic nozzle to solve the two-dimensional expansion of a plasma. This coupling models the implementation of a *"focusing stage"* between the injection plane and the nozzle throat in a thermal plasma thruster.

4.4.1 Model Assumptions and Governing Equations

For this analysis, we use and expand the approximated analytical model of Little and Choueiri [49]. This method allows to solve the plasma flow of a magnetic nozzle without the need of implementing CFD codes [23] or other methods such as numerical solver of the method of the characteristics [3, 5, 6]. Moreover, the analytical expressions give insight to the physical nature of the plume expansion in electron-driven magnetic nozzles. Following such a method, we make use of a coordinate transformation from physical (r, z) to magnetic (ψ, ζ), where ψ is the magnetic stream function and ζ is the magnetic scalar potential [27], defined according to

$$\mathbf{B} = \frac{1}{r}(\hat{\vartheta} \times \nabla\psi) = -\nabla\zeta \quad . \tag{4.25}$$

This transformation allows to straighten the magnetic field lines in the newly defined (ψ, ζ) space, as shown in fig. 4.4. Moreover, this choice leads to write the balance equations along and across the magnetic surfaces, which are more representative of the magnetic nozzle physics than the geometric (r, z) and are not subject to singularities after the magnetic field turning point.

We will consider the magnetic field as generated by a single current loop at coordinates $r = a_e, z = 0$. This choice of magnetic topology leads to the following approximate form for the non-dimensionalized magnetic coordinates $\psi(r, z)$ and $\zeta(r, z)$:

$$\psi(r,z) = \frac{r^2/2}{\left((r^2+1)+z^2\right)^{3/2}} \quad , \tag{4.26}$$

$$\zeta(r,z) = \frac{3+z+r^2 z+z^3}{2\left(1+r^2+z^2\right)^{5/2}} \quad , \tag{4.27}$$

where the coordinates (r, z) have been nondimensionalized by a_e.

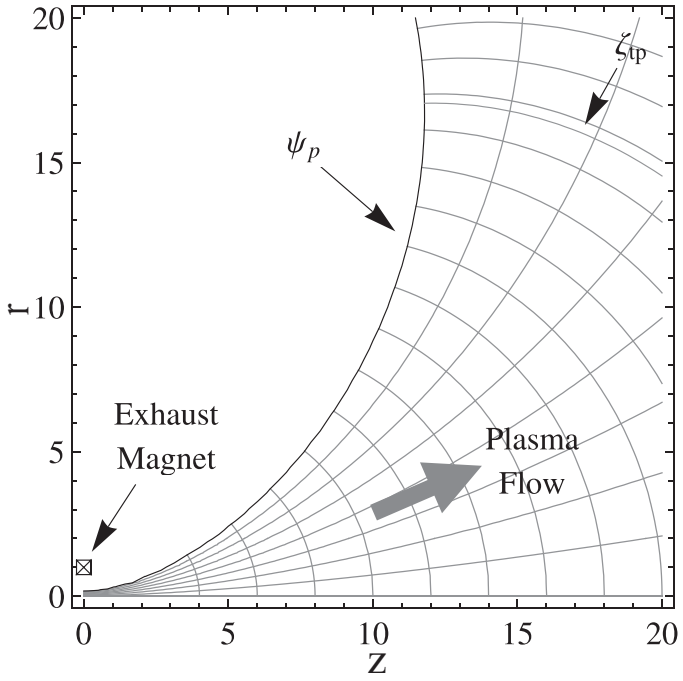

Figure 4.4: *Magnetic nozzle field topology [49]. The grid shows the transformation from geometric (r, z) to magnetic (ψ, ζ) coordinates system. The plasma-vacuum interface is marked by the stream coordinate ψ_p. The plasma-vacuum magnetic surface turning point has coordinate ζ_{tp}.*

The governing equation of the finite-temperature, two-population, uncollisional ($\mathbf{R_a} = 0$), inviscid ($\mathbf{\Pi_a} = 0$) [49] flow under the additional assump-

tions of section 2.3.2 and negligible electron inertia are:

$$\begin{cases} \nabla \cdot n\mathbf{u}_i = 0 \\ m_i \tilde{\mathbf{u}_\mathbf{i}} \cdot \nabla \tilde{\mathbf{u}_\mathbf{i}} = -e\nabla\phi + eu_{\theta\mathrm{i}} B\hat{\mathbf{n}} + m_i \dfrac{u_{\theta\mathrm{i}}^2}{r}\ \hat{\mathbf{r}} \\ 0 = -T_e \nabla \ln(n) + e\nabla\phi - eu_{\theta\mathrm{e}} B\hat{\mathbf{n}} \\ rm_i u_{\theta\mathrm{i}} + e\psi = R_i^0 m_i u_{\theta\mathrm{i}}^0 + e\psi^0 \\ ru_{\theta\mathrm{e}} = D(\psi) \\ T_e = T_e^0 \\ T_i = 0 \end{cases} . \tag{4.28}$$

To solve the nozzle flow, Little and Choueiri integrate the plasma governing equations along the magnetic streamlines ψ with the nozzle throat plane as boundary condition. We will follow here the same scheme, modifying the equations for the case of non-zero azimuthal velocity of the electrons.

The adopted nondimensionalization uses the coil radius a_e as reference length, the electron temperature T_e for the energies and the sonic speed $c_s = \sqrt{T_e/m_i}$ .The nondimensional nozzle throat radius is r_e. We retain the null azimuthal velocity of ions, but we introduce a non-zero azimuthal velocity for the electrons, $M_{\theta\mathrm{e}}$.

The system of differential equations we want to solve has five unknowns: the streamwise (ionic) Mach number M_i, the electric potential ϕ, the number density n, the azimuthal electronic Mach number $M_{\theta\mathrm{e}}$ and the flow-magnetic field separation angle α_i. Thus, five relations are required to evaluate all the unknowns.

The first equation is get by multiplying the momentum equation for the ions fluid by the stream versor $\hat{\mathbf{s}} \parallel \mathbf{u}_i$

$$\hat{\mathbf{s}} \cdot \nabla \left(\frac{1}{2} M_i^2 + \phi \right) = \hat{\mathbf{s}} \cdot \left(\mathbf{M}_i \times \left(\frac{\mathbf{B}}{\rho_i} + \nabla \times \mathbf{M}_i \right) \right) \quad , \tag{4.29}$$

which gives the conservation of energy along the flow streamline

$$\hat{\mathbf{s}} \cdot \nabla \left(\frac{1}{2} M_i^2 + \phi \right) = 0 \quad . \tag{4.30}$$

From the electron momentum equation multiplied by the magnetic versor $\hat{\mathbf{b}}$ we get the second relation

$$\hat{\mathbf{b}} \cdot \nabla \left(\phi - \ln(n) \right) = \hat{\mathbf{b}} \cdot \left(\mathbf{M}_e \times \left(\frac{\mathbf{B}}{\rho_e} \right) \right) \quad , \tag{4.31}$$

which leads to

$$\hat{\mathbf{b}} \cdot \nabla \left(\phi - \ln(n) \right) = 0 \quad . \tag{4.32}$$

Equation (4.32) indicates that the electrons still follow the Boltzmann relation, without any trace of the action of $M_{\theta \mathrm{e}}$

$$n(\psi, \zeta) = n_t(\psi) e^{\left(\phi(\psi,\zeta) - \phi^0(\psi) \right)} \quad . \tag{4.33}$$

This result should not surprise, since the effect of the Lorentz force is always perpendicular to the magnetic streamline, thus the balance along it must not change. On the contrary, in the case of ionic azimuthal current, the ion mass leads to finite azimuthal kinetic energy, which is streamwisely recovered as the swirling motion decay for conservation of angular momentum along the expanding streamline.

The third equation comes from the continuity law, in integral form

$$\int_S n \tilde{M} \, \tilde{\hat{\mathbf{s}}} \cdot \mathbf{dA} = 0 \quad , \tag{4.34}$$

where the integration surface S is generally composed by the nozzle throat plane and a ζ-surface along the nozzle.

As previously stated, we added a new variable ($M_{\theta \mathrm{e}}$) with respect to Little and Choueiri's model, hence an additional equations is needed to close the system. We take this equation from the conservation of angular momentum along the streamlines, under the hypothesis of magnetized electrons.

$$\hat{\mathbf{b}} \cdot \nabla \left(M_{\theta \mathrm{e}} r \right) = 0 \quad . \tag{4.35}$$

Finally we introduce the quasi-field aligned assumption as fifth and last relation.

$$\hat{\mathbf{b}} \approx \hat{\mathbf{s}} \quad . \tag{4.36}$$

This assumption correspond to imposing the fifth unknown α_i to be equal to zero, which is in contrast with results from numerical solutions of the

flow [3] and to the same idea of flow separation. Now, the solution of the *streamwise* differential equations along the flow streamline can be projected on the magnetic streamline by means of the cosine of the angle, $\cos(\alpha_{\mathrm{i}})$. Therefore, since $\cos(\alpha_{\mathrm{ei}}) \sim 1$ even for rather large values of α_{i}, Little and Choueiri concluded that a quasi-field aligned assumptions well approximate the solution of the flow foll all the unknowns, except of course α_{i}.

Ultimately, the magnetic coordinate transformation and the quasi-field aligned assumptions allow to transform a two-dimensional integration of an hyperbolic system of PDEs in the physical space (r, z) into a bundle of streamwise solutions of ODEs, functions of ζ only, and parametrized by ψ.

As noted by Little and Choueiri, the quasi-field aligned hypothesis leads to an overestimation of the electric potential across the magnetic streamlines, since the ions are forced to be tight to the electrons. From a propulsive point of view, neglecting the ion separation from the magnetic surfaces leads to an overestimation of the nozzle divergence, hence to an underestimation of the efficiency and thrust coefficient.

Recalling for the moment the so-far neglected ionic azimuthal velocity $M_{\theta\mathrm{i}}$, we evaluate the electric potential through the momentum equation for the ions perpendicular to $\hat{\mathbf{b}}$

$$\frac{\partial \phi}{\partial \psi} = -K M_i^2 + \frac{M_{\theta\mathrm{i}}}{r} \quad . \tag{4.37}$$

In this equation the Lorentz force makes its first appearance, but in the ionic term only. Indeed, we see the electrons does not affect explicitly the potential distribution. We could explicit the effect of electron swirl on density by composing eq. (4.37) with the electron cross-field momentum equation:

$$\frac{\partial \phi}{\partial \psi} = \frac{\partial \ln n}{\partial \psi} + \frac{M_{\theta\mathrm{i}}}{r} \quad , \tag{4.38}$$

leading to a cross field equation for the density:

$$\frac{\partial \ln n}{\partial \psi} = -K M^2 + \frac{M_{\theta\mathrm{i}} - M_{\theta\mathrm{e}}}{r} \quad . \tag{4.39}$$

which, if solved, gives the cross-field density distribution at each ζ. However, we note that it is not necessary to solve this equation, since the density can

be computed using the Boltzmann relation and the electric potential coming from eq. (4.37). Nevertheless, eq. (4.39) does affect the boundary conditions at the nozzle throat, which have to be consistent with the presence of the azimuthal current $M_{\theta e}$.

Therefore, we conclude that the presence of differential species swirling influences the two-dimensional density distribution inside the magnetic nozzle in two ways: the ion azimuthal current and kinetic energy recovery induce a change in the potential profile ϕ across the magnetic streamlines, while the electron current changes the boundary conditions at the nozzle throat, n_t. Here arises a strong difference with what previously observed by Schmit and Fisch [65]. According to our equations, the effect of introducing an electron swirling motion is recorded at the nozzle throat and is limited to a change in the radial density profile, as described in section 4.3. What happens in the divergent part of the nozzle is the propagation of the newly derived equilibrium state throughout the downstream plume, according to the hyperbolic nature of the supersonic fluid equations. This allows the modified radial density distribution to propagate along the nozzle, even outside the region of influence of F. This observation implies that the actual effect of an azimuthal current cannot be correctly modeled by using a zero-temperature model. Indeed, in such a case, the radial Lorentz force induced by the swirling would not be balanced by any pressure, leading to a non-equilibrium situation in contrast with the steady state regime of operation of MNs.

4.4.2 Analytical Solution

In section 4.4.1 we described the governing equation of the approximate analytical model of Little and Choueiri [49]. According to this formulation, all the quantities are written as function of the plasma potential ϕ, which is in turn solved using eq. (4.37). In the case of no ion swirling motion, we see we get the same expression of Little and Choueiri [49]. Thus, the potential has the analytical solution

$$\phi(\psi, \zeta) = \frac{1}{2} + C(\zeta) \exp\left(\int_0^{\psi} K(\psi', \zeta) d\psi' \right) \quad . \tag{4.40}$$

If we approximate the streamline curvature $K(\psi, \zeta)$ with its Taylor series for $\psi \to 0$

$$K(\psi, \zeta) \approx k(\zeta) \approx \frac{3}{4\sqrt{2\zeta}} \quad , \tag{4.41}$$

we finally get an handy expression for the electric potential ϕ

$$\phi(\psi, \zeta) = \frac{1}{2}\left(1 - (1 - 2\overline{\phi})\frac{2k\psi}{e^{2k\psi} - 1}e^{2k\psi}\right) \quad , \tag{4.42}$$

where $\overline{\phi}$ is the quasi-one dimensional approximation of the potential. We can get an implicit equation for $\overline{\phi}$ by expressing the Mach number and the density according to eq. (4.30) and (4.33) in the quasi-one dimensional continuity equation $\overline{n}A\overline{M}_i = \overline{n}_t A_t \overline{M}_t$

$$e^{\overline{\phi}}\sqrt{1 - 2\overline{\phi}} = \frac{A_t}{A} \quad . \tag{4.43}$$

Once the potential is solved, all other quantities are directly computed by using the stream-wise equations and the nozzle throat plane conditions.

4.4.3 Throat Boundary Conditions

The boundary condition for ϕ at the nozzle throat does not change from Little and Choueiri, since also the new radial density profile shows negligible potential drop in the bulk region.

$$\begin{cases} \phi(\psi, \zeta_t) = 0 \\ \\ M_t = 1 \\ \\ M_{\theta \mathrm{i}}(\psi, \zeta_t) = 0 \end{cases} . \tag{4.44}$$

An additional boundary condition for the new variable $M_{\theta \mathrm{e}}(\psi, \zeta)$ has to be added to the set. The final boundary condition comes from the radial density profile in magnetic coordinates.

$$\begin{cases} M_{\theta \mathrm{e}}(\psi, \zeta_t) = M^0_{\theta \mathrm{e}}(\psi) \\ \\ n(\psi, \zeta_t) = n_t(\psi) \end{cases} . \tag{4.45}$$

The boundary condition on the density eq. (4.45)(b) has to be consistent with the azimuthal current at the nozzle throat eq. (4.45)(a). Since we want to analyze the effect of the body force F on the nozzle flow, we apply the infinite plasma column solution with F presented in section 4.3 as boundary condition at the throat for both density and azimuthal velocity. According to this match, we see that the plume enters the throat with a narrower density radial profile. Since the quasi-one dimensional continuity equation still holds, the density profile at the throat is scaled by the ratio:

$$\rho(\hat{\Omega}) = \int_0^{R_s(\hat{\Omega})} \hat{r}\ \hat{n}(\hat{r})d\hat{r} \Big/ \int_0^{R_{s0}} \hat{r}\ \hat{n}(\hat{r})d\hat{r} \quad , \tag{4.46}$$

whose effect is reported in fig. 4.5.

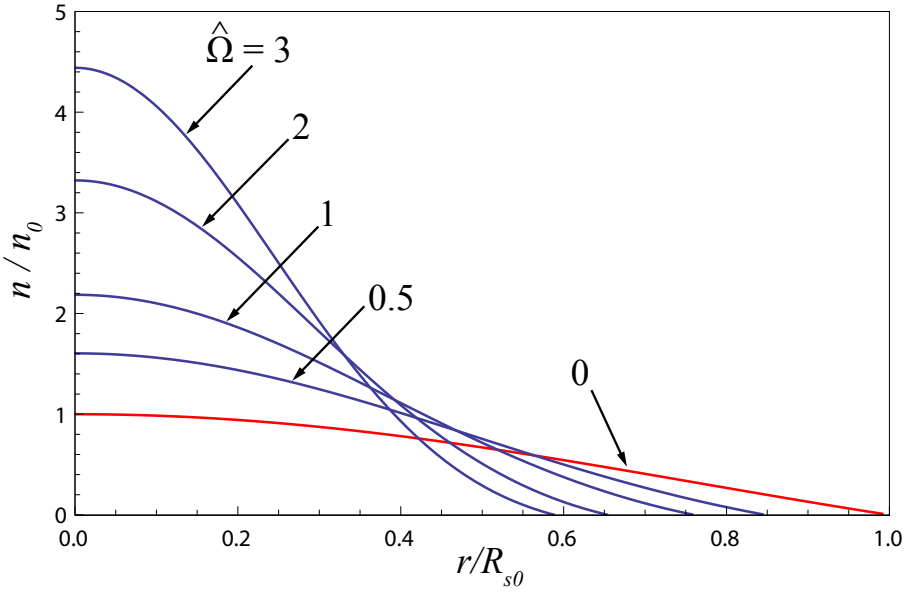

Figure 4.5: *Change in the non-dimensional plasma radial density profile at the throat with* $\hat{\Omega}$. *The red line is the baseline for* $\hat{\Omega} = 0$. *Magnetization parameter* $\hat{\omega}_{lh} = 10$.

By stopping the integration at $R_s(\hat{\Omega})$ while performing this scaling, we are actually neglecting the plasma density inside the sheaths, which are located between $R_s(\hat{\Omega})$ and the physical radius of the confining chamber r_e. However, we see from fig. 4.1(a) and fig. 4.5 that the plasma density in this region is orders of magnitude lower than that in the plasma bulk, thus has a negligible mass flow rate.

From fig. 4.5 we see the combinations of the two effects of the application of F. First, the plasma column is compressed to a narrower region, thus the value of the *effective* plasma column radius at the throat $r_e^F = R_s(\hat{\Omega})$ decreases, as described in section 4.3.3. Thus, for mass flux conservation, the relative density peak value in the throat center increases. From fig. 4.5 we see that this increase is monothonic but not proportional to the r_e^F decrease. This is due to the fact that the mass flux depends quadratically on the radius, but only linearly on the density. Therefore, we expect that the nozzle performances related to the density peak value to be more affected than those dependent on the sheath radius value.

4.4.4 Magnetic Nozzle Flow in Electron Swirling Regime

Having modified the equations and closed the system of boundary conditions, we can now solve the plasma flow in the magnetic nozzle, comparing the new results with the baseline no-swirling solution of Little and Choueiri [49].

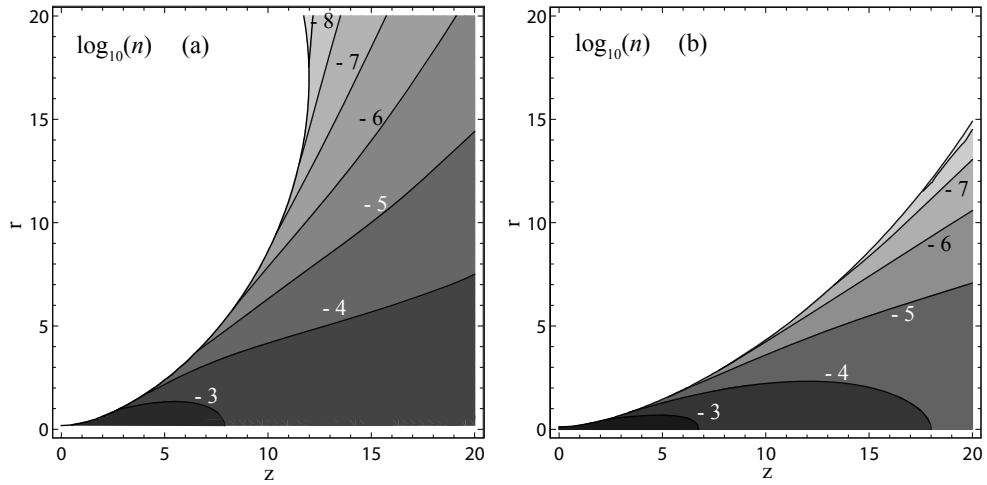

Figure 4.6: *Change in plasma flow density for $\hat{\Omega} = 2$. Throat radius $r_e = 0.185$. Magnetization parameter $\hat{\omega}_{lh} = 10$. Fig. (a) is the baseline no-swirl solution. fig. (b) is the solution after the application of F.*

From fig. 4.6 we note that the flow features more elongated and narrower density lobes and that the density decays faster near the border, since the cross-field derivative is higher in magnitude. Moreover, the turning point is pushed downstream, leading to a less divergent plume, and eventually to

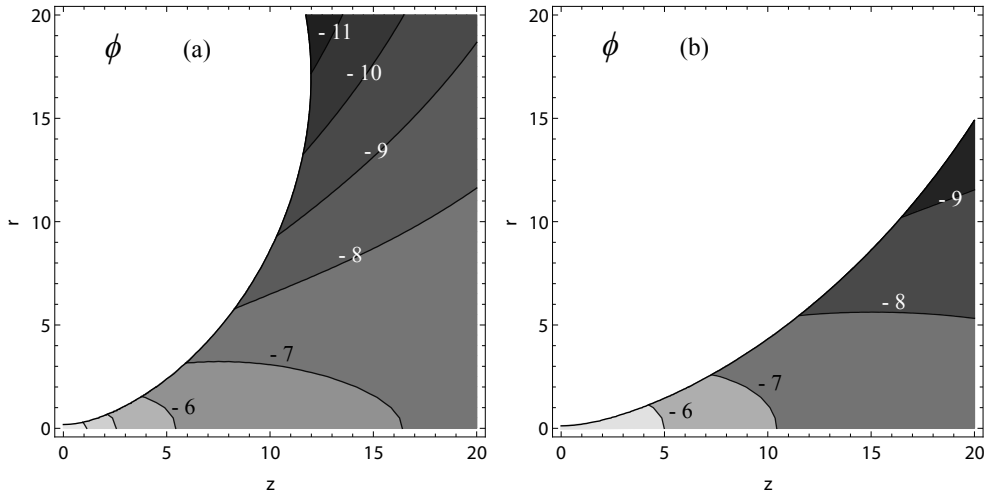

Figure 4.7: *Change in plasma flow potential for $\Omega = 2$. Throat radius $r_e = 0.185$. Magnetization parameter $\hat{\omega}_{lh} = 10$. Fig. (a) is the baseline no-swirl solution. fig. (b) is the solution after the application of F.*

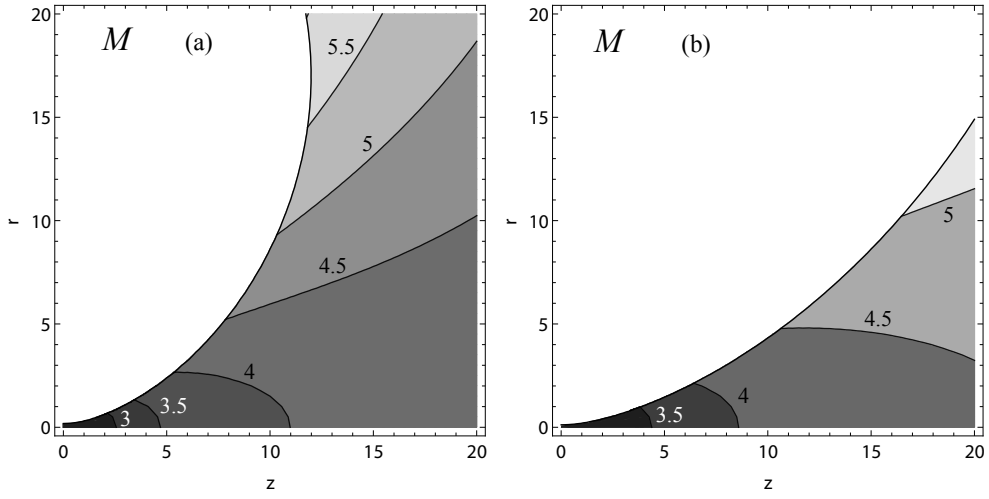

Figure 4.8: *Change in plasma flow Mach number for $\Omega = 2$. Throat radius $r_e = 0.185$. Magnetization parameter $\hat{\omega}_{lh} = 10$. Fig. (a) is the baseline no-swirl solution. fig. (b) is the solution after the application of F.*

higher nozzle efficiency and thrust coefficient. From fig. 4.8 we also note a faster acceleration of the plasma as it flows along the nozzle. We explain this phenomenon by noting that, due to the modified density profile of fig. 4.5, in the focused case there is a stronger concentration of thermal energy in the central region than in the reference situation. Thus, the thermal expansion

is more vigorous and the axial acceleration faster.

By comparing the flow before and after the introduction of the body force, we also see that most of the effect occur in the central portion of the plume, where the difference in the two cases is stronger. This, in turn, would favor the increase in the nozzle performances, since most of the momentum is carried in the central region of the plume.

Chapter 5

Propulsive Applications

5.1 Introduction

In this Chapter, we use the modified nozzle flow solution to assess the effects of the azimuthal current on the propulsive performances of the magnetic nozzle. First, we recall Little and Choueiri's efficiency model and we carry out and discuss the assessment of such a performance increase. Then, we use the results of the analysis to propose a number of designs for focusing stages to be implemented between the plasma source and the nozzle throat for the introduction of the electronic azimuthal current.

5.2 Propulsive Performance Assessment

5.2.1 Efficiency Model

We define the divergence efficiency of the nozzle as the ratio between the axial kinetic power in the plume and the total kinetic power, both taken at the magnetic field turning point ζ_{tp}. Under quasi-field aligned assumption, this ratio reads

$$\eta_{\text{div}} = \frac{\mathcal{P}_b^*}{\mathcal{P}_b} = \int_{\zeta_{tp}} nM^3 \frac{B_z^2}{B^2} dA \Big/ \int_{\zeta_{\text{tp}}} nM^3 dA \quad . \tag{5.1}$$

The choice of using the turning point as performance evaluation coordinate is sustained by recent simulations [3], which showed little momentum exchange

beyond $\zeta_{\rm tp}$, thus making of this position a suitable location for performance evaluation.

This divergence efficiency $\eta_{\rm div}$ differs from the overall nozzle efficiency, assumes the unity value for a perfectly axial flow and scales with the half width of the plume as $\cos^2(\theta_{\rm div})$. While it is clear that a plume focusing affects mainly $\eta_{\rm div}$, other efficiencies might be affected too, as stated in previous Chapters. Indeed, a narrower plasma column couples better with an helicon wave and the ionization efficiency should rise accordingly. Finally, the plume is tight to a more internal magnetic surface, thus the wall losses should decrease too, increasing the overall thruster efficiency. The divergence efficiency is related to the overall nozzle efficiency through the relation $\eta_n = \eta_i\ \eta_{\rm div}$, where η_i takes into account all other sources of losses.

The thrust coefficient C_T is defined as

$$C_T = \frac{1}{\bar{n}_t A_t} \int_{\zeta_{tp}} n \left(M^2 + 1\right) \frac{B_z}{B} dA \quad , \tag{5.2}$$

where the quasi-field aligned hypothesis has again been used. The nondimentional thruster specific impulse depends on both η_n and C_T

$$\hat{I}_{\rm sp} = \frac{g_0 I_{\rm sp}}{c_s} = \eta_n C_T \quad . \tag{5.3}$$

Through the nozzle flow solution, we can also evaluate the plume divergence. Little and Choueiri derives an handy relation between the divergence half-angle $\theta_{\rm div}$ and a parameter $\Psi_{1/2}$ defined as the coordinate ψ/ψ_p at which the density at ζ_{tp} is half its value on the axis. This $\Psi_{1/2}$ is computed from the relation

$$\frac{n(\Psi_{1/2}, \zeta_{tp})}{n(0, \zeta_{tp})} = \frac{1}{2} \quad . \tag{5.4}$$

Since n_t is no longer a Bessel function, in our case this equation is solved numerically. Then, the divergence angle is computed as $\cos(\theta_{\rm div}) \approx 1 - \Psi_{1/2}$ [49].

5.2.2 Nozzle Performance Assessment

By solving numerically eq. (5.1) to (5.4), we compute the variation in nozzle divergence angle, divergence efficiency, thrust coefficient and specific impulse

due to the introduction of the body force F. The results, plotted versus the force parameter $\hat{\Omega}$, are reported in fig. 5.1 to 5.5, parameterized by the magnetization factor $\hat{\omega}_{\rm lh}$ and the throat radius r_e.

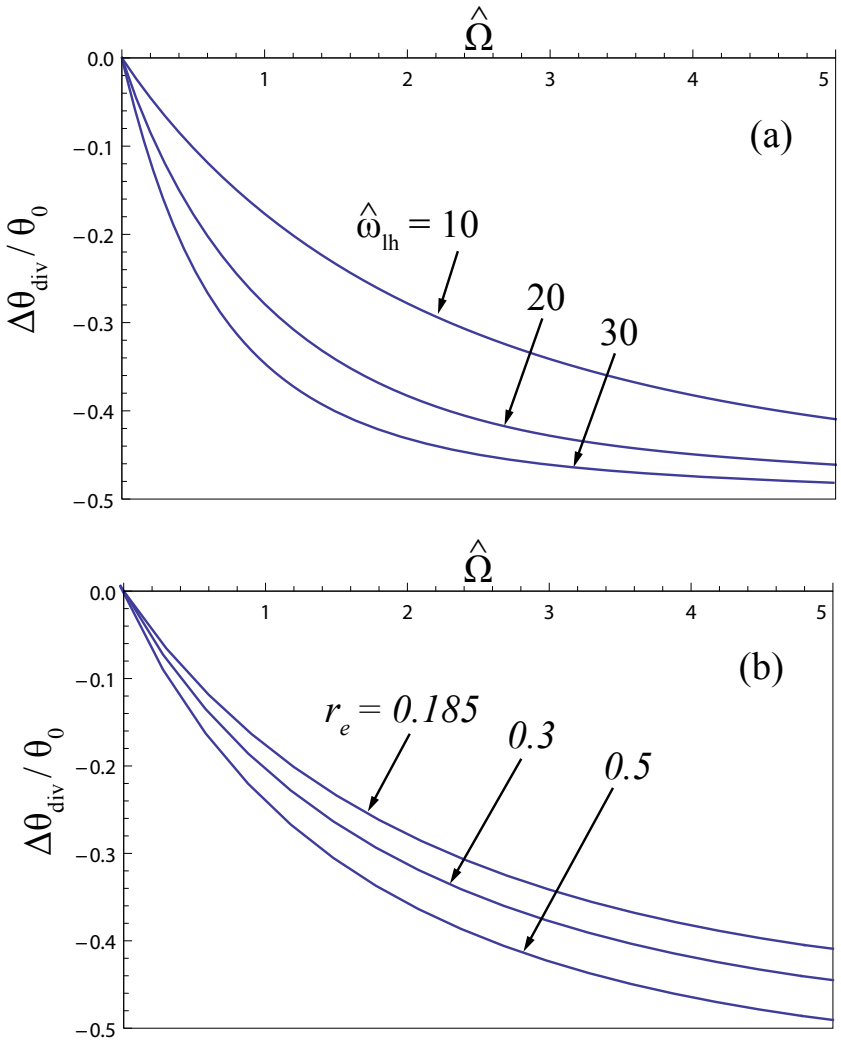

Figure 5.1: *Relative reduction in plume divergence with* $\hat{\Omega}$. *Throat radius* $r_e = 0.185$ *for graph (a). Magnetization parameter* $\hat{\omega}_{lh} = 10$ *for graph (b).*

From fig. 5.2, we see that the relative increase in efficiency follows the trend of fig. 8 of Little and Choueiri [49], reported here as fig. 5.3. It is clear that the reduction of the sheath coordinate has the same effect of a reduction of r_e, while the definition of divergence efficiency does not take into account the density scaling of eq. (4.46).

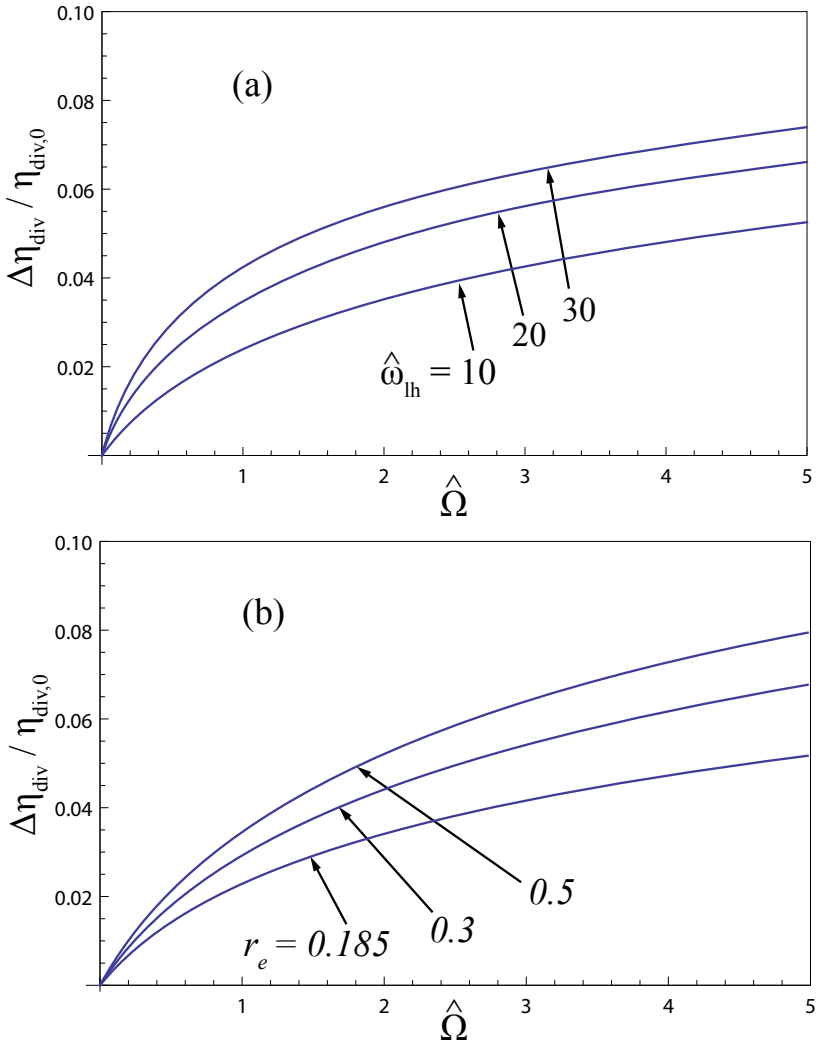

Figure 5.2: *Relative increase in nozzle divergence efficiency with $\hat{\Omega}$. Throat radius $r_e = 0.185$ for graph (a). Magnetization parameter $\hat{\omega}_{lh} = 10$ for graph (b).*

The divergency efficiency in fig. 5.2 qualitatively scales as the divergence decrease. We observe that, for $r_e = 0.185$, $\hat{\omega}_{\rm lh} = 30$ and $\hat{\Omega} = 5$ it can reach values above 0.9, with a plume half-angle below 15 degrees.

While this raise in $\eta_{\rm div}$ is already relevant, we note that a much higher increase is recorded for the thrust coefficient, as plotted in fig. 5.4. Specifically, the relative increase of C_T is almost one order of magnitude more than the one of the efficiency, and reaches values of about 40% in the initially low-efficient situation of $r_e = 0.5$ with $\hat{\omega}_{\rm lh} = 10$. The physical explanation

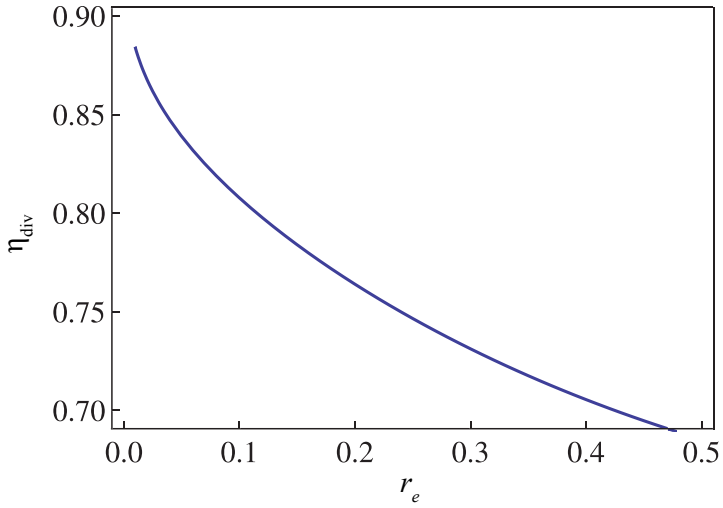

Figure 5.3: *Analytical approximation of beam divergence efficiency, η_{div}, versus the plasma radius at the throat r_e [49].*

for this predominance of $\Delta C_T/C_{T0}$ over $\Delta\eta_{\rm div}/\eta_{\rm div0}$ comes from the definition of these two parameters. Indeed, we observe that the efficiency increase accounts only for the reduction of the sheath coordinate R_s, while the thrust coefficient is influenced also by the increase in value of the density peak in the center as of fig. 4.5.

From eq. (5.3) we can also plot the increase in specific impulse, which will be a combination of the trends of $\eta_{\rm div}$ and C_T, being

$$\frac{\Delta\hat{I}_{\rm sp}}{\hat{I}_{\rm sp0}} = \frac{\Delta\left(C_T\ \eta_{\rm div}\right)}{C_{T0}\ \eta_{\rm div0}} \quad . \tag{5.5}$$

From these fig. , we see that a stronger effect is achieved for initially high values of r_e, which is for initially low-efficient designs of the nozzle [3, 49]. Therefore we might think to exploit such an azimuthal current for designing plasma thrusters with smaller nozzle coils, thus with reduced power losses, without jeopardizing the efficiency. As an example, given a value for the throat radius, we can design a thruster with $r_e = 0.3$ (coil radius thrice the throat) and recover the same thrust coefficient of the case $r_e = 0.185$ (coil radius more than five times the throat) by setting $\hat{\Omega} \approx 2.6$, as can be seen in fig. 5.6.

As noted in section 4.3.3, an higher grade of magnetization (high $\hat{\omega}_{\rm lh}$)

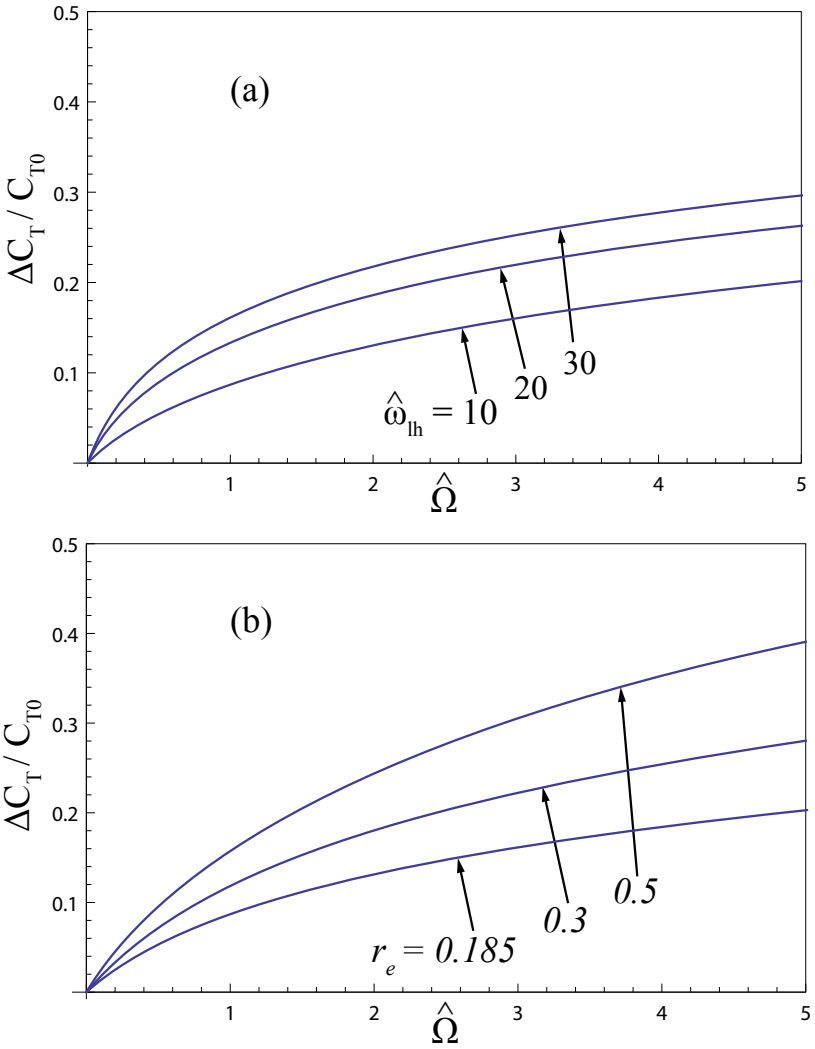

Figure 5.4: *Relative increase in nozzle thrust coefficient with* $\hat{\Omega}$. *Throat radius* $r_e = 0.185$ *for graph (a). Magnetization parameter* $\hat{\omega}_{lh} = 10$ *for graph (b).*

strengthens the effect, accentuating the knee below $\hat{\Omega} \approx 1.5$. For high values of $\hat{\Omega}$ we see a stabilization in the difference between the performance at different values of magnetization, while this difference monotonically increases if the curves are parametrized according to r_e. This might suggest that an high value of $\hat{\omega}_{\rm lh}$ is convenient only if $\hat{\Omega}$ is kept relatively low.

These results makes this concept a promising mean to increase the nozzle efficiency for all the applications where magnetic nozzles have place, even outside the field of plasma propulsion. Indeed, such focusing system would

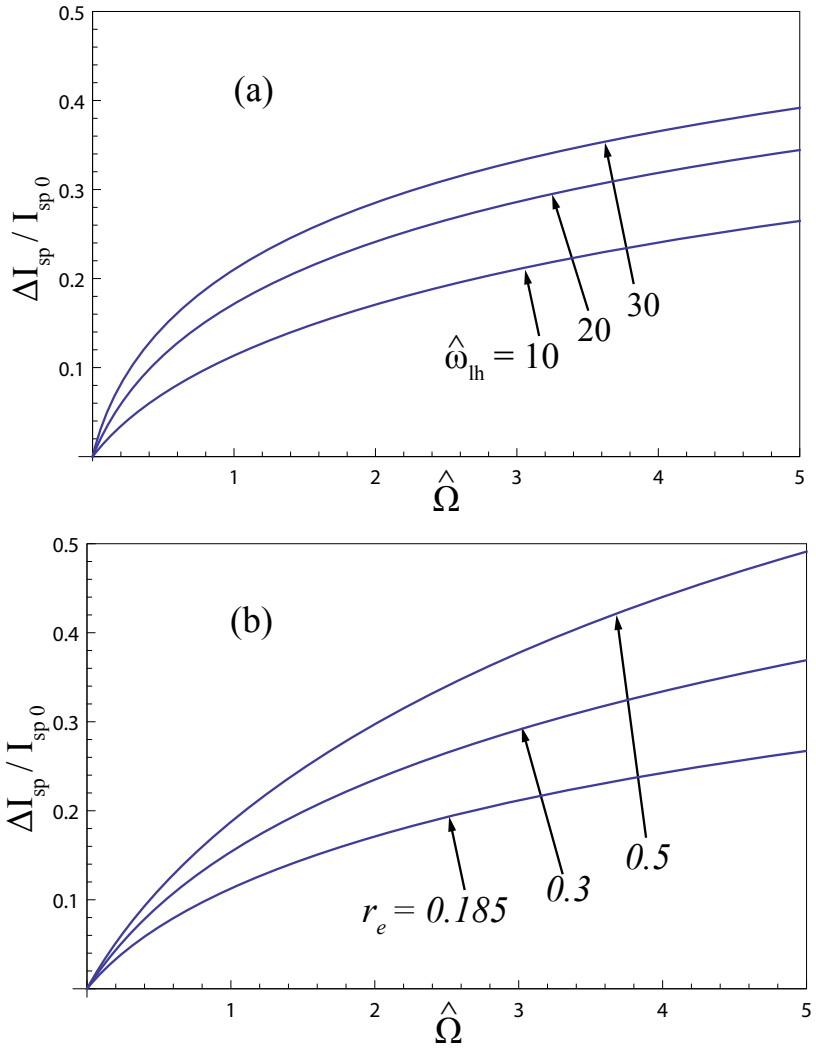

Figure 5.5: *Relative increase in normalized specific impulse $\hat{I}_{sp}$ with $\hat{\Omega}$. Throat radius $r_e = 0.185$ for graph (a). Magnetization parameter $\hat{\omega}_{lh} = 10$ for graph (b).*

provide a way to actively tune the width of the plasma plume, a degree of freedom that can be very useful, for example, for plasma surface processing.

This system is obviously not exempt from problems. Indeed, an high value of electronic swirl might raise the efficiency loss observed by Ahedo and Merino due to the outward separation of the electron stream surface. Moreover, at relatively high $\hat{\Omega}$, the induced diamagnetic magnetic field starts being relevant. This leads to a reduction of the axial magnetic field, with consequent increase in the magnetic field lines divergence and wall losses

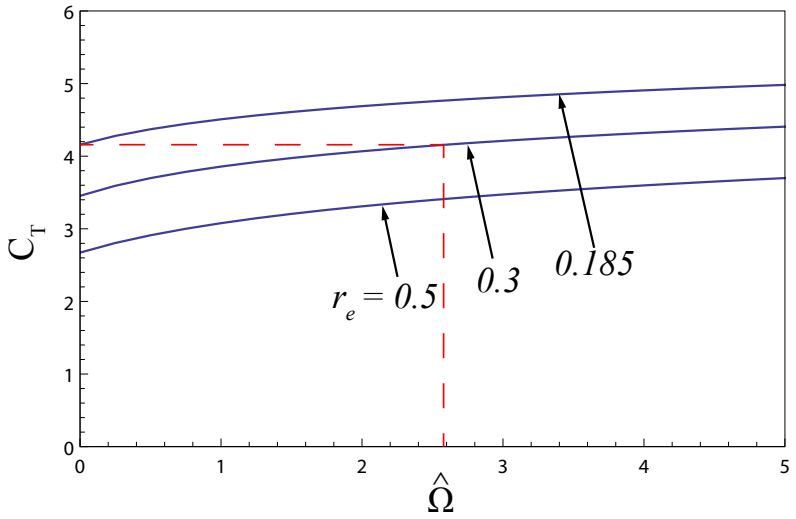

Figure 5.6: *Absolute increase in nozzle thrust coefficient with* $\hat{\Omega}$*. Magnetization parameter* $\hat{\omega}_{lh} = 10$*. The red lines mark the example reported in the text, where we show that we can recover the same thrust coefficient of the case* $r_e = 0.185$ *by setting* $r_e = 3$ *and* $\hat{\Omega} \approx 2.6$*.*

[4]. Eventually, an high enough induced magnetic field would lead to field-reversed configurations [69], jeopardizing the EDMN field topology. However, the physical model here described would fail far before reaching this extreme.

5.3 Power Assessment

To assess the efficiency of the force $\hat{F}$ in increasing the performances of the overall thruster, we can plot the ratio between the increase in the axial jet power and the force power $\Delta\mathcal{P}_b^*/\mathcal{P}_{\hat{F}}$, where $\mathcal{P}_b^*$ and $\mathcal{P}_{\hat{F}}$ are defined from eq. (5.1) and eq. (4.24), respectively, and reported here in eq. (5.6).

$$\begin{cases} \mathcal{P}_b^* = \int_{\zeta_{tp}} nM^3 \dfrac{B_z^2}{B^2} dA \\ \mathcal{P}_{\hat{F}} = \int_{A_t} \hat{F}\ n\ \hat{u}_{\theta e} \sqrt{\dfrac{m_i}{m_e}} dA \end{cases} . \tag{5.6}$$

As clear from fig. 5.7, the axial power gain overcomes the power introduced by the focusing stage. We must clarify that this increase in the axial power comes from a better conversion of the overall jet power $\mathcal{P}_b$ and not from $\mathcal{P}_{\hat{F}}$

since the force $\hat{F}$ acts only as a mean for a better conversion of thermal power to axial kinetic power, and not as a net power source for the jet. Thus, the overall efficiency remains below the unity.

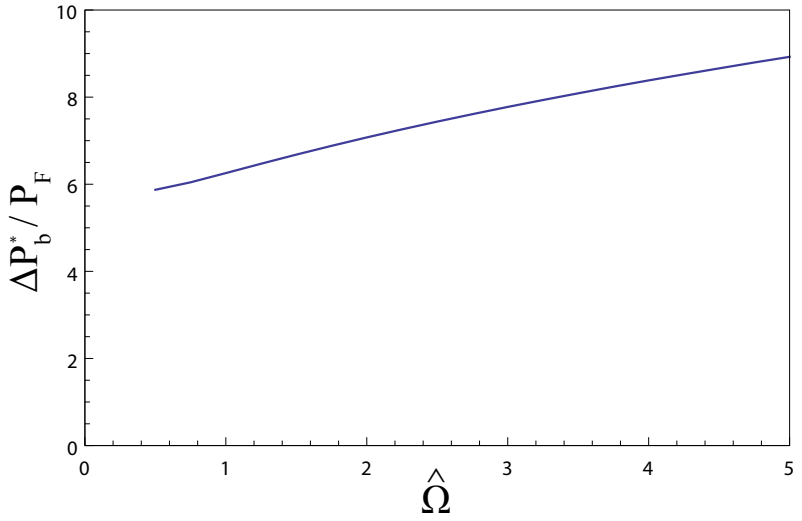

Figure 5.7: *Ratio between jet axial power increase due to azimuthal curent and body force power. Magnetization parameter $\hat{\omega}_{lh} = 10$, throat radius $r_e = 0.185$. The plot is limited to $\hat{\Omega} \geq 0.5$, since the limitations of our definition of $\hat{F}$ described in section 4.3.4 lead to unphysical results for lower $\hat{\Omega}$.*

We could state that the same power $\mathcal{P}_{\hat{F}}$ used for the focusing stage could be used to directly increase the power of the jet, for example by heating the electron fluid to an higher T_e. Thus, we can compare the effects of this temperature increase with those of the introduction of the azimuthal momentum source. In other words, we can plot the ratio between the axial power in swirling regime $\mathcal{P}^*_{\mathrm{b,S}}$ and the axial power in augmented temperature regime $\mathcal{P}^*_{\mathrm{b,H}} = \eta_{\mathrm{div},0}\,(\mathcal{P}_b + \mathcal{P}_{\hat{F}})$.

From fig. 5.8 we see that the ratio $\mathcal{P}^*_{\mathrm{b,S}}/\mathcal{P}^*_{\mathrm{b,H}}$ is always greater than the unity. This means that the axial power recovery in the jet due to the introduction of $\hat{F}$ is higher than the axial power gain due to an augmented overall power in the jet. This result eventually makes of the concept of focusing stage a promising mean to overtake the well-known difficulties in increasing the electron temperature in helicon plasmas [73].

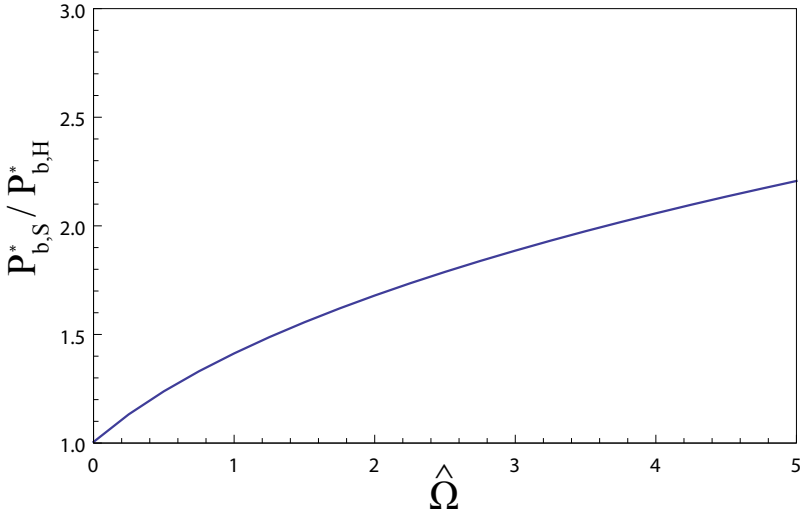

Figure 5.8: *Ratio between jet axial powers in swirling ($\mathcal{P}^*_{b,S}$) and increased electron temperature ($\mathcal{P}^*_{b,H}$) regimes. Magnetization parameter $\hat{\omega}_{lh} = 10$, throat radius $r_e = 0.185$.*

5.4 Focusing Stage Design

The results obtained in the previous sections clearly showed the benefits of the implementation of a focusing stage. Thus, we wish now to deal with the engineering problem of actually designing such a system in a way that might be suitable for in-space applications.

In literature, a number of different techniques has been identified to drive an azimuthal electron current in a magnetized plasma column [10, 16, 38, 52, 65, 70, 74]. In this section, we will revise three of them, which we have identified to be the most promising ones, and we will proceed with a preliminary design of a focusing stage based on each of those concepts. Particular attention will be paid to the description of the underlying physics and the pros and cons of each solution. The helicon plasma source used at the Electric Propulsion and Plasma Dynamics Laboratory (EPPDyL) of Princeton University will be used as a reference for the conceptual design.

5.4.1 Magnetic Step Field Architecture

A steep variation of the axial magnetic field magnitude is a first way to induce both species of the plasma to start a counter-rotating swirl motion.

This acceleration occurs in order to preserve the magnitude of the angular momentum H_a along each species' flow streamline:

$$m_a r u_{\theta \mathrm{a}} + q_a \psi = H_a \quad . \tag{5.7}$$

An abrupt change in magnetic field is required in order to force the fluid particles to diffuse crossing the magnetic streamlines and achieving the $\Delta\psi$ that eventually drives the azimuthal acceleration. Taking an initially fully axial flow, we can write the conservation of angular momentum across the magnetic step

$$q_a \psi^i = m_a r u^f_{\theta \mathrm{a}} + q_a \psi^f \quad , \tag{5.8}$$

where ψ^i and ψ^f are the initial and final magnetic stream coordinate of the fluid particle. Then, we can derive a sizing relation for the magnetic field step, which depends on the value of azimuthal velocity we want to achieve

$$\left(\psi^i - \psi^f\right) = \frac{m_a r^2}{q_a} \omega^f_a \quad , \tag{5.9}$$

being ω^f_a the angular velocity we want to achieve at the throat. We note immediately that, to get the diamagnetic current we need, such variation shall be negative

$$\Delta\psi = -\left(\psi^i - \psi^f\right) < 0 \quad , \tag{5.10}$$

which means that the axial magnetic field B_z shall increase across the step. Specifically, if we wish to get the half-cyclotron frequency of eq. (3.19), the magnetic field shall double. A conceptual scheme of such device is depicted in fig. 5.9.

This phenomenon has been experimentally proven for non-neutral electron plasma [72], but it is believed to occur also for neutral plasmas [65]. This method has the huge advantage of being passive, which means that no power is provided to the plasma: the energy to induce the azimuthal rotation is taken from the axial flow and is then recovered in the divergent section by means of the accelerating term, but the flow results more collimated because of the focusing effect. Obviously, some power will be needed for feeding the eventual coils used to create the magnetic step. Moreover, we see that both species are swirled and both contribute to the azimuthal current.

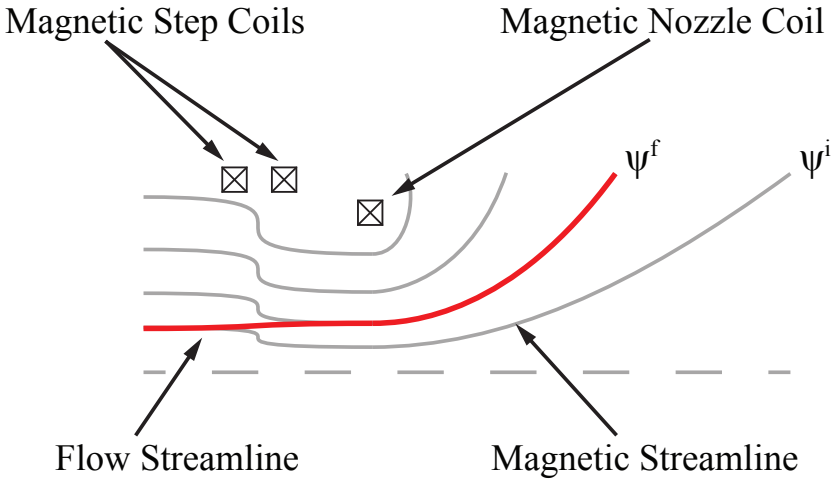

Figure 5.9: *Schematics of flow and magnetic streamlines with a magnetic step before the nozzle throat. The flow is tight to the magnetic streamline up to the step, where suddenly transitions to a different field line.*

An adverse effect would be the insurgence of magnetic mirroring effects which may confine part of the plasma before the nozzle throat and would slow down the motion of the plasma itself along the streamline. Moreover, to practically create such an abrupt change in the magnetic field might be tricky. Other disadvantages may come from poor confinement and ionization efficiency in the plasma source because of the lower magnetic field before the step.

5.4.2 Concentric Electrodes Architecture

A very simple mean for driving an azimuthal current would make use of the Hall effect in a magnetized plasma column. Let us take the generalized Ohm's law:

$$\mathbf{E} + \mathbf{u} \times \mathbf{B} = \frac{1}{ne}\mathbf{J} \times \mathbf{B} - \frac{1}{ne}\nabla \cdot \mathbf{P} + \underline{\underline{\eta}}\mathbf{J} \quad , \tag{5.11}$$

where $\mathbf{P}$ and $\underline{\underline{\eta}}$ are the pressure and the resistivity tensors, respectively, and all other symbols are conventional. If we consider only the radial direction and a diagonal resistivity tensors, we get

$$E_r = \frac{1}{ne}J_\theta B_z - \frac{1}{ne}\nabla_r P + \eta_r J_r - u_\theta B_z \quad , \tag{5.12}$$

where also the viscous losses have been neglected. Recalling that $\mathbf{J} = ne(\mathbf{u_i} - \mathbf{u_e})$ and $\eta_r = m_e \nu_{\mathrm{ei,r}}/e^2 n$, we have:

$$\frac{E_r}{B_z} = -\left(u_{\theta \mathrm{e}} + \frac{m\nu_{\mathrm{ei,r}}}{eB_z} u_{\mathrm{r\ e}} + \frac{(ne)^{-1}\nabla_r P}{B_z}\right) \quad , \tag{5.13}$$

or

$$\frac{E_r}{B_z} = -\left(u_{\theta \mathrm{e}} + \frac{1}{\beta_H} u_{\mathrm{re}}\right) \quad , \tag{5.14}$$

where β_H is the Hall parameter, defined as the ratio between the cyclotron (Ω_e) and collisional (ν_{ei}) frequencies. The thermoelectric term is neglected because is much lower than $u_{\theta \mathrm{e}}$, especially in the peripheral regions, where the density gradient vanishes, as from section 4.3.3. We see that, in a high-β_H plasma, an applied radial electric field E_r induces mainly an azimuthal electron current $u_{\theta \mathrm{e}}$. Indeed, the Hall parameter can be seen as the trigonometric tangent of the angle between the current density $\mathbf{J}$ and the applied electric field $\mathbf{E}$ [38]. Thus, a very high β_H gives a current almost perpendicular to the electric field or, in our case, azimuthal. This functioning mechanism recalls the pinching effect of Hall currents in applied field MPD [17, 28, 38, 41].

It is common [38] to have situation where the Hall parameters of electrons and ions differ greatly from each other. In these situations, the concentric electrodes focusing stage would drive both a radial ion current and an azimuthal electron current.

In fig. 5.10 is depicted a scheme of the design of an electrode-based focusing stage applied to an planar antenna helicon plasma source.

The main advantage of the electrode-based focusing stage concept is its intrinsic simplicity of manufacturing, implementation and operation. However, as one could expect, this simplicity is paid by a number of relevant disadvantages. First of all, the presence of electrodes inside the plasma is a source of inefficiencies due to RF coupling wave and wall losses. These losses are particularly relevant on the cathode, since the plasma is much denser in the central region of the column. The presence of electrodes inside the plasma may also cause sputtering problems with eventual contamination of the external surface of the spacecraft, in case of space application, or of the diagnostic. The sputtering is also expected to increase scaling with the plasma density and temperature, thus the electrode focusing stage ill couples

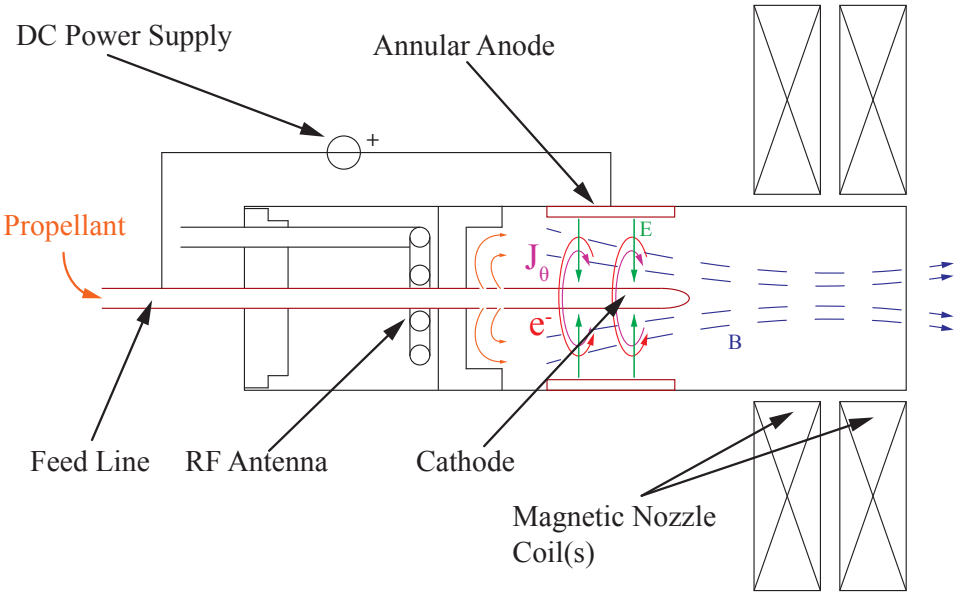

Figure 5.10: *Schematics of focusing stage based on Concentric Electrodes architecture applied to an helicon plasma source with planar antenna.*

with an high power thruster. Moreover, much of the applied voltage between the electrodes is spent inside the sheath and the boundary layer [22, 24] , leaving only a fraction of this potential drop to occur in the plasma bulk region, where the Hall current is induced.

Finally, the cylindrical geometry leads to an higher electric field in the center of the column with respect to the peripheral region. Eventually, a higher Hall current is expected closer to the axis, while for focusing purposes we would desire to have more action in the external portion of the plasma.

5.4.3 Rotating Magnetic Field Architecture

Another widely studied mean to drive an azimuthal current in a cylindrical theta-pinch plasma confinement configuration makes use of a Rotating Magnetic Field (RMF). In this architecture, a rotating transverse magnetic field couples with the electrons and drags them in a rigid-body azimuthal rotation at the same angular frequency [69], thus driving a net current. A practical way of introduce such RMF is to use a set of two or more antennas distributed around the column. By phase-shifting the signal depending on the angular

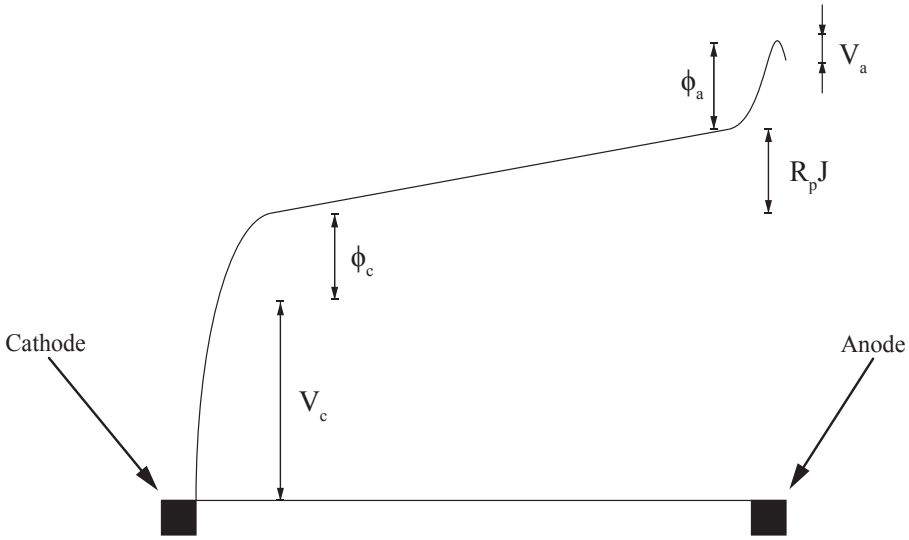

Figure 5.11: *Qualitative distribution of the potential across the plasma between the electrodes. V_c, V_a, ϕ_c and ϕ_a are the potential drops across the cathode and anode sheaths and the boundary layer, respectively. R_pJ is the potential drop across the bulk of the plasma [22].*

displacement of each antenna, a constant-magnitude rotating magnetic field can be induced. This concept finds applications, among others, in the field of nuclear fusion research, specifically in the Reversed Field Configuration architecture [70], and spacecraft propulsion, with the pulsed Electrodeless Lorentz Force thruster (ELF) [68].

The main issue with RMF current-drive experiments is the difficulty in achieving a steady-state condition with non-zero current. Indeed, as soon as the electrons are entertained with the rotating field, the ion-electron collisionality drags the ions, reducing the differential motion of the species, eventually vanishing the azimuthal current [34, 69]. The accessibility of a steady state regime, the so called *Clemente state* [19], where two counter-rotating RMFs drives the two fluids has been studied by Hugrass [33, 34] and Visentin [75], leading to a very promising configuration which waits to be confirmed by experiments.

However, in our specific case, we may be able to produce a steady state functioning regime even without reaching the Clemente state. Indeed, we

can design the focusing stage in such a way to have a residency time of the flow in the thruster higher than the penetration time of the RMF, but lower than the characteristic time of azimuthal current dissipation. In such a way, the flow will stay inside the focusing stage long enough to experience the confining effect of the RMF, but not enough to see such an effect vanishing. This goal can be achieved by tuning the RMF magnitude and frequency, and by correctly sizing the antennas. A conceptual design of this focusing stage can be found in fig. 5.12.

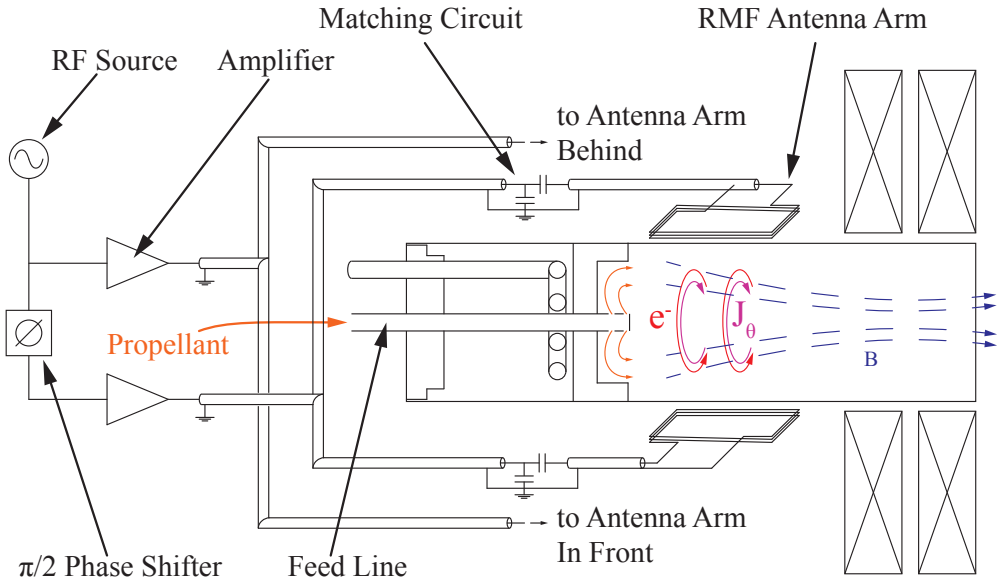

Figure 5.12: *Schematics of focusing stage based on Rotating Magnetic Field architecture. The signal produced by an RF source is split into two signals, one of which is phase-shifted by $\pi/2$ radians. Then, the signals are amplified and, through coaxial cables or waveguides, are sent to the two sets of antennas. Matching circuits, made of series and shunt variable capacitors, and are implemented to match the antenna impedance and avoid reflected power [63]*

As a case study, we can design such RMF focusing stage using geometrical characteristics and typical plasma parameters of the EPPDyL magnetic nozzle experiment, reported in tab. 5.1. Using Argon and the electron temperature reported in tab. 5.1, we get a sound speed of $c_s = 3418\ m/s$. Adopting this value as characteristic velocity of the flow in the plasma source, we get a residence time t_r of 0.043 ms.

Quantity	Value	
Density	n	$3 \cdot 10^{18}\ m^{-3}$
Ion Temperature	T_i	$\sim 0\ eV$
Electron Temperature	T_e	$5\ eV$
Electron-Ion Collision Frequency	ν_{ei}	$4.8511 \cdot 10^{6}\ s^{-1}$
Axial Magnetic Field	B_z	$200\ G$
Length of Focusing Stage	L	$0.150\ m$
Radius of Plasma Source	R	$0.035\ m$

Table 5.1: *Plasma parameters and physical characteristics used for the case-study design of RMF stage. Data from the Magnetic Nozzle experiment at EPPDyL [48].*

To estimate the penetration time of the RMF we follow the approach presented by Milroy [54, 55]. In his simulations, Milroy developed handy empirical expressions to find the characteristics of the RMF in order to achieve and maintain full penetration in the column. He derived that these requirements are function of two parameters: the ratio λ between the column radius r_e and the skin depth δ, and the ratio γ_ω of the electron cyclotron frequency computed using the RMF field $\Omega_{\mathrm{e},\omega}$ and the electron-ion collision frequency, ν_{ei}. Thus, to achieve the entertainment of all the plasma column, the following inequalities shall be met:

$$\begin{cases} \lambda > 6.5 \\ \\ \gamma_\omega > \gamma_{\omega \mathrm{c}} = 1.12\lambda \left(1 + 0.12\left(\lambda - 6.5\right)^{0.4}\right) \end{cases} , \tag{5.15}$$

while, to maintain the penetration, we need to have

$$\gamma_\omega > 1.12\lambda \quad . \tag{5.16}$$

Using the data from tab. 5.1, we get $\lambda = 11.3$, thus $\gamma_\omega = \omega_{\mathrm{ce}} / \nu_{\mathrm{ei}} > 15.4847$. Then, using these requirements, we can compute a minimum value for the magnitude of the rotating magnetic field

$$B_\omega > B_{\omega,\min} = 15.4847\ \nu_{\mathrm{ei}} \frac{m_e}{q} = 4.27G \quad . \tag{5.17}$$

The characteristic time of the penetration is:

$$\tau_\omega = t\ \omega \approx \frac{\lambda^2}{2\sqrt{\gamma_N}} \quad , \tag{5.18}$$

where ω is the angular frequency of the RMF and γ_N is defined as

$$\gamma_N = \frac{\gamma_\omega - \gamma_{\omega c}}{\gamma_{\omega c}} \quad . \tag{5.19}$$

Therefore, if we impose to have full penetration before the nozzle throat, we can relate the characteristic time with the physical length of the device by using the characteristic velocity. Following this logic, we get to a relation between the magnetic field and the frequency of RMF

$$B_\omega > \frac{m_e \nu_{ei} \gamma_{\omega c}}{q} \left(1 + \left(\frac{\lambda^2}{2t_r}\right)^2 \frac{1}{\omega^2}\right) \quad . \tag{5.20}$$

We see that the minimum value of magnetic field decreases by increasing the frequency of the RMF, and shows an horizontal asympthote at $B \to B_{\omega,\min}$ for $\omega \to \infty$.

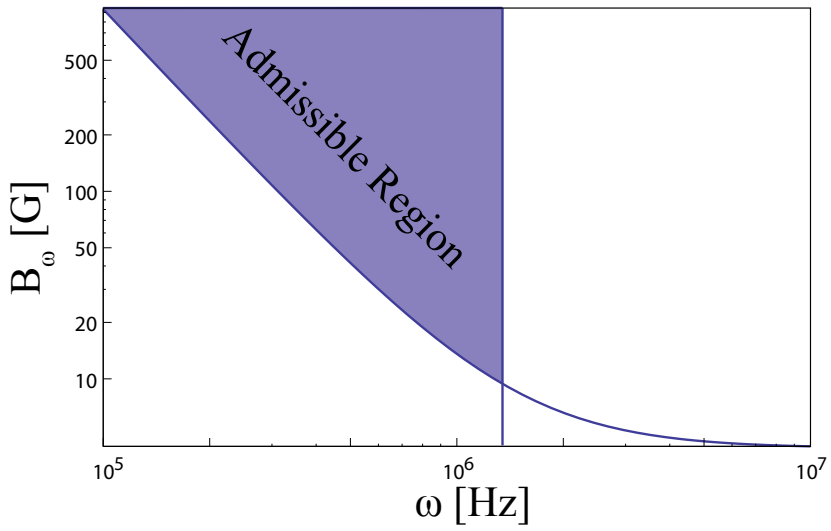

Figure 5.13: *Working region for full RMF penetration in the plasma column and reduced current dissipation, with imposed $t = t_r = 0.043\ ms$. All the points inside the admissible region are valid solution of the system of inequalities* (5.20) *and* (5.21)*, hence give a full penetration without significant current dissipation in less than t_r.*

Estimating the characteristic time of the current dissipation is rather difficult [42, 54, 55, 69]. Taking the numerical simulations of Lifschitz et al., we see that for our range of RMF parameters (λ, γ) and a fully ionized gas,

the ion motion approximately matches the electrons after about 60 periods of the RMF. Thus, we impose

$$\omega < \frac{60}{t_r} \quad . \tag{5.21}$$

This requirements is relaxed if the gas is not fully ionized because the ion-neutral friction would preserve the electron-ion differential motion. Using the values of tab. 5.1, we can plot the eq. (5.20) and (5.21) to get the admissible region for full RMF penetration and reduced current dissipation in the imposed length.

The RMF architecture presents a number of advantages. First of all, the possibility of tuning the frequency and the magnitude of the rotating magnetic field allows great operative flexibility. Also, due to the rigid-body velocity profile of the electrons when driven by the RMF, most of the power is spent in the external region of the plasma column, which are the regions we want to affect the most. Moreover, no electrodes are required and the RMF technology is mature and well known from years of research in Reversed Field Configurations nuclear fusion reactors.

The main drawback of this concept is the complexity of the system, which requires at least two (if not four or more) additional antennas with the relative matching circuits, amplifiers and RF source. Therefore, we believe that such an architecture might find application in high-power high-size MN-based thrusters, rather than in small and simpler low power engines.

Chapter 6

Experimental Proof of Concept

6.1 Introduction

In this Chapter we present an experimental setup for investigating the feasibility and characterize the behavior of one of the architectures of focusing stage introduced in section 5.4. After presenting the goals of our experimental work, we describe the equipment and diagnostic used for this study. Then, the setup of the experiment and the results are presented and discussed. In the last section of the Chapter, some conclusions are drawn and possible future developments are proposed.

This experimental investigation has been carried on using the magnetic nozzle experiment recently built at the Princeton Electric Propulsion and Plasma Dynamics Laboratory (EPPDyL), properly modified for the purposes of this study.

6.2 Objectives of the Experiment

The theory and analytical simulations developed open the possibility of an experimental proof of concept for the implementation of the *Focusing Stage* conceived in section 5.4.

Thus, the high level goal of this experiment is to prove the positive effects on nozzle efficiency of an applied azimuthal electron current. According to the proof-of-concept nature of this investigation, we do not claim to reach

an optimal operation or sufficient technology readiness for the implementation on an actual plasma thruster. Among the presented designs, the most suitable focusing stage would make use of the RMF technology, as described in section 5.4. However, the same section 5.4.3 describes that such system would require the implementation of an additional RF source, two amplifiers, a phase delay, two matching networks and four antennas. Therefore, it was agreed internally in the EPPDyL laboratory that, for the purposes of this experiment, the less performing but much simpler and cheaper electrode architecture has to be chosen for the implementation.

Then, the main objectives were: to investigate in steady state the ability of one of the focusing stage designs to drive an azimuthal current; to assess the effect of the focusing stage on the density and potential transversal distribution inside the thruster; to verify that a net effect is propagated outside in the plume, with beneficial effect to the focusing of the jet. No flow velocity measurements were planned to investigate effects on the plume axial acceleration. Since the selected technology differs from the theoretical model of body force previously described, we cannot use such a theory to quantitatively predict the performances of the present experiment. However, as will be clear from the results, many predicted trends and effects are actually found in practice.

6.3 Equipment

6.3.1 Plasma Source

The magnetic nozzle experiment at EPPDyL consists of an helicon plasma source enclosed in a borosilicate glass tube of 35 mm in radius and a couple of magnetic coils for the induction of the magnetic nozzle field topology. The operating gas is argon, ionized by means of a two-turn planar copper antenna operating at 13.56 MHz. The propellant feedline is coaxial with the antenna and a Macor movable backplate. The RF signal is generated by an Agilent 8648B Signal Generator. Two amplifiers (ENI 2100L pre-amplifier and Alpha 9500) in series provide up to 1 KW of RF power for ionization and plasma heating. An Alpha 4520 digital wattmeter is used to measure the standing-

wave ratio (SWR) and the delivered power. No independent plasma heating stage is implemented. The antenna matching is achieved by a L-type tunable custom-built capacitors network. The plasma source, pictured in fig. 6.1, is coated by a copper net for preventing the helicon RF wave to escape the glass tube. The nozzle electromagnets are made of 144 turns (12 x 12) of AWG 10 square, copper magnet wire wrapped on an aluminum core. The whole electromagnet has an effective radius of $a_e = 7.51$ cm. The coils are powered by an Amrel SPS32 DC power supply, operated in current control. The downstream electromagnet is aligned with the end of the glass tube and the magnetic nozzle throat is located between the two coils.

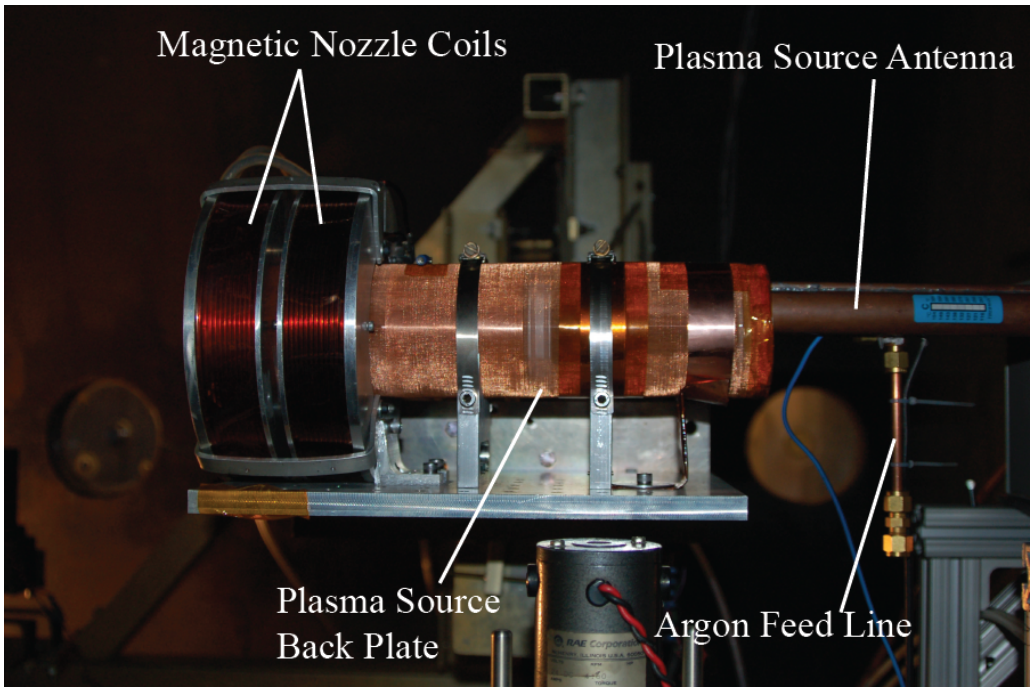

Figure 6.1: *Plasma source in use for the Magnetic Nozzle experiment at the Electric Propulsion and Plasma Dynamics Laboratory (EPPDyL) of Princeton University.*

The experiments is assembled within the EPPDyL's Large Dielectric Pulsed Propulsion vacuum chamber. The fiberglass chamber measures approximately 2.5 m in diameter and 7.5 m in length. The vacuum is provided by a three-stages vacuum system composed by a couple of Stokes mechanical roughing pumps, a roots blower and a CVC diffusion pump, capable of achieving pressures as low as 2×10^{-6} Torr, or 0.27 mPa. The antenna is wa-

ter cooled, while the electromagnets are passively cooled. Thus, experimental runs are limited to two hours to avoid excessive heating of the electromagnets. The temperature is monitored using a FLIR infrared camera.

The typical plasma parameters recorded in this experiment, operating in helicon mode, are reported in tab. 6.1.

Quantity	Value
n	$3\ to\ 6 \cdot 10^{18}\ m^{-3}$
T_i	$\sim 0\ eV$
T_e	$5\ to\ 10\ eV$

Table 6.1: *Typical plasma parameters recorded at Magnetic Nozzle experiment at EPPDyL [48].*

6.3.2 Diagnostic

The diagnostic is composed by a set of three in-house designed and manufactured probes: double-sided and single-sided Langmuir probes and a multi-purpose probe implementing both an emissive probe and a Mach probe.

The physics governing these probes is described by the plasma sheath theory, and will not be revised in this work. We will limit the following review only to the results useful for our experimental investigation.

Langmuir Probe Simply speaking, a Langmuir probe is a conducting surface immersed in the plasma flow (periodically) biased in voltage. The presence of an electrode inside the plasma produces a sheath, a thin non-neutral region that Debye-shield the bulk of the plasma flow from the perturbation introduced by the presence of the electrode. By measuring the current flowing to or from the sheath at different applied bias, we can draw the voltage-current characteristic curve. The analysis of such a curve can be used for computing the plasma density and electron temperature.

The electron temperature can be computed using by fitting the linear portion of the voltage-current natural logarithm curve. For the ion-unmagnetized

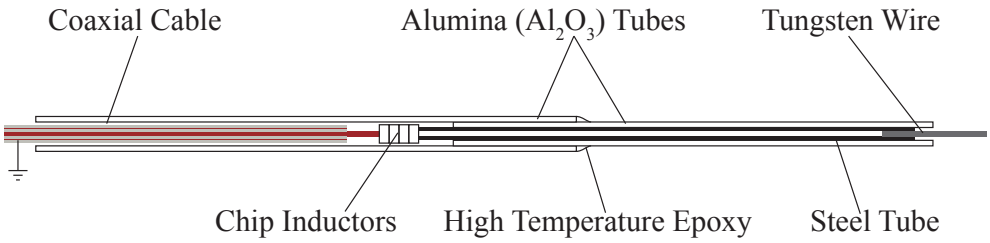

Figure 6.2: *Schematics of the Langmuir probe in use for EPPDyL magnetic nozzle experiment. Tungsten and Alumina are used for their resistance to high-temperature plasmas. The series of four chip inductors self resonates at 14 MHz and 28 MHz and is used to reject the RF signal picked up by the probe from the helicon wave.*

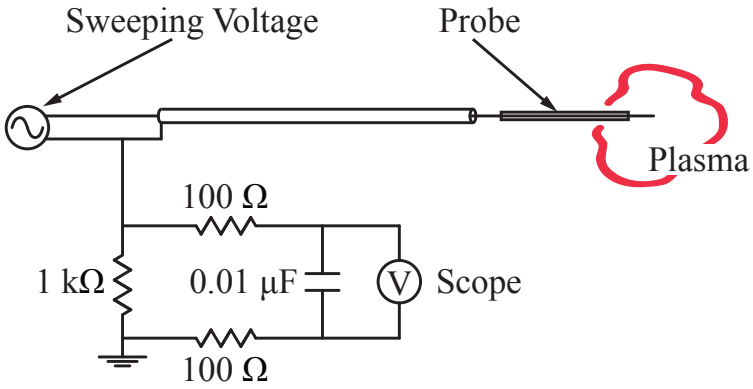

Figure 6.3: *Langmuir probe circuit. A low-pass filter is used to reject the high-frequency component of the signal before the scope.*

plasma under analysis, the temperature in Joule is simply [36]

$$T_e = e \Big/ ln\left(\frac{d\,|I - I_{\text{is}}|}{dV}\right) \quad , \tag{6.1}$$

where I_{is} is the ion saturation current, which is the current flowing in the Langmuir probe when the applied voltage is highly negative and the current curve approaches an horizontal asymptote. The slope $d\,|I - I_{\text{is}}|\,/dV$ is usually computed fitting the characteristic curve.

The density can be computed from the same ion saturation current which,

under the conditions of $T_e \gg T_i$, corresponds to the Bohm ion current [16, 53]:

$$I_{\text{is}} = I_{\text{Bohm}} = 0.61\ en\sqrt{\frac{T_e}{m_i}}A_{\text{probe}} \quad , \tag{6.2}$$

again with the temperature expressed in Joule.

emissive Probe Even if an indirect measure of the electric potential of the plasma can be carried out from the characteristic curve of the Langmuir probe, this analysis is rather difficult and a potential source of error [53, 67]. A solution comes from the emissive probes. This probes have an electrically heated tip which emits low-energy electrons through thermoionic effect. Ideally speaking, when the probe voltage is set to be lower than the plasma potential, the electrons are repelled from the probe and the sensed probe current decreases. If the probe is biased to an higher voltage than the plasma potential, the electrons would be attracted back by the probe tip and the current would be the same of a conventional Langmuir probe [36] .

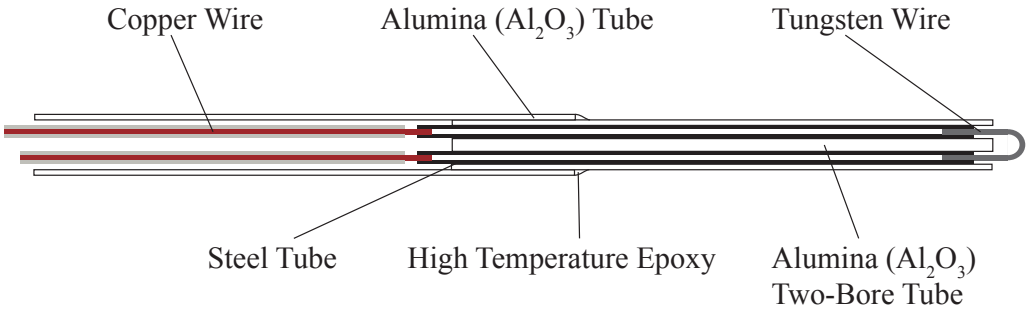

Figure 6.4: *Schematics of emissive probe. The heating circuit is not represented. No chip inductors are used because they could not handle the current of the heating circuit.*

Therefore, by looking at the difference between the characteristic curves in heated and non-heated cases, the plasma potential can be estimated. In particular, the *separation point method* consists in identifying the voltage at which the characteristic curves of the heated probe and the non-heated probe separates [67].

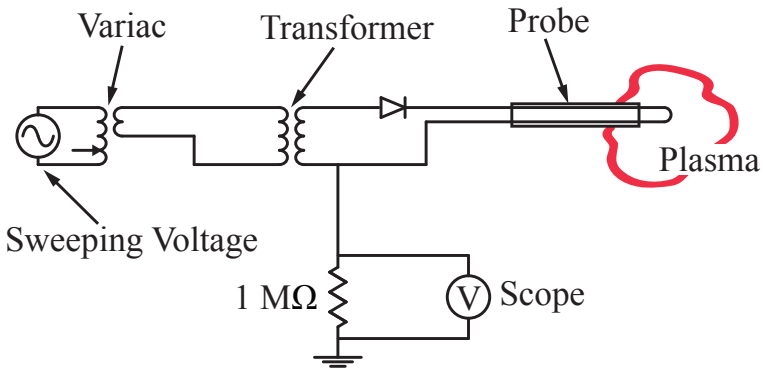

Figure 6.5: *Emissive probe circuit.*

Mach Probe and Single-Sided Langmuir Probe A Mach probe is a sensor used for measuring the plasma current and the ion drift Mach number. This probe is made of two sensing surfaces, one upstream and one downstream of the flow, with an insulating shield between the two. Alternatively, we can shield one side of a Langmuir probe (hence getting a single-sided probe) and rotate it to face different directions. In this case, upstream and downstream measurements cannot be taken simultaneously.

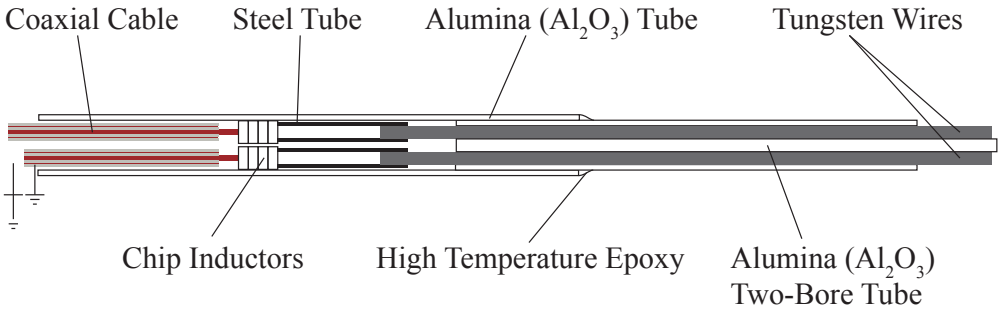

Figure 6.6: *Schematics of the Mach probe.*

When the probe is biased at the plasma potential, the two sides collect a certain amount of current, and the difference of these two collected currents gives the net current flowing in the plasma in the direction of the connecting line between the collecting surfaces[11].

$$J = J_U - J_D \quad , \tag{6.3}$$

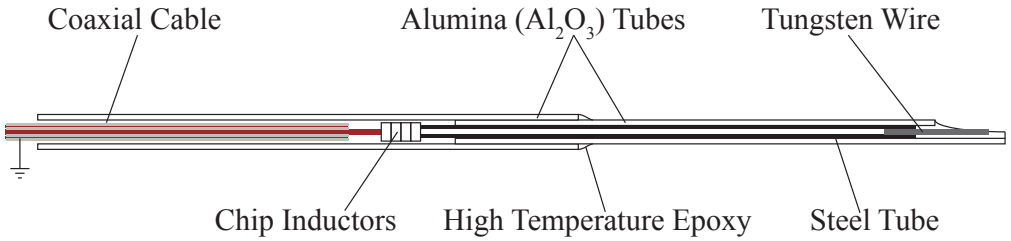

Figure 6.7: *Schematics of the Single-Sided Langmuir probe.*

where the current densities are computed simply from

$$J_{\mathrm{U,D}} = I_{\mathrm{U,D}} / A_{\mathrm{U,D}} \quad . \tag{6.4}$$

It is clear how an uncertainty on the collecting area due to manufacture imperfections directly leads to uncertainties in the computation of the currents. Thus, given the area uncertainty ΔA , the minimum measurable plasma current $I_p = \Delta I$ will be

$$\frac{\Delta I}{I} = \frac{\Delta A}{A} \quad . \tag{6.5}$$

We see here the advantage of using a rotating single-sided Langmuir probe, where the collecting area is always the same and comparative measurements are easier. Even we did not use the Mach probe for flow velocity measurements, one could compute the flow Mach number through the ratio of the ion saturation currents of the two surfaces [57]. For supersonic flows, we have

$$\frac{J_U}{J_D} = \exp(kM) \quad , \tag{6.6}$$

where J_U is the current density collected by the upstream surface, J_D is the current density collected by the downstream surface and k is a calibration constant. The quantitative value of this parameter k depends on the physical model that most accurately describes the sheath in the specific plasma under investigation. For the case of unmagnetized ions, $k \approx 1.34$ [35]. The plasma density and potential can be estimated from the characteristic curve of this probe by comparative analysis of the values obtained by the two sides [57].

As described and differently from Langmuir and emissive probes, Mach probes measurements are not only local, but also directional. The sensed

value of current and flow velocity is indeed related to the direction of the straight line connecting the two surfaces. Therefore, if a multi-directional measure were needed to determine the current and velocity vectors, we would need to rotate the probe about its axis.

Combined Mach-emissive Probe As previously described, the plasma current and potential can be directly measured by the use of Mach and emissive probes, respectively. Since it is desirable to get both measures in the same condition, we designed and manufactured a combined Mach and emissive probe of fig. 6.8 and 6.9.

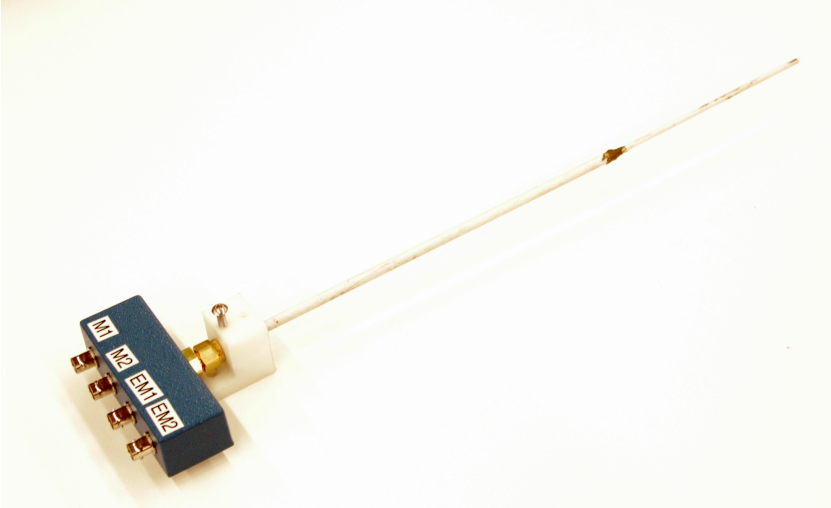

Figure 6.8: *Combined Mach-emissive probe.*

6.4 Experimental Setup

The experiment implements a solid molybdenum cathode and an annular copper anode. After several design iterations, we chose molybdenum for for the high temperature and sputtering resistance and for the relatively easiness in machining. Other materials, such as stainless steel or copper, suffered extremely high damage due to sputtering and thermal loads. The plasma density in the external region showed less aggressiveness, thus copper can be used as anode, helping to reduce the electrode losses. The relevant dimensions of the experimental setup are reported in fig. 6.10.

Figure 6.9: *Combined Mach-emissive probe tip. The Mach probe is made of the two tungsten wires in the upper and lower sides, while the thin tungsten arch is the sensing surface of the emissive probe.*

A stainless steel 6.35 mm (1/4 inch) feed line replaces the non conducting tube of the original magnetic nozzle experiment. Two sets of four 2.25 mm holes in the central tube provide the argon feed. The voltage is applied grounding the steel feeding tube and biasing external electrode through connection across the pyrex cylinder.

With respect to the original configuration of the magnetic nozzle experiment, the metallic feedline shields the argon from the electromagnetic waves coming from the antenna, preventing the ionization to occur before the actual feed, which may lead to a reduction in plasma source efficiency.

The external electrode presents a longitudinally-directed cut, in order to avoid induced currents to flow in the azimuthal direction due to RF coupling.

6.5 Operations

6.5.1 Operations Description

The overall data collection took about 50 hours of discontinuous run of the experiment. Sputtering and thermal loads on the feedline represented major

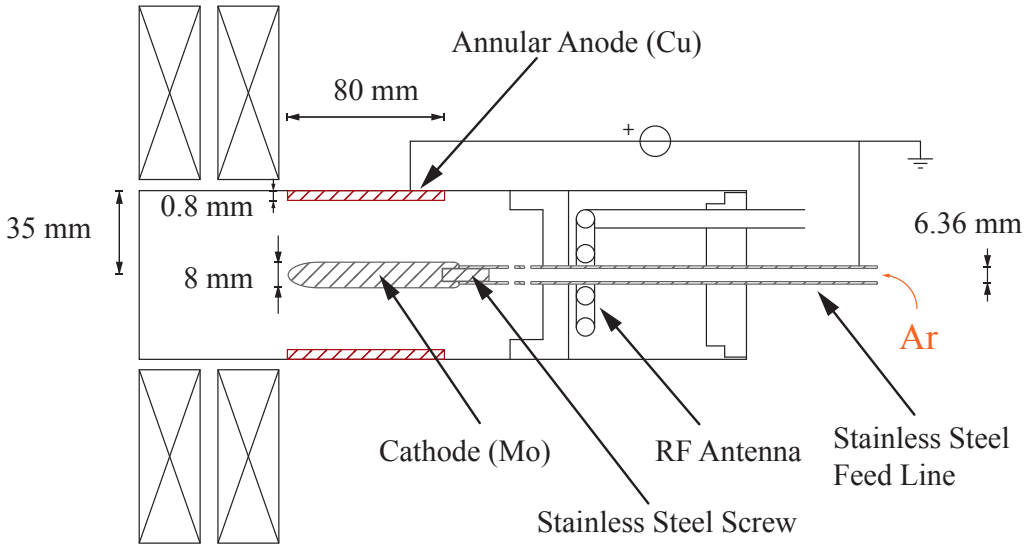

Figure 6.10: *Schematics with materials and relevand dimensions of the experimental setup.*

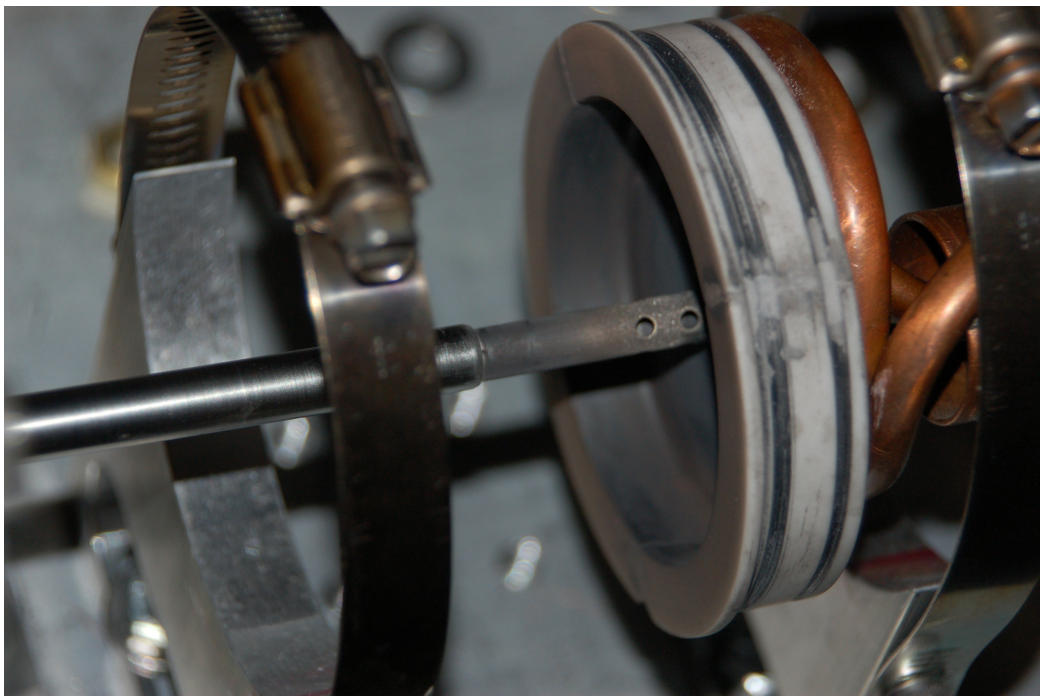

Figure 6.11: *Feedline and cathode installed for operation. The two series of feeding holes are visible as well as the Macor backplate and the copper antenna. To limit the sputtering due to electric field peaks, all edges have been smoothed.*

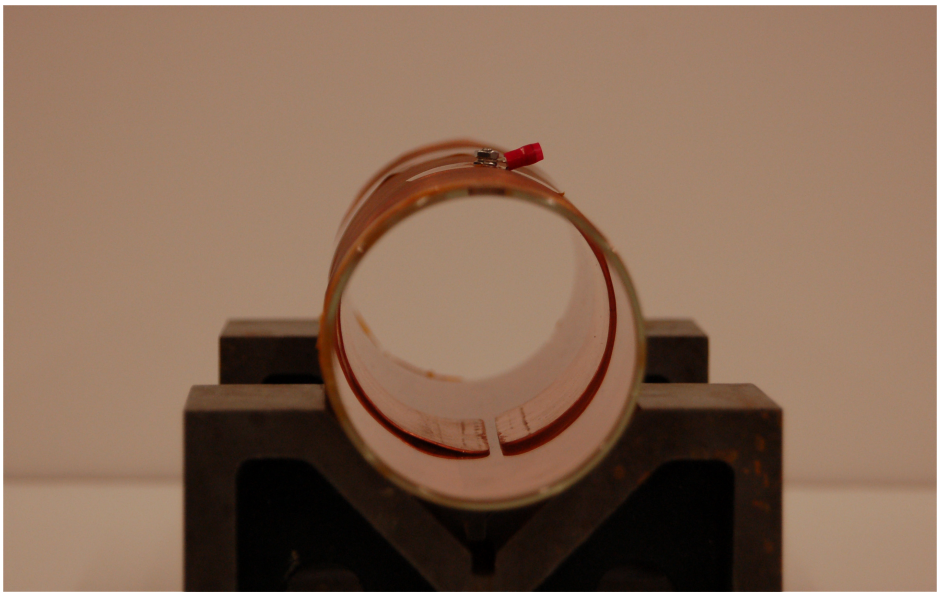

Figure 6.12: *Pyrex cylinder and external electrode before the installation. Note the cut in the cylinder that prevents RF-induced azimuthal current in the electrode. The edges have been rounded to avoid electric field peaks.*

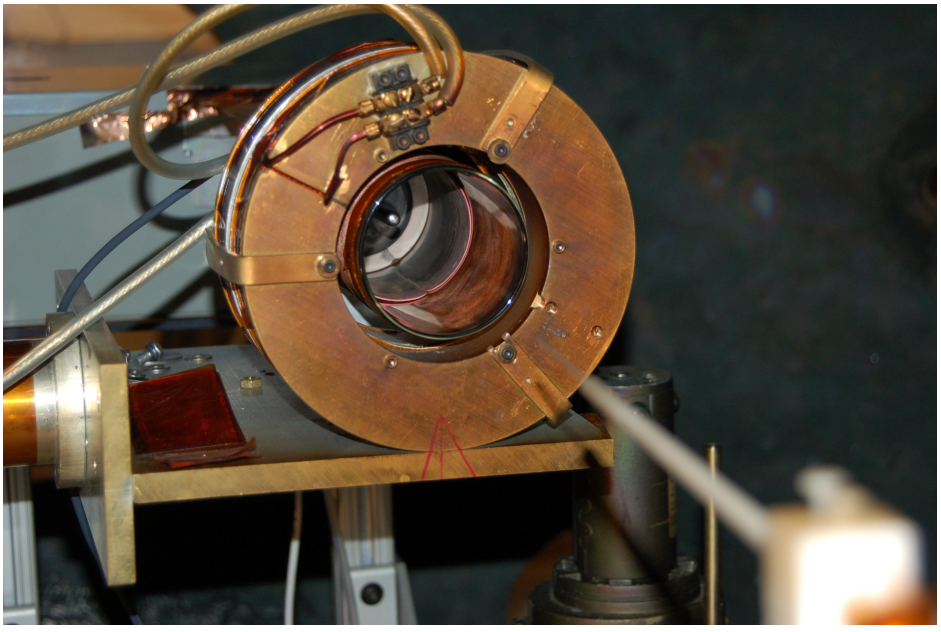

Figure 6.13: *Close-up view of the assembled setup with the two electrodes clearly visible inside the borosilicate tube. The Langmuir probe for plume measurements is also visible out of focus in the lower-right corner.*

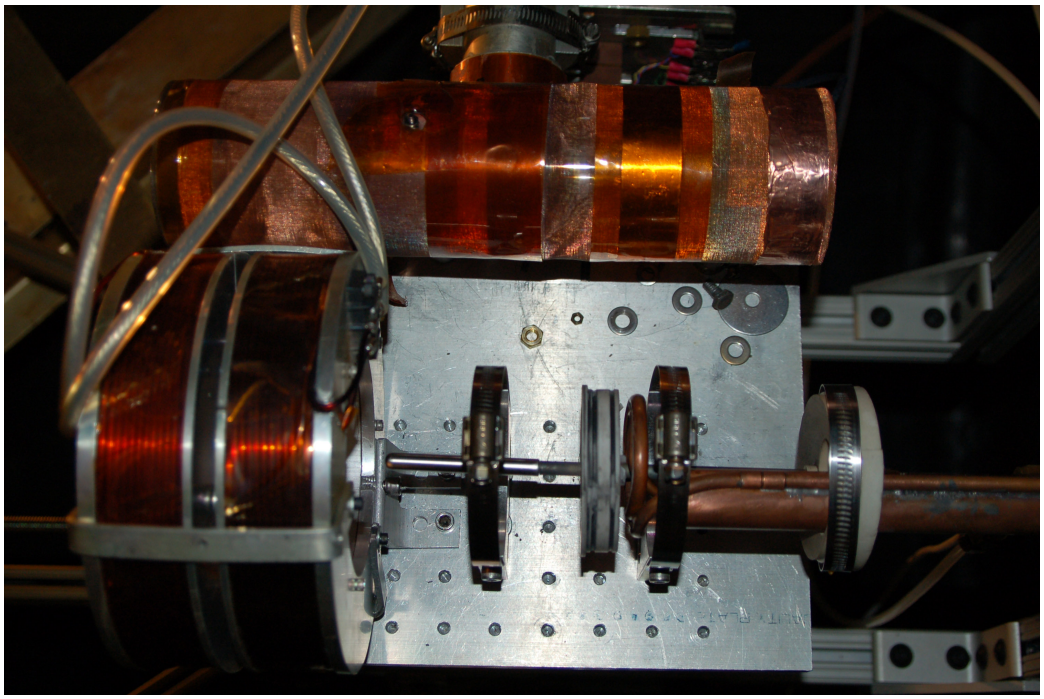

Figure 6.14: *View of the setup with the pyrex tube removed to show the internal disposition of the components. From left to right we see the two magnetic nozzle coils, the cathode, the feedline, the Macor backplate, the antenna and the Teflon backplate. The retention rings for the glass tube are also visible across the cathode and immediately behind the antenna.*

issues for both the feedline itself and the diagnostic used inside the plasma source. During all the operations, the argon mass flow rate was set to 2 mg/s and the base pressure was 5×10^{-5} Torr, with pressure never exceeding 1×10^{-4} Torr during the operations.

As first step of the experimental analysis, we measured the current-voltage characteristic curves of the electrodes system at different values of magnetic field, with a fixed RF power of 500 W. The resulting trends are reported in section 6.6.1.

To characterize the effect of the electrodes on the plasma flow, two series of measurements were taken, one inside the focusing stage and one in the plume outside the thruster. For these measurements, the chosen values of magnetic field were 120 G, 200 G and 280 G. The helicon antenna delivered power was set to 500 W for 120 G and 200 G, while an higher value of 600

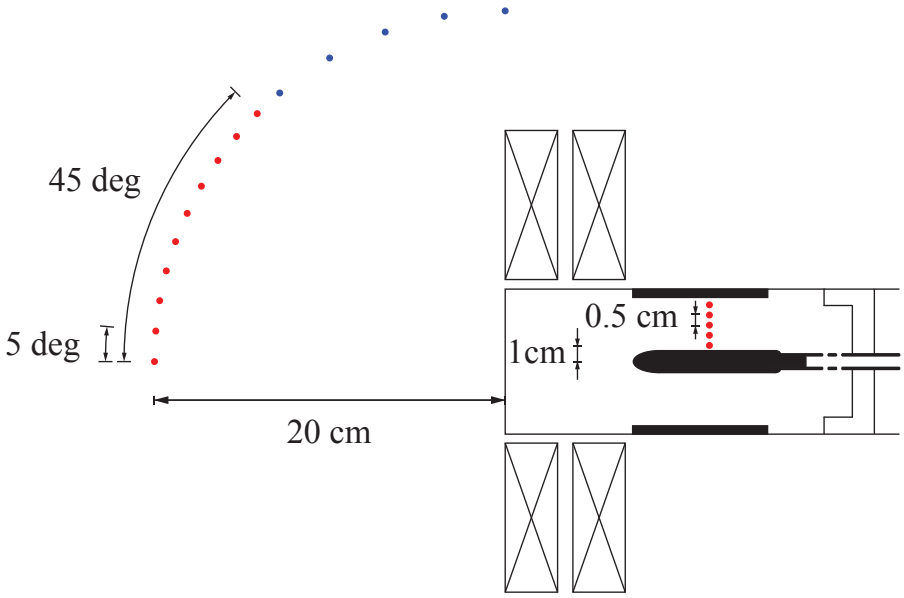

Figure 6.15: *Measurement points depiction. Measurements in the external plume beyond 45 degrees (marked as blue dots) showed very low density and negligible angular variation in the measured quantities, thus have been omitted for clarity from the results reported below.*

W was chosen to be delivered in the 280 G case for preventing instabilities and mode transitions observed at lower power.

The measurements inside the plasma source were taken at four different voltages, either 2 or 7 V, 15 V, 25 V and 35 V; those in the plume were taken at either 2 or 7 V, 20 V and 35 V. The first of these voltages (either 2 or 7 V) was set to be close to the zero-current value identified in section 6.6.1.

For the plasma source characterization we used the combined Mach-emissive probe and the single-sided Langmuir probe, moved radially between the cathode and the anode, with the sensing surfaces directed azimuthally. The positioning system had a resolution of ± 0.1 cm and the measurements were taken every 0.5 cm from radial coordinate equal to 1 cm (2 mm from the cathode) to 3 cm (4 mm from the anode).

The measurements in the external plume were taken using a Langmuir probe fitted onto a movable stand. The probe was set to a distance of 20 cm from the nozzle throat and was moved angularly up to 45 degrees, on one

side and with steps every 5 degrees, thus approximately following a ζ-surface. The movable stand had an angular resolution of ± 0.2 degrees.

A depiction of the measurement points inside the focusing stage and in the external plume is reported as fig. 6.15.

6.5.2 Operative Issues

Plasma Source and Electrodes

After about 40 hours of discontinuous operation, the plasma source stopped working. We found that the source backplate has been completely coated by sputtered steel from the feedline, effectively shielding the plasma source from the antenna radiation. Also, the Macor cracked along three different lines, most likely due to thermal stress. After extensive cleaning and having repaired the cracks, the backplate had been reinstalled and the plasma source restarted operating nominally. After this event, we limited the duration of each run to one hour.

Even if the feedline clearly suffered the extensive contact with the plasma, no significant damage were reported. In particular, the molybdenum cathode showed extreme resistance to the working conditions.

Figure 6.16: *Plasma source backplate before (left) and after (center) about 40 hours of discontinuous plasma operation. The backplate is coated by sputtered steel and some cracks appeared due to thermal stress. On the right, the cleaned and repaired backplate is ready for another set of runs.*

Diagnostic

The same sputtering and deposition phenomena strongly affected the diagnostic used for the characterization of the plasma between the electrodes.

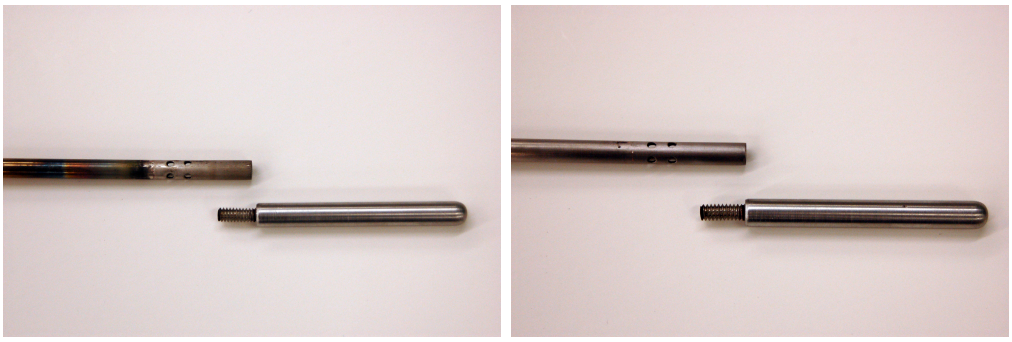

Figure 6.17: *On the left, feedline and cathode after about 40 hours of discontinuous plasma operation. Thermal and sputtering effects are clear on the feedline. On the right, the same components cleaned and readied for operation.*

In addition, the high density recorded in such a region led to probe saturation issues.

The combined Mach-emissive probe showed strong coupling between the Mach and the emissive circuits, and the measurements were considered not reliable. Thus, the whole plasma source characterization has been carried out using the single-sided Langmuir probe. The two-sided Langmuir probe used for the plume characterization behaved well and no significant steel deposition was observed.

6.6 Results and Discussion

6.6.1 Current-Voltage Characteristic Curve

When a voltage was applied between the electrodes, we observed a net current flowing from the DC power supply. Measuring such a current by using the voltage drop across a calibrated resistor, we drew the current-voltage characteristic curve of the electrodes circuit reported in fig. 6.18.

After an initially linear dependence on the voltage, the current approaches asymptotically a limiting value which depends on the applied magnetic field. We also see that such transition is sharper for higher values of magnetization. Furthermore, we found a finite voltage for zero-current condition, whose value depends on the applied magnetic field.

We can explain these trends as follows. At 0 G (no magnetic field) and

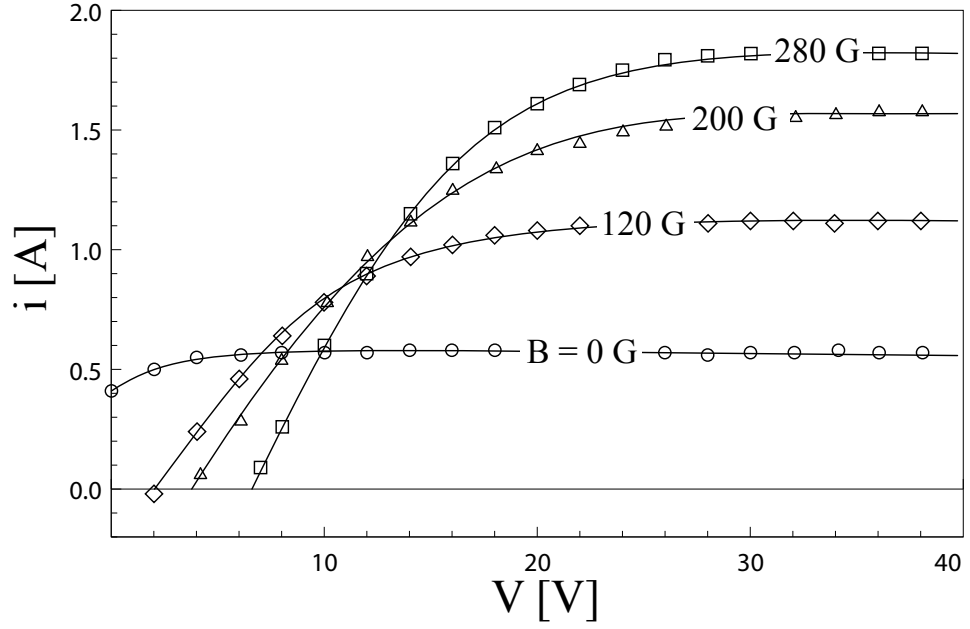

Figure 6.18: *Current-Voltage characteristic curves of the electrodes circuit, at different magnetic field. The source power is always set to 500 W, Argon mass flow rate 2 mg/s.*

at 0 V (the electrodes are shorted), both the electrodes are collecting a small electron current since their floating potential is below 0 V. Thus, since the density is approximately constant in the radial direction and the anode area is larger than that of the cathode, a net current flows from the anode to the cathode, in a positive direction according to our convention. When we apply a voltage, the cathode is kept a 0 V (is grounded) while the anode collects more and more electrons, up to the electron saturation current, increasing and then flattening the current-voltage trend. When we increase the magnetization, the floating potential of both the electrodes increases to positive values, but this raise is stronger at the anode. Thus, at 0 V the anode collects more and more ions as the magnetic field increases, eventually overcoming those taken by the cathode and leading to a net negative current. For restoring a zero-current condition, a voltage has to be applied to repel ions from the anode (i.e. moving the anode potential closer to the floating potential). The higher saturation current seen at higher magnetizations is probably due to an increased mobility of electrons along the magnetic field

lines that, at the level of the focusing stage, connect the two electrodes.

6.6.2 Focusing Stage Characterization

The characterization of the plasma inside the focusing stage aimed to draw the radial profiles of density, potential and azimuthal current in steady state at various values of applied voltages. During preliminary runs, we estimated the temperature to be 5.8 eV for all the operative conditions, compatibly to previous measurements on the original configuration of the experiment [48]. The error on the temperature measurement has been estimated as 25 % [48].

The radial density profiles at different values of magnetic field and applied voltage to the electrodes are reported in fig. 6.19, 6.21 and 6.23, while the radial potential distributions are reported in fig. 6.20, 6.22 and 6.24.

From the radial density profiles we see that an increased voltage across the electrodes pinches the plasma in all cases. We also see that, when no voltage is applied, the density peaks away from the longitudinal axis, differently from what observed in the original magnetic nozzle experiment of EPPDyL [48]. This is due to the perturbing effect of the cathode, which prevents the plasma to concentrate in the innermost region. However, this annular distribution is not found in the external plume, suggesting that a cross-field diffusion occurs between the focusing stage edge and the nozzle throat to redistribute the density profile.

The plasma potential, estimated from the floating potential corrected by the electron temperature, shows a roughly linear trend in the radial direction, with generally higher drops in the innermost regions, as expected from the geometry of the electrons (see discussion in section 5.4.2). The distribution of the plasma potential suggests that an inward-directed electric field is induced in the plasma, as desired. Also, as expected from the sheath theory, we see that the plasma bulk is always at higher potential than the walls and we note the strong shielding effect of the sheaths. Indeed, even if the cathode is always grounded (0 V), the innermost potential is always much higher. Thus, most of the applied voltage is actually lost nearby the cathode and does not penetrate the plasma bulk. Also, we find a potential drop nearby the anode, which we think to be related to the anode boundary layer and pre-sheath [22].

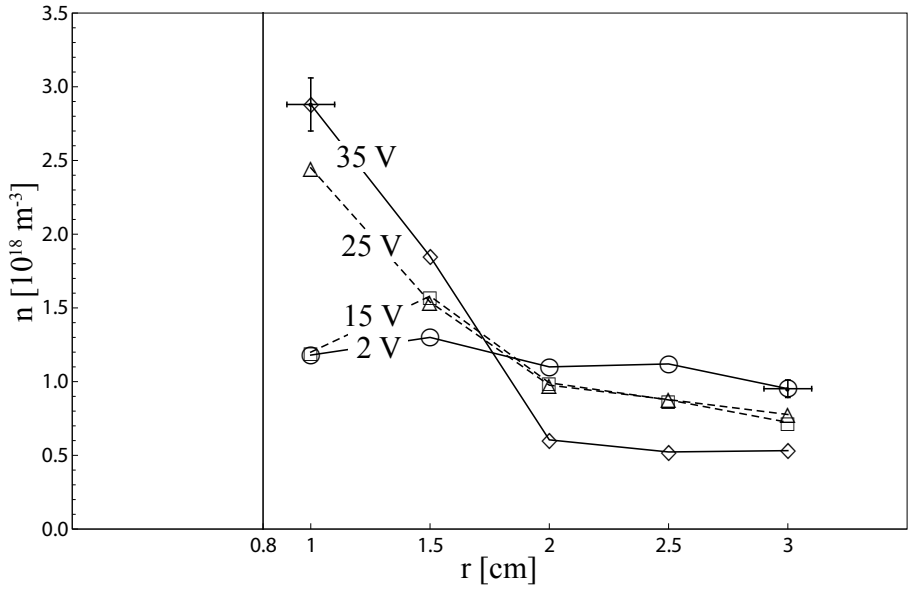

Figure 6.19: *Radial distribution of plasma density between the electrodes of the focusing stage. Applied magnetic field 120 G. The vertical black line marks the border of the cathode. For readability, only two error bars are reported.*

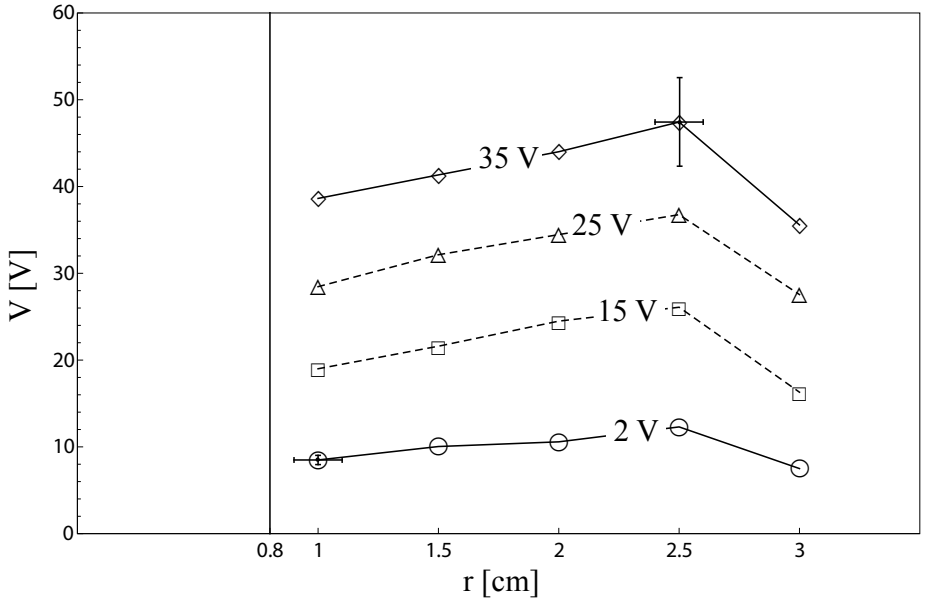

Figure 6.20: *Radial distribution of plasma potential between the electrodes of the focusing stage. Applied magnetic field 120 G.*

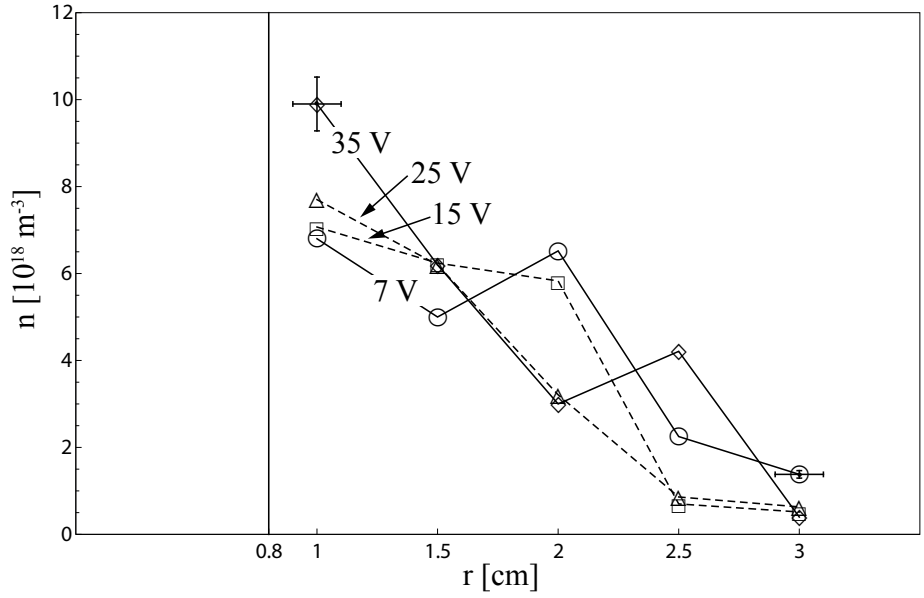

Figure 6.21: *Radial distribution of plasma density between the electrodes of the focusing stage. Applied magnetic field 200 G.*

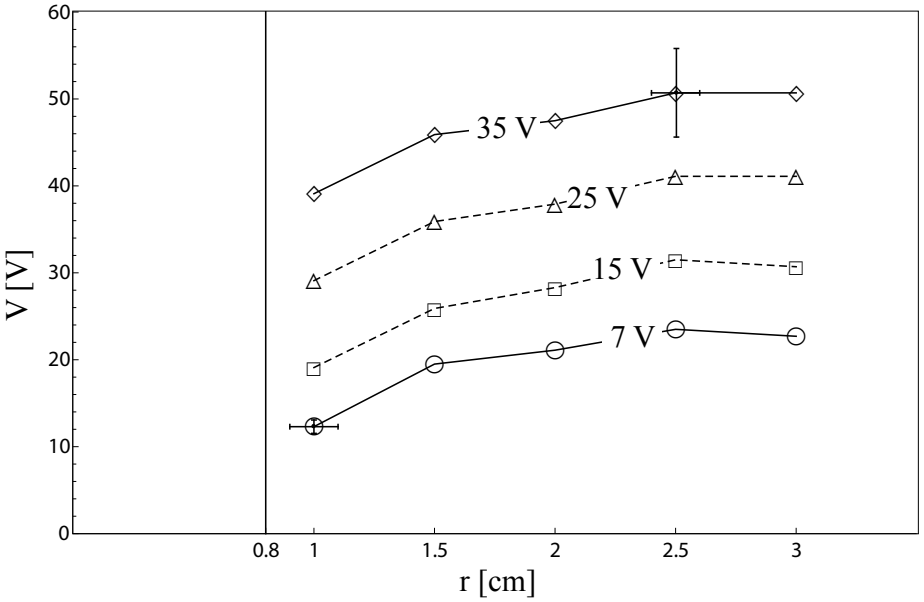

Figure 6.22: *Radial distribution of plasma potential between the electrodes of the focusing stage. Applied magnetic field 200 G.*

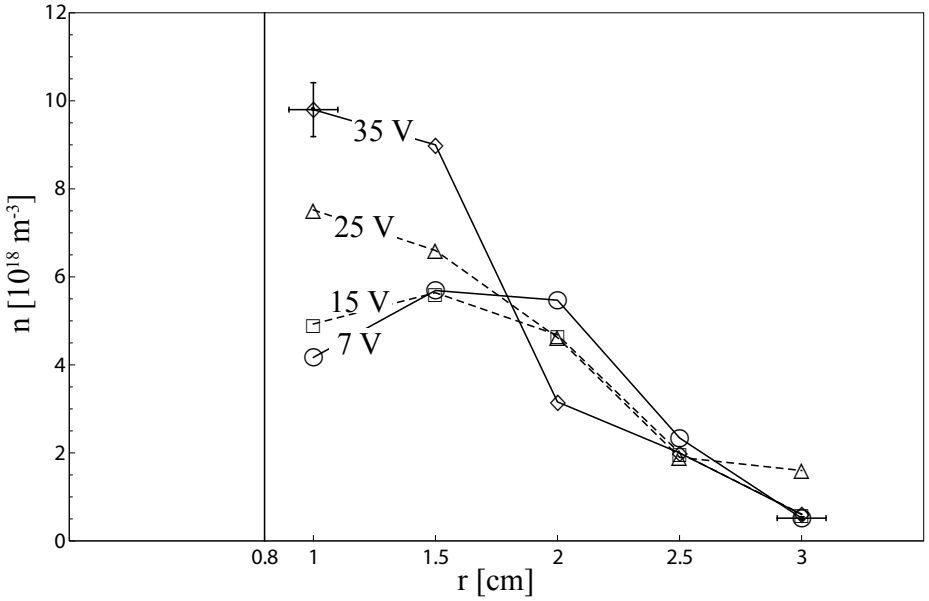

Figure 6.23: *Radial distribution of plasma density between the electrodes of the focusing stage. Applied magnetic field 280 G.*

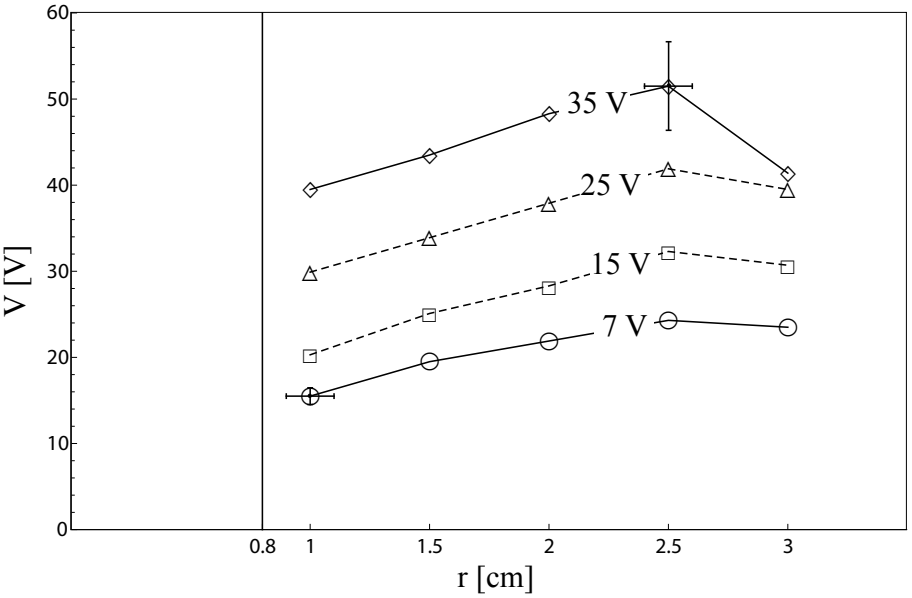

Figure 6.24: *Radial distribution of plasma potential between the electrodes of the focusing stage. Applied magnetic field 280 G.*

The Langmuir traces around and above the plasma potential showed poor repeatability and saturations phenomena, probably due to steel deposition and high plasma density. Thus, it was impossible to directly measure the profiles of the azimuthal current. However, we did see that increasing the applied voltage had an effect on the electron saturation current compatible with the induction of a diamagnetic electron Hall current and the radial density and potential distributions seems to confirm this observation.

Armed with this observation, we can try to derive averaged values for the azimuthal current through the computation of the classical conductivity tensor $\underline{\underline{\sigma}}$. The ion and electron cyclotron frequency Ω, Hall parameter β_{H}, and the slip factor $s = \beta_{\mathrm{H,e}}\beta_{\mathrm{H,i}}$ at various magnetic fields are reported in tab. 6.2.

B [G]	Ω_e [1/s]	$\beta_{\mathrm{H,e}}$	Ω_i [1/s]	$\beta_{\mathrm{H,i}}$	s
120	$2.11 \cdot 10^9$	435.09	$2.89 \cdot 10^4$	0.006	2.61
200	$3.52 \cdot 10^9$	725.16	$4.82 \cdot 10^4$	0.010	7.18
280	$4.92 \cdot 10^9$	1015.20	$6.75 \cdot 10^4$	0.014	14.11

Table 6.2: *Ion and electron cyclotron frequency Ω, Hall parameter β_H, and the slip factor $s = \beta_{H,e}\beta_{H,i}$ at various values of magnetic field.*

Adopting the usual cylindrical coordinates and approximating the magnetic field as parallel to the z axis, the resulting conductivity tensor can be written as of eq.(6.7)

$$\underline{\underline{\sigma}} = \begin{bmatrix} \sigma_\perp & \sigma_H & 0 \\ -\sigma_H & \sigma_\perp & 0 \\ 0 & 0 & \sigma \end{bmatrix} \quad , \tag{6.7}$$

where the parallel conductivity σ is equal to $1.7391 \cdot 10^4$ $1/\Omega m$. For each value of magnetic field, we can compute the other two terms of the conductivity tensor, $\sigma_\perp$ and σ_H. The results are reported in tab. 6.3

As clear from the last column of tab.6.3, the Hall current dominates the radial current when a radial electric field is applied to the plasma. However, keeping constant such a radial electric field, the higher the magnetic field and the lower is the Hall conductivity, since also the ions start showing a significant $\mathbf{E} \times \mathbf{B}$ drift.

B [G]	$\sigma_\perp/\sigma$	σ_H/σ	$\sigma_H/\sigma_\perp$
120	$1.907 \cdot 10^{-5}$	0.0023	120.6
200	$1.555 \cdot 10^{-5}$	0.0014	90.0
280	$1.466 \cdot 10^{-5}$	0.0010	66.85

Table 6.3: *Perpendicular and Hall conductivities in the plasma at different magnetic fields.*

Now, from a linear fit of the plasma potential profiles we can estimate a radially-averaged value for the radial electric field, which eventually will allow us to compute the average value of the azimuthal current as

$$J_\theta = -\sigma_H E_r \quad . \tag{6.8}$$

The resulting averaged electric field and azimuthal currents are reported in tab. 6.4 and 6.5.

E_r [V/m]	B = 120 G	B = 200 G	B = 280 G
$V = 2$ or $7V$	-239	-704	-576
$V = 15V$	-483	-792	-784
$V = 25V$	-544	-760	-800
$V = 35V$	-581	-728	-816

Table 6.4: *Averaged radial electric field at various values of magnetic field and applied voltages. The first row correspond to the electric field for zero-current applied voltage.*

J_θ [A/m^2]	B = 120 G	B = 200 G	B = 280 G
$V = 2$ or $7V$	9560	17141	9817
$V = 15V$	19328	19283	13362
$V = 25V$	21776	18504	13635
$V = 35V$	23256	17725	13907

Table 6.5: *Averaged azimuthal current at various values of magnetic field and applied voltages. The first row correspond to the azimuthal current for zero-current applied voltage.*

To depict the pinching effect of the azimuthal current we can plot in fig. 6.25 the ratio n_p/n_{p0} with respect to $J_\theta/J_{\theta 0}$, where n_p is the density

in the innermost position, n_{p0} is n_p for $J_\theta = J_\theta|_{\text{zero current}}$ and $J_{\theta 0}$ is the zero-current for B = 120 G.

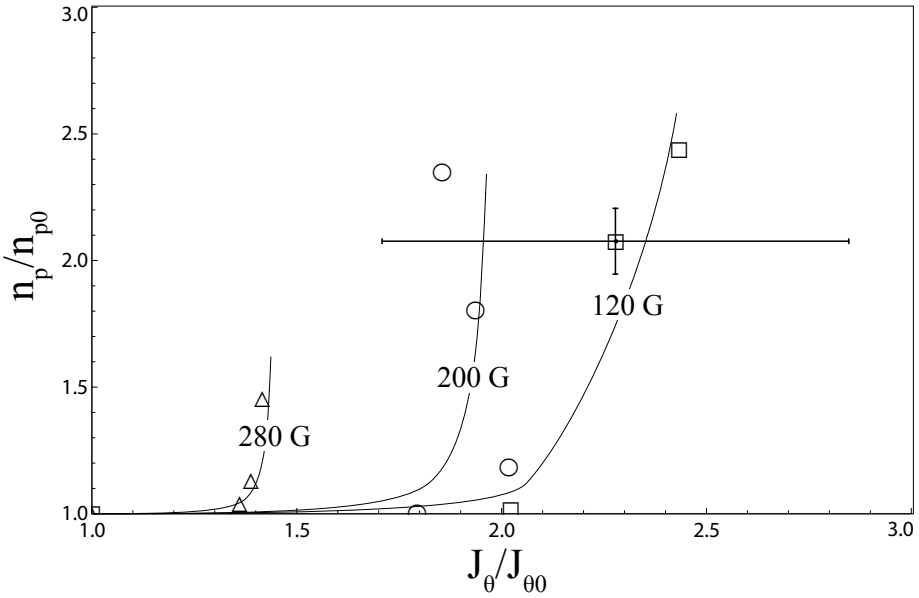

Figure 6.25: *Radial distribution of plasma potential between the electrodes of the focusing stage. Applied magnetic field 280 G.*

From fig. 6.25 we see that the normalized density peak value increases with the azimuthal current. Even if the errors on the currents are too big to allow a reliable fit of the data, we can say that the results of fig. 6.25 actually prove the effectiveness of the concept of current-driven focusing stage.

6.6.3 Plasma Plume Characterization

After having characterize the flow between the electrodes, we proceeded with the measurements in the external plume.

The angular density distribution at different values of magnetic fields and electrodes voltage has been computed using the temperature recorded along the nozzle axis and the results are reported in fig. 6.26, 6.28 and 6.30. The angular potential distributions are reported in fig. 6.27, 6.29 and 6.31.

In all cases, the electric potential across the plume is approximately constant, with a minimal drop in the external regions, as foreseen by the theory. Such a constant value increases with the applied voltage, as already seen

in the plasma source characterization. The fact that the plasma potential increases with the applied voltage even outside in the plume, far from the focusing stage, suggests that a perturbation of the nozzle throat characteristics does propagate along the plume.

From fig. 6.26, 6.28 and 6.30 we observe either the increase of the plasma density in the inner region and the faster decay in the external region, with general prevalence of the first effect over the second, as predicted in theory. The action of the focusing stage and can be clearly seen in fig. 6.32 as an increased brightness in the center of the plume and reduced divergence of the nozzle flow.

The density profiles of the 200 G and 280 G cases show the expected trends, with the 200 G case being more affected than the 280 G thanks to higher values of azimuthal current in the source, as depicted in fig. 6.25. We observe a particular behavior in the 120 G case: even if this case features the highest values of azimuthal current in the source, the plume is not as affected as we might have expected. We believe that the dampening of the collimating effect may be due to the very low magnetization and ionization reported in this situation, which may drive an enhanced cross-field transport.

As predicted, at higher value of magnetization the difference between applied voltage is weaker. Indeed, from fig. 6.30 we find that the difference between 20 V and 35 V is minimal at 280 G of applied field, while is significant for the case of 200 G. Moreover, we find that the already well focused condition found at 280 G is generally less affected by the focusing stage action than the less efficient flow at 200 G.

Finally, since the plasma potential is transversally constant, we note that the same qualitative trend of transversal density distribution should be found without distortion at the nozzle throat, thus matching the predicted profile of fig. 4.5.

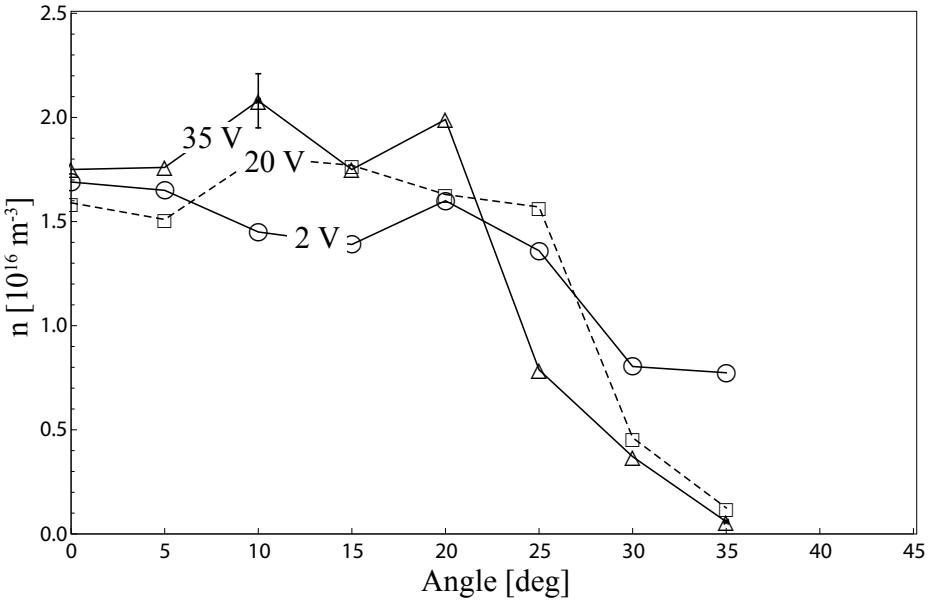

Figure 6.26: *Angular distribution of plasma density in the plume at 20 cm from the nozzle throat. Applied magnetic field 120 G. The measurements beyond 35 degrees from the axis were too noisy for a reliable density distribution estimation and have been omitted. For readability, only two error bars are reported.*

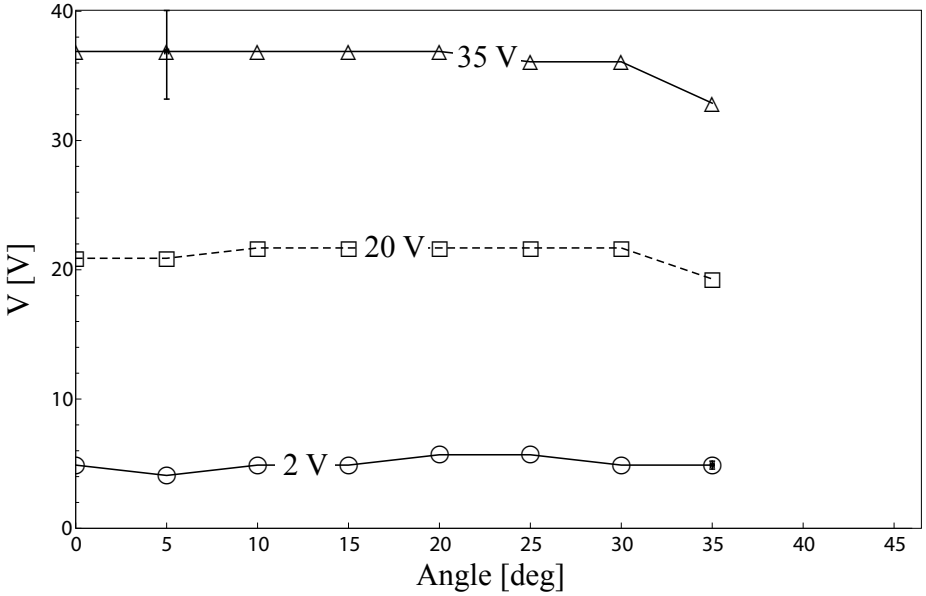

Figure 6.27: *Angular distribution of plasma potential in the plume at 20 cm from the nozzle throat. Applied magnetic field 120 G.*

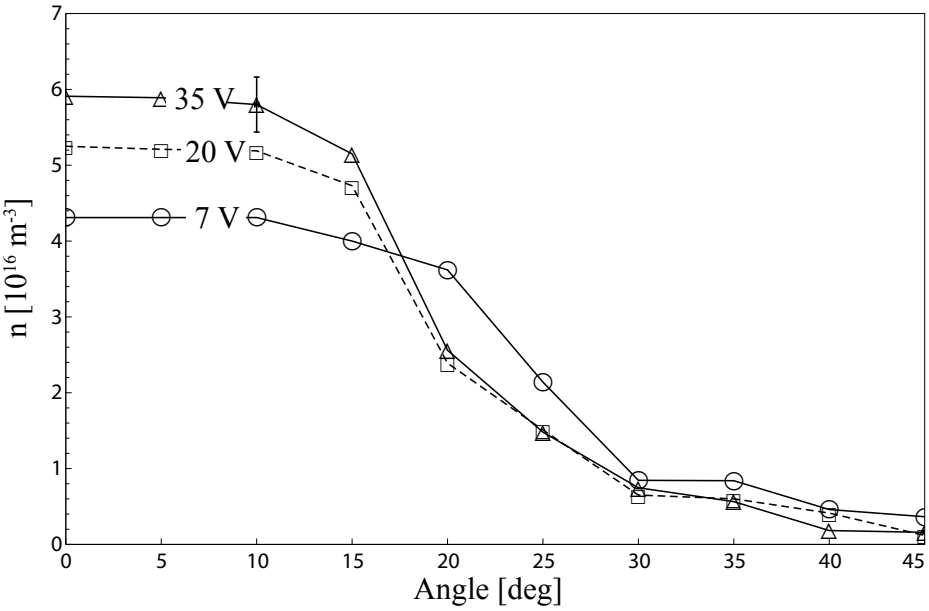

Figure 6.28: *Angular distribution of plasma density in the plume at 20 cm from the nozzle throat. Applied magnetic field 200 G.*

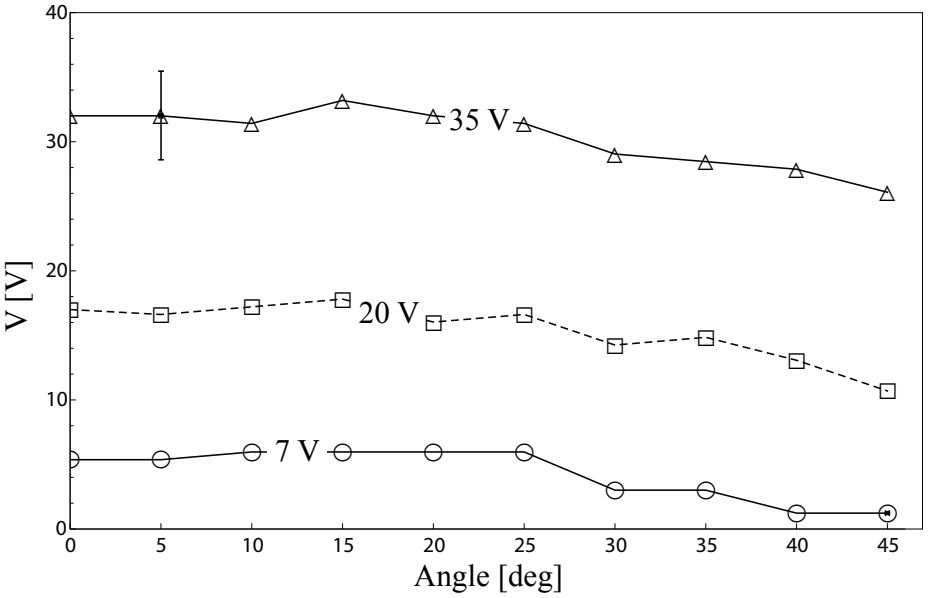

Figure 6.29: *Angular distribution of plasma potential in the plume at 20 cm from the nozzle throat. Applied magnetic field 200 G.*

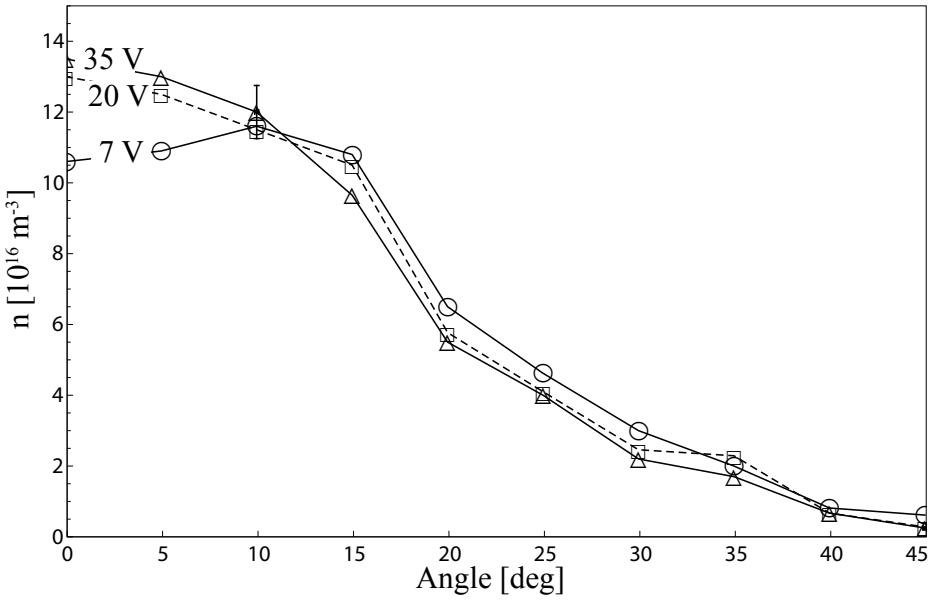

Figure 6.30: *Angular distribution of plasma density in the plume at 20 cm from the nozzle throat. Applied magnetic field 280 G.*

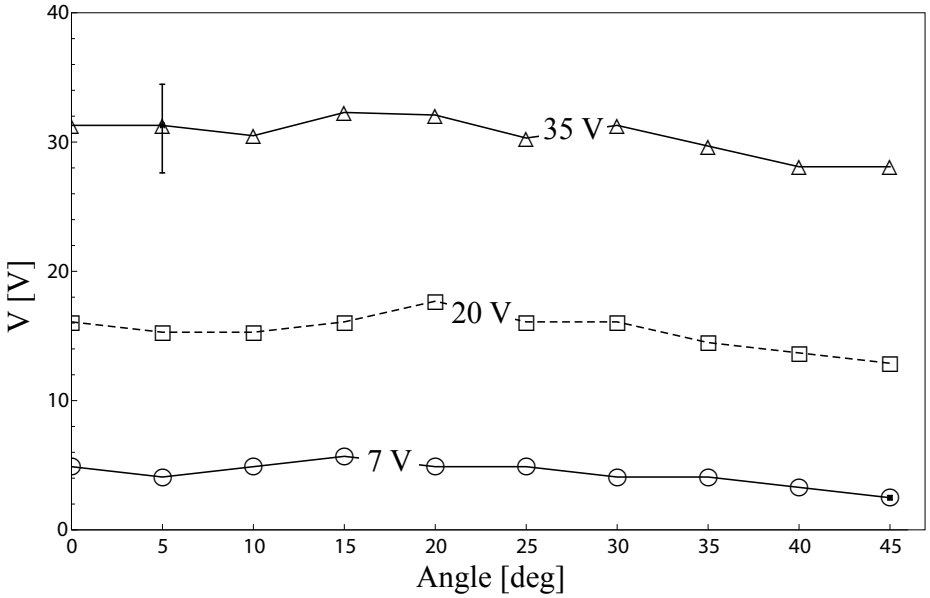

Figure 6.31: *Angular distribution of plasma potential in the plume at 20 cm from the nozzle throat. Applied magnetic field 280 G.*

Even if the electrodes architecture was expected to be much less efficient than the RMF architecture, we found such a significant focusing of the plume with a focusing stage power consumption always below the 10 % of the delivered power to the plasma source. We also point out that increasing the power of the plasma source by 10 % while turning off the focusing stage has very little effect on the plume. Thus, this experiment confirmed empirically the advantage of using a focusing stage over an heating stage, in the limits of operations here described.

Pictures in natural colors of the experiment operating in various conditions are reported in fig. 6.33, 6.34 and 6.35.

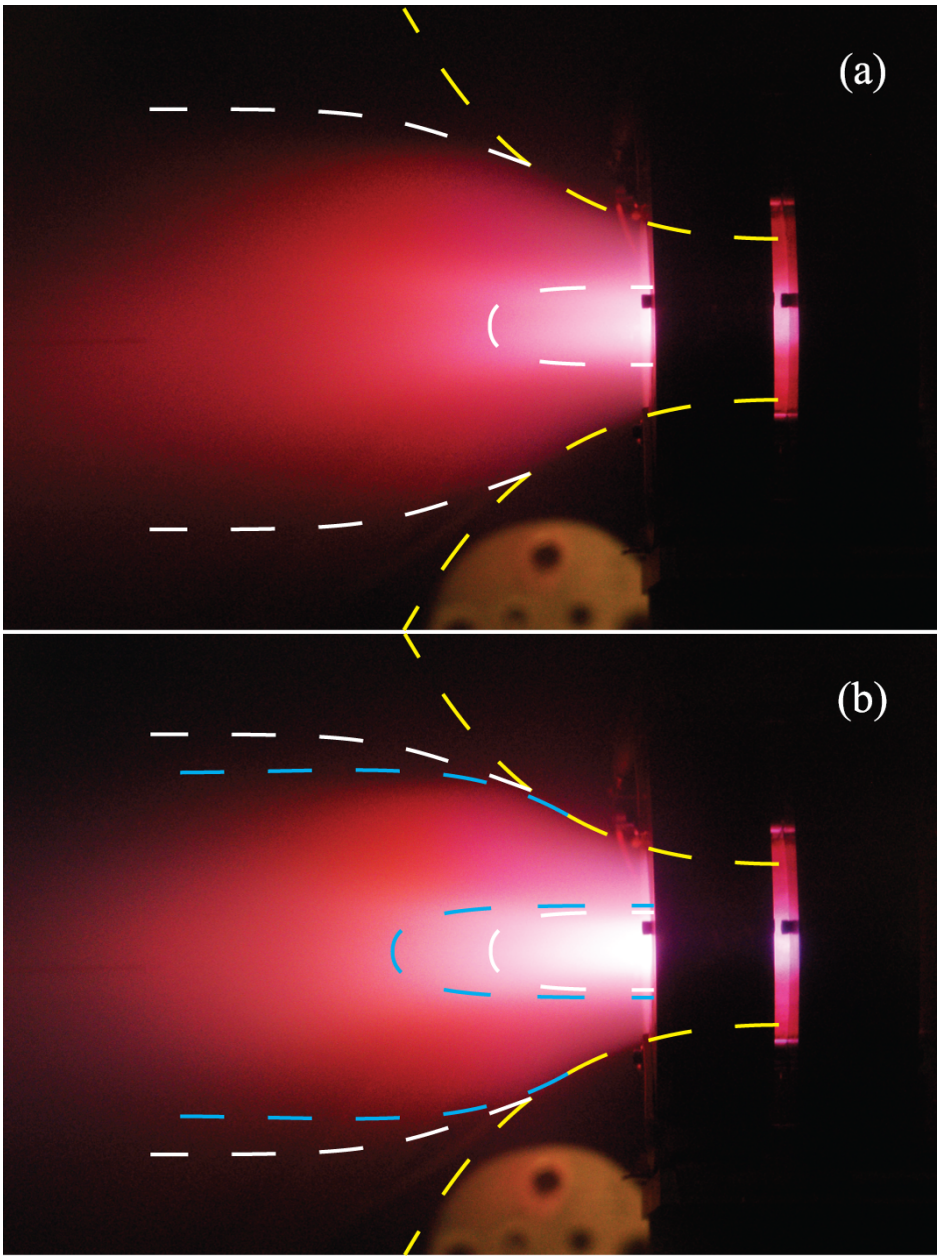

Figure 6.32: *Enhanced-contrast pictures of plasma fire with 280 G of applied magnetic field. Voltage between the electrodes set to 7 V for (a) and 20 V for (b). The increase in brightness of the plasma core and the reduced plume divergence are clearly visible. The dashed yellow lines are the magnetic streamline of the throat radius, the white dashed lines mark the plume boundaries and the core region at 7 V, while the blue lines of (b) mark the plume boundaries and the core region at 20 V.*

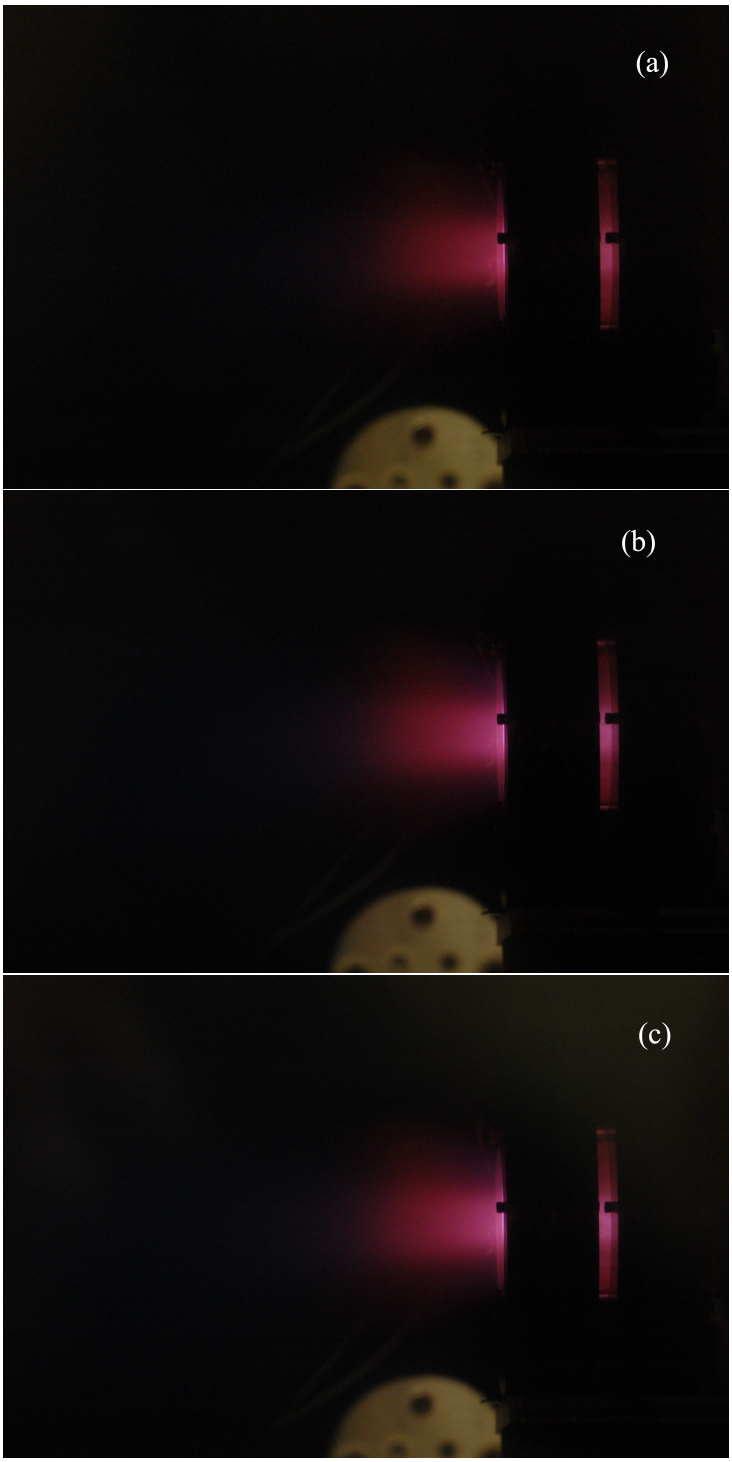

Figure 6.33: *Pictures in natural colors of plasma fire with 120 G of applied magnetic field. Voltage between the electrodes set to 2 V (a), 20 V (b) and 35 V (c). Camera settings: exposition 1/30 s, aperture f/7.1.*

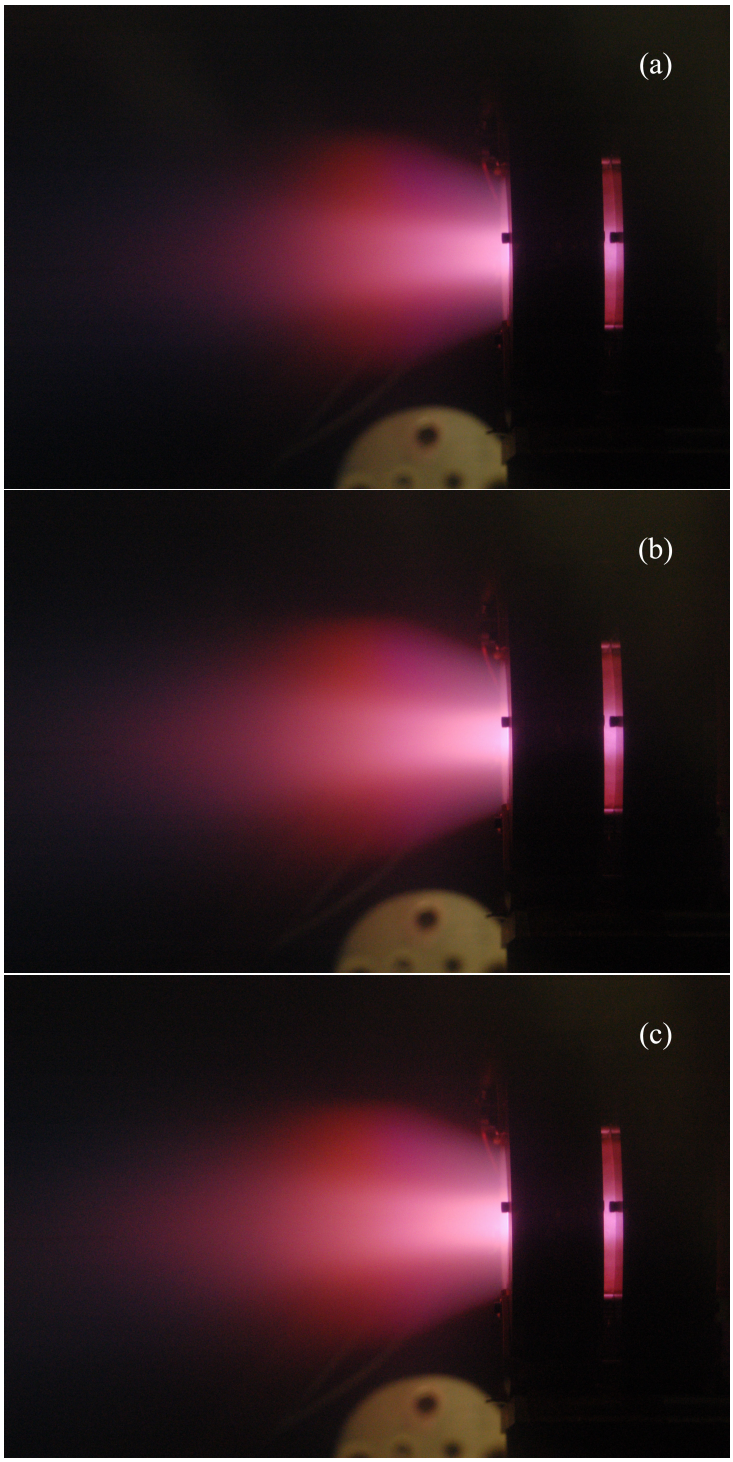

Figure 6.34: *Pictures in natural colors of plasma fire with 200 G of applied magnetic field. Voltage between the electrodes set to 7 V (a), 20 V (b) and 35 V (c). Camera settings: exposition 1/30 s, aperture f/7.1.*

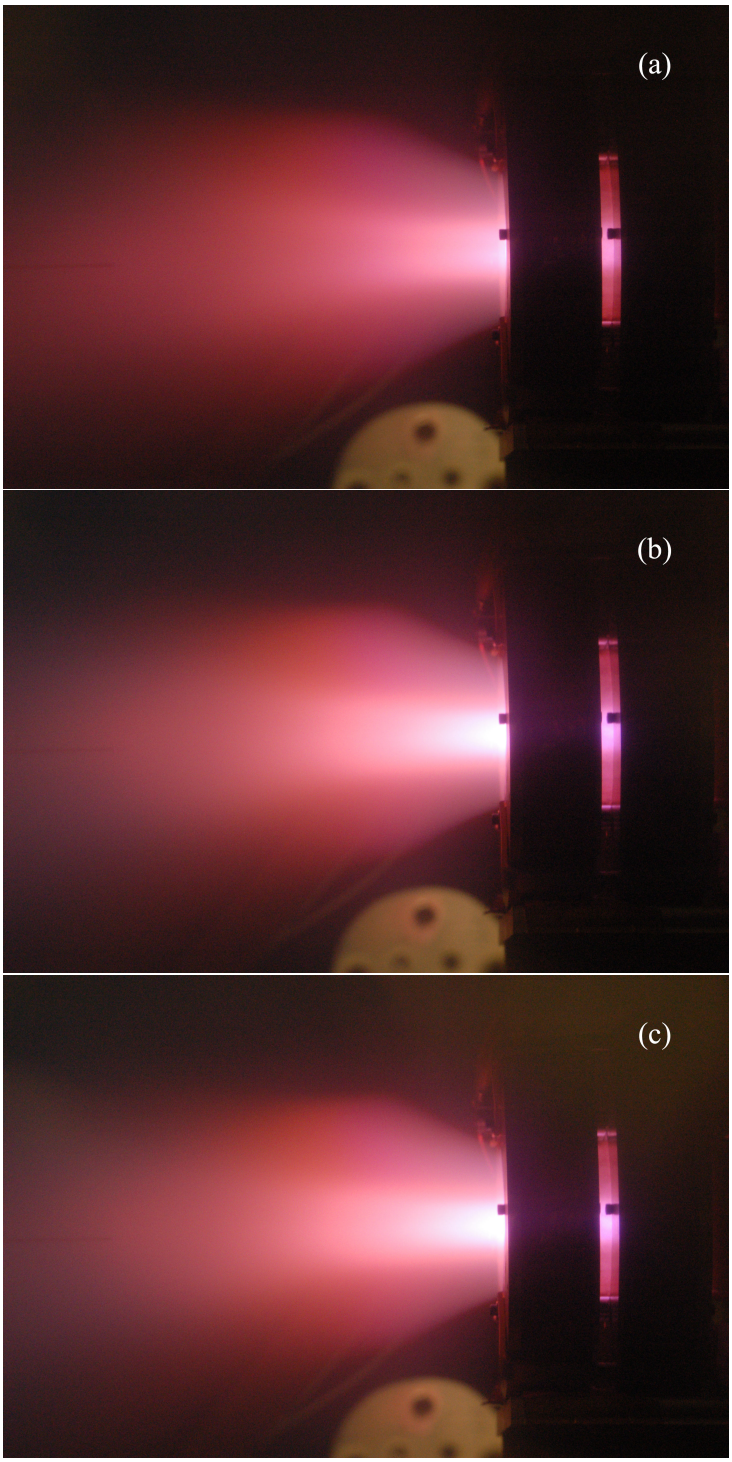

Figure 6.35: *Pictures in natural colors of plasma fire with 280 G of applied magnetic field. Voltage between the electrodes set to 7 V (a), 20 V (b) and 35 V (c). Camera settings: exposition 1/30 s, aperture f/7.1.*

6.7 Future Work and Design Improvements

As previously described, sputtering and thermal loads represented major issues during the operations of the experiments, with steel deposition on the diagnostic being the most severe problem for the focusing stage characterization. We believe that replacing steel with molybdenum in the feedline should strongly reduce these losses. In our case, budget constraints prevented the implementation of such a straightforward solution. A complementary option would be to redesign the feed system to avoid the concentration of erosion phenomena and thermal stresses on the cathode. Specifically, we are thinking to inject the argon from a set of holes in the backplate, or in the glass tube, in order to avoid ionization to occur close to the cathode. Once a more erosion-resistant feed system has been implemented, a full characterization of the azimuthal current density inside the focusing stage can be carried out.

Improvements in the diagnostic may include a thrust stand and a Retarding Potential Analyzer (RPA) for the investigation of the ion distribution function. A full bidimensional characterization of the nozzle plume and an investigation of the throat region are other areas we found to be worth of future experimental research.

Chapter 7

Conclusions

In this work we analyzed theoretically and experimentally the influence of an applied azimuthal electron current on the flow inside an electron-driven magnetic nozzle for thermal plasma acceleration. The discussion on the modified momentum equations and a quasi-one dimensional model allowed us to restrict our focus to the electronic population, also showing the need of a multi-dimensional description.

The theoretical framework developed led us to understand the nature of the interaction between the azimuthal current and the plasma flow. We found that such an interaction is mediated by the density distribution at the throat, which is in turn influenced by the applied azimuthal current. Thus, previously-used cold plasma approximations proved to be not comprehensive enough to describe the phenomenon. Then, the solution of the modified flow showed that the introduction of such a diamagnetic current leads to a better collimation of the plasma flow, eventually increasing the nozzle propulsive performances, especially in terms of thrust coefficient and specific impulse. Moreover, we showed that increasing the nozzle performances through jet collimation is more efficient than a direct increase of the power of the jet. Armed with these results, we proposed three different designs for systems to introduce the throat azimuthal current, exposing advantages and problematics of each of them.

Finally, to prove the concept of *focusing stage*, we designed and operated an experimental equipment that implemented the most simple of the presented architectures. Even if a complete investigation of the applied az-

imuthal current was not possible with the equipment in use, we did find clues that an azimuthal electron current is induced by the focusing stage. Measurements taken in the plasma flow inside the focusing stage and in the external plume showed that our system does collimate the jet even when fed with less than 10 % of the plasma source power.

In conclusion, supported by theoretical computations and experimental evidences, we believe that the concept of magnetic nozzle plasma focusing through induction of electron azimuthal current has the potential to be an efficient mean to increase significantly the performances of thermal plasma thruster.

From this thesis, two papers have been derived, corresponding to Chapters 4-5, and Chapter 6, respectively:

- *"Propulsive performance of finite-temperature plasma flow in a magnetic nozzle with applied azimuthal current"*, a full jurnal paper to be submitted for peer review to Physics of Plasmas and attached here as Appendix A.

- *"Experimental investigation of plasma plume characteristics in applied radial electric field magnetic nozzle"*, accepted for presentation at 50th AIAA/ ASME/SAE/ASEE Joint Propulsion Conference, 28 - 30 July 2014 Cleveland, Ohio, USA.

Acronyms, Symbols and Constants

Acronyms

EDMN	Electron-Driven Magnetic Nozzle
FRC	Field Reversed Configuration
FS	Focusing Stage
MHD	Magnetohydrodynamics
MN	Magnetic Nozzle
PIC	Particles In Cell
RF	Radio Frequency
RMF	Rotating Magnetic Field
RPA	Retarding Potential Analyzer
SWR	Standing Wave Ratio
VASIMR	Variable Specific Impulse Magnetoplasma Rocket

Symbols

$\mathbf{x}_{\mathrm{i,a}}$	Position vector of the i-th particle of a-th population
$\mathbf{v}_{\mathrm{i,a}}$	Velocity vector of the i-th particle of a-th population
m_a	Mass of particles of a-th population
q_a	Charge of particles of a-th population
n_a	Number density of the a-th population
f_a	Distribution function of the a-th population
C_a	Boltzmann's collisional term of a-th population

S_a	Continuity equation source term of a-th population
$\mathbf{u}_a$	Flow velocity of the a-th population
$\mathbf{R}_a$	Inter-population collisional term of a-th population
$\mathbf{\Pi}_a$	Viscous tensor of a-th population
P_a	Isotropic pressure of a-th population
T_a	Temperature of the a-th population
$\mathbf{Q}_a$	Thermal flux of a-th population
$\Omega_{\mathrm{c,a}}$	Cyclotron frequency of a-th population
$\rho_{\mathrm{L,a}}$	Larmor radius of a-th population
$\mathbf{u}$	Mass-averaged flow velocity
ρ_m	Mass density
$\mathbf{\Pi}$	Viscous tensor of mass-averaged flow
P	Isotropic pressure of mass-averaged flow
P_{mag}	Magnetic pressure
T	Temperature of mass-averaged flow
$\mathbf{Q}$	Thermal flux of mass-averaged flow
$\mathbf{E}$	Electric field
$\mathbf{B}$	Magnetic induction field
ϕ	Electrostatic potential
ψ	Magnetic stream-function
ζ	Magnetic scalar potential
e	Elementary charge
ρ	Charge density
$\mathbf{J}$	Conduction current density
λ_D	Debye length
$\underline{\underline{\eta}}$	Resistivity tensor
ν_{ab}	Collision frequency between species a and b
β	Thermal-to-magnetic pressures ratio
β_H	Hall parameter
$(\hat{\mathbf{b}}, \hat{\mathbf{n}}, \hat{\vartheta})$	Magnetic intrinsic tern
$(\hat{\mathbf{s}}, \hat{\mathbf{p}}, \hat{\vartheta})$	Flow intrinsic tern
$(\hat{\mathbf{r}}, \hat{\vartheta}, \hat{\mathbf{z}})$	Cylindrical coordinate tern

Physical Constants

ϵ_0	Vacuum dielectric permittivity
μ_0	Vacuum magnetic permeability
k_b	Boltzmann's constant

Bibliography

[1] E. Ahedo. Parametric analysis of a magnetized cylindrical plasma. *Physics of Plasmas*, 16:113503, 2009.

[2] E. Ahedo. Plasmas for space propulsion. *Plasma Phys. Control. Fusion*, 53:124037, 2012.

[3] E. Ahedo and M. Merino. Two-dimensional supersonic plasma acceleration in a magnetic nozzle. *Physics of Plasmas*, 17(073501), 2010.

[4] E. Ahedo and M. Merino. On plasma detachment in propulsive magnetic nozzles. *Physics of Plasmas*, 18(053504), 2011.

[5] E. Ahedo and M. Merino. Magnetic nozzle far-field simulation. In *Proceedings of the 48th AIAA/ASME/SAE/ASEE Joint Propulsion Conference*, Jul 2012.

[6] E. Ahedo and M. Merino. Two-dimensional plasma expansion in a magnetic nozzle: Separation due to electron inertia. *Physics of Plasmas*, 19(083501), 2012.

[7] E. Ahedo and M. Merino. Influence of electron and ion thermodynamics on the magnetic nozzle plasma expansion. In *Proceedings of 33rd International Electric Propulsion Conference*, October 2013.

[8] A. V. Arefiev and B. N. Breizman. Theoretical components of the vasimr plasma propulsion concept. *Physics of Plasmas*, 11:2942–2949, 2004.

[9] A. V. Arefiev and B. B. N. Magnetohydrodynamic scenario of plasma detachment in a magnetic nozzle. *Physics of Plasmas*, 12(043504), 2005.

[10] P. M. Bellan. Rotamak confinement-power-current relationships and r.f. loading resistance. *Plasma Physics and Controlled Fusion*, 31:879–894, 1989.

[11] E. A. Bering, M. C. Kelley, and F. S. Mozer. Theory and operation of the split langmuir probe. *Planetary and Space Science*, 21:1983–2001, 1973.

[12] B. N. Breizman and A. A. V. Radially localized helicon modes in nonuniform plasma. *Physical Review Letters*, 84(17):3863, 2000.

[13] R. L. Burton and P. J. Turchi. Pulsed plasma thruster. *Journal of Propulsion and Power*, 14:716–735, 1998.

[14] C. C., K. Takahashi, and R. W. Boswell. Axial force imparted by a conical radiofrequency magneto-plasma thruster. *Applied Physics Letters*, 100:113504, 2012.

[15] P. Chabert and N. Braithwaite. *Physics of Radio-Frequency plasmas*. Cambridge University Press, Cambridge, UK, 2011.

[16] F. F. Chen. *Plasma Physics and Controlled Fusion, Volume 1: Plasma Physics*. Plenum Press, New York, NY, USA, 1984.

[17] E. Y. Choueiri. On the thrust of self-field mpd thrusters. In *Proceedings of the 25th International Electric Propulsion Conference*, 1997.

[18] D. L. Chubb. Fully ionized quasi-one dimensional magnetic nozzle flow. In *Proceedings of the 9th AIAAAerospace Sciences Meeting*, Jan 1971.

[19] R. A. Clemente. On current drive in field-reversed configurations. *J. Phys. Soc. Japan*, 67:3450, 1998.

[20] S. A. Cohen, X. Sun, E. E. Ferraro, N. M. abd Scime, M. Miah, S. Stange, N. S. Siefert, and R. F. Boivin. On collisionless ion and electron populations in the magnetic nozzle experiment (mnx). *IEEE Transactions on Plasma Sciences*, 34:792–803, 2006.

[21] C. Deline, R. Bengtson, B. Breizman, M. Tushentsov, J. Jones, D. Chavers, C. Dobson, and B. Schuettpelz. Plume detachment from a magnetic nozzle. *Physics of Plasmas*, 16:033502, 2009.

[22] E. Distefano and H. J. Pain. Electrical current in a moving plasma between cold electrodes. *British Journal of Applied Physics*, 2:1085–1093, 1969.

[23] F. H. Ebersohn, B. W. Longmier, J. P. Sheehan, J. V. Shebalin, and S. S. Girimaji. Preliminary magnetohydrodynamic simulations of magnetic nozzles. In *Proceedings of 33rd International Electric Propulsion Conference*, October 2013.

[24] D. G. Fearn. An investigation of the electrical breakdown of a plasma-electrode system. *Journal of Plasma Physics*, 2, Ser. 2(3):527–533, 2009.

[25] A. Fruchtman, R. Gueroult, and N. J. Fisch. Rigid-body rotation of an electron cloud in divergent magnetic fields. *Physics of Plasmas*, 20:073502, 2013.

[26] A. Fruchtman, K. Takahashi, C. Charles, and R. W. Boswell. A magnetic nozzle calculation of the force on a plasma. *Physics of Plasmas*, 19:033507, 2012.

[27] R. A. Gerwin. Integrity of the plasma magnetic nozzle. Technical Report TP-2009-213439, NASA, 2009.

[28] J. Gilland and G. Johnston. Mpd thruster performance analytic models. In *AIP Conference Proceedings*, volume 654, 2003.

[29] D. M. Goebel and I. Katz. *Fundamentals of Electric Propulsion*. Wiley, Hoboken, NJ, USA, 2008.

[30] M. Hagler and M. Kristiansen. *An introduction to controlled thermonuclear fusion*. Lexington Books, Lanham, MD, USA, 1977.

[31] E. B. Hooper. Plasma detachment from a magnetic nozzle. *Journal of Propulsion and Power*, 9(5):757–763, 1993.

[32] R. Hoyt, J. Scheuer, K. Schoenberg, R. Gerwin, R. Moses, and I. Henins. Magnetic nozzle design for coaxial plasma accelerators. *IEEE Trans. Plasma Sci.*, 23:481–494, 1995.

[33] W. N. Hugrass. Control of the motion of the ions in rotating magnetic field current drive: 1. steady-state analysis. *Plasma Physics and Controlled Fusion*, 42:1219–1225, 2000.

[34] W. N. Hugrass. Control of the motion of the ions in rotating magnetic field current drive: 2. transient analysis. *Plasma Phys. Control. Fusion*, 45:209–219, 2003.

[35] I. Hutchinson. Ion collection by a sphere in a flowing plasma: I. quasineutral. *Plasma Physics and Controlled Fusion*, 44:1953–1977, 2002.

[36] I. H. Hutchinson. *Principles of Plasma Diagnostics, Second Edition.* Cambridge University Press, Cambridge, UK.

[37] A. V. Ilin, L. D. Cassady, G. T. W., and F. R. Chang Diaz. Vasimr human mission to mars. In *Proceedings of the Space, Propulsion and Energy Sciences International Forum*, March 2011.

[38] R. G. Jahn. *Physics of Electric Propulsion.* Dover, Mineola, NY, USA, 2006.

[39] J. L. Kline, E. E. Scime, R. F. Boivin, A. M. Keesee, X. Sun, and V. S. Mikhailenko. rf absorption and ion heating in helicon sources. *Phys. Rev. Lett.*, 88:195002, 2002.

[40] K. Kuriki and O. Okada. Experimental study of a plasma flow in a magnetic nozzle. *Phys. Fluids*, 13:2262–2269, 1970.

[41] D. Lev and E. Y. Choueiri. Scaling of anode sheath voltage fall with the operational parameters in applied-field mpd thrusters. In *Proceedings of the 32nd International Electric Propulsion Conference*, Sep 2011.

[42] A. F. Lifschitz, R. Farengo, and R. A. Clemente. The effect of ion motion on rotating magnetic field current drive. *Plasma Physics and Controlled Fusion*, 45:999–1012, 2003.

[43] J. M. Little and E. Y. Choueiri. Ion detachment in the helicon double-layer thruster exhaust beam. *Journal of Propulsion and Power*, 22:24–30, 2006.

[44] J. M. Little and E. Y. Choueiri. The influence of induced currents on magnetic nozzle acceleration and plasma detachment. In *Proceedings of 46th AIAA/ASME/SAE/ASEE Joint Propulsion Conference and Exhibit*, July 2010.

[45] J. M. Little and E. Y. Choueiri. High and low-efficiency detachment modes for magnetic nozzle plasma flows. In *Proceedings of 32rd International Electric Propulsion Conference*, September 2011.

[46] J. M. Little and E. Y. Choueiri. Plasma detachment and momentum transfer in magnetic nozzles. In *Proceedings of 47th AIAA/ASME/SAE/ASEE Joint Propulsion Conference and Exhibit*, July 2011.

[47] J. M. Little and E. Y. Choueiri. Plasma detachment and momentum transfer in magnetic nozzles. In *Proceedings of the 47th AIAA/ASME/SAE/ASEE Joint Propulsion Conference*, Jul 2011.

[48] J. M. Little and E. Y. Choueiri. Plasma transport in a converging magnetic field with applications to helicon plasma thrusters. In *Proceedings of 33rd International Electric Propulsion Conference*, October 2013.

[49] J. M. Little and E. Y. Choueiri. Thrust and efficiency model for electron-driven magnetic nozzles. *Physics of Plasmas*, 20(103501), 2013.

[50] B. W. Longmier and J. P. Sheehan. Initial experiments of a new permanent magnet helicon thruster. In *Proceedings of the 40th IEEE International Conference on Plasma Science*, June 2013.

[51] W. M. Manheimer and R. F. Fernsler. Plasma acceleration by area expansion. *IEEE Transactions on Plasma Sciences*, 29:75–84, 2002.

[52] J. J. Martinell and C. Gutiérrez-Tapia. Induction of poloidal rotation by a radial ponderomotive force of electron cyclotron waves. *Physics of Plasmas*, 8:2808–2815, 2001.

[53] R. L. Merlino. Understanding langmuir probe current-voltage characteristics. *American Journal of Physics*, 75:1078–1085, 2007.

[54] R. D. Milroy. Modeling of RMF Current Drive in a FRC. In *APS Division of Plasma Physics Meeting Abstracts*, Nov. 1998.

[55] R. D. Milroy. A magnetohydrodynamic model of rotating magnetic field current drive in a field-reversed configuration. *Physics of Plasmas*, 7(4135-4142), 2000.

[56] R. W. Moses, R. A. Gerwin, and K. F. Schoenber. Resistive plasma detachment in nozzle based coaxial thrusters. In *Proceedings of the 9th symposium on space nuclear power systems*, Jan 1992.

[57] L. Oksuz and N. Hershkowitz. Understanding mach probes and langmuir probes in a drifting, unmagnetized, non-uniform plasma. *Plasma Sources Science and Technology*, 13:263–271, 2004.

[58] C. S. Olsen, M. G. Ballenger, M. Carter, F. R. Chang Diaz, M. Giambusso, T. W. Glover, A. V. Ilin, J. P. Squire, B. W. Longmier, E. A. Bering, and P. A. Cloutier. An experimental study of plasma detachment from a magnetic nozzle in the plume of the vasimr engine. In *Proceedings of the 33rd International Electric Propulsion Conference*, Oct 2013.

[59] M. Passoni. Notes of the course "fisica dei plasmi". Dipartimento di Energia, Politecnico di Milano, 2013.

[60] J. Reece Roth. *Industrial Plasma Engineering: Volume 2 - Applications to Nonthermal Plasma Processing*. CRC Press, Boca Raton, FL, USA, 2001.

[61] N. Sakaguchi, Y. Kajimura, and H. Nakashima. Thrust efficiency calculation for magnetic nozzle in laser fusion rocket. *Trans. Japan Soc. Aero. Space Sci.*, 48:180–182, 2005.

[62] J. F. Santarius and B. G. Logan. Generic magnetic fusion rocket model. *Journal of Propulsion and Power*, 14:519–524, 1998.

[63] J. Sapan. Circuit simulations for the rmf/frc antenna system. Princeton Dep. of Electrical Engineering and PPPL, 2002.

[64] A. Sasoh. Simple formulation of magnetoplasmadynamic acceleration. *Physics of Plasmas*, 1:464, 1994.

[65] P. F. Schmit and N. J. Fisch. Magnetic detachment and plume control in escaping magnetized plasma. *Journal of Plasma Physics*, 75(3):359–371, 2009.

[66] K. F. Schoenberg, R. A. Gerwin, R. W. Moses, J. T. Scheuer, and H. P. Wagner. Magnetohydrodynamic flow physics of magnetically nozzled plasma accelerators with applications to advanced manufacturing. *Physics of Plasmas*, 5:2090–2104, 1998.

[67] J. P. Sheehan, Y. Raitses, N. Hershkowitz, I. Kaganovich, and N. J. Fisch. A comparison of emissive probe techniques for electric potential measurements in a complex plasma. *Physics of Plasmas*, 18:073501, 2011.

[68] J. Slough, D. Kirtley, and T. Weber. Pulsed plasmoid propulsion: The elf thruster. In *Proceedings of the 31st International Electric Propulsion Conference*, Sep 2009.

[69] L. C. Steinhauer. Transient and quasisteady behavior with rotating magnetic field current drive. *Physics of Plasmas*, 8:3367–3376, 2001.

[70] L. C. Steinhauer. Review of field-reversed configurations. *Physics of Plasmas*, 18(070501), 2011.

[71] G. P. Sutton. *Rocket Propulsion Elements, 7th Edition.* Wiley, New York, NY, USA, 2001.

[72] A. J. Theiss, R. A. Mahaffey, and A. W. Trivelpiece. Rigid-rotor equilibria of nonneutral plasmas. *Physical Review Letters*, 35:1436–1438, 1975.

[73] S. Tonooka, I. Funaki, T. Matsuoka, S. Iwabuchi, T. Nakamura, S. Shinohara, and N. H. Thrust characteristics of helicon plasma thrusters.

In *Proceedings of the 33rd International Electric Propulsion Conference*, Oct 2013.

[74] J. Vaclavik, M. L. Sawley, and F. Anderegg. The ponderomotive force in a magnetized plasma: The effect of radiofrequency induced magnetization. *Physics of Fluids*, 29:2034–2037, 1986.

[75] D. C. Visentin. Ion motion control in rmf current drive by means of a frequency modulated counter-rmf. *Plasma Phys. Control. Fusion*, 45:1027–1035, 2003.

[76] W. Von Jaskowsky, A. J. Kelley, R. G. Jahn, and J. E. Polk. Measurement of mpd thruster erosion using surface layer activation. *Journal of Propulsion and Power*, 3:33–38, 1987.

Appendix A

Propulsive performance of finite temperature plasma flow in a magnetic nozzle with applied azimuthal current

(Paper to be submitted to Physics of Plasmas)

Propulsive performance of a finite-temperature plasma flow in a magnetic nozzle with applied azimuthal current

Lorenzo Ferrario,[a] Justin M. Little,[b] and Edgar Y. Choueiri[c]

A solution is presented for the flow in a finite-electron-temperature magnetic nozzle under the influence of an applied azimuthal current at the throat. A correction to the nozzle throat boundary conditions is derived by modifying the radial equilibrium of a magnetized infinite two-population cylindrical plasma column with the insertion of an external azimuthal body force for the electrons. The nozzle flow is then solved using a previously developed approximate analytical model, properly modified. The sensitivity of the nozzle propulsive performance is assessed in terms of beam divergence, nozzle divergence efficiency, thrust coefficient and normalized specific impulse. The results show that, under the hypotheses of work, all the analyzed performance parameters are positively affected by the external body force through the narrowing of the radial density profile at the throat. This eventually opens the possibility for a future design of a focusing stage between the plasma source and the magnetic nozzle, increasing the performances of the nozzle.

I. INTRODUCTION

A Magnetic Nozzle (MN) is a propulsive device that converts part of the thermal energy of a plasma into direct kinetic energy. Application of such nozzles can be found in fundamental plasma physics experiments,[1] plasma processes[2–4] and plasma propulsion for spacecraft.[5–12]

The underlying mechanism in such devices relies on high plasma conductivity.[13] This so called frozen-in condition forces the plasma to follow the magnetic stream surfaces as they expand through the nozzle. This property allows the magnetic nozzle to guide the plume much like the gasdynamic expansion in conventional rocket nozzles. The momentum is then transferred back to the thruster by the mutual interaction of induced diamagnetic currents in the plume and the applied magnetic field.[8]

The flexibility of MNs allowed a number of proposed application in plasma propulsion, such as helicon thrusters,[14] permanent magnet micropropulsion systems for cubesat,[15] VASIMR architecture[5] and proposed fusion rockets.[16,17]

The absence of electrodes, often identified as the life-limiting components of other electric propulsion systems[18], and the ability to scale to high power[5] make the MN a desirable option for the acceleration stage for pre-ionized gaseous propellants.

When the thermal energy is stored mainly in the electrons ($T_e \gg T_i$), the functioning mechanism can be described as *thermal* for the electrons fluid, and *electrostatic* for the ions. Such devices are therefore called Electron-Driven Magnetic Nozzles (EDMN).[12] In this class of magnetic nozzles, the thermal energy stored in the electrons drives them in a thermal expansion in the divergent field. The ions, on the contrary, are much cooler and tend to remain confined in the plasma source. Therefore, an ambipolar electric field arises to conserve local quasi-neutrality[19] and accelerates ions, thus producing thrust.

A. Open problems in Magnetic Nozzle theory

While MNs have been already implemented in various thruster prototype architectures,[5,14–17] their governing physics have yet to be fully understood and the plasma dynamics in MNs are still an active field of research.

Among other problems, plasma detachment is a central issue affecting thrust production in MN, and has been investigated through a number of simulations[10,11,20] and analytical models.[6,7,21] Recently, Deline et al.[22] provided the first experimental evidence of plasma detachment in such MNs flows. However, the divergence in plasma flow in MNs has an obvious adverse effect in thrust production and nozzle efficiency.

How and where this detachment occurs is still under a vivid scientific debate. Previously accepted theories of resistive[7] and electron inertia[6] detachment mechanism has recently been questioned[10,11], while experimental measures[5] did not verify the stretching to the infinite of the magnetic field lines as foreseen by Arefiev.[21]

Other problems affecting MNs-based thrusters are poor thermal-kinetic power conversion efficiency[23] at low power and magnetic field, and poor ionization.

B. Motivation and Scope

In their paper,[9] Schmit and Fisch expanded Hooper's[6] nozzle model, introducing an azimuthal current that, coupling with the axial magnetic field, produces a significant decrease in the plume divergence.

However, through numerical solution of a finite-temperature plasma flow model, Ahedo and Merino[10] showed that the hypotheses of negligible pressure effect and absent ambipolar current used by Hooper's model prevents from really understand the thermal-electrostatic

[a] Politecnico di Milano, Princeton University; lorenzo.ferrario@asp-poli.it
[b] Princeton University; jml@princeton.edu
[c] Princeton University; http://alfven.princeton.edu

nature of the plasma expansion in magnetic nozzles. As consequence of this analysis, it became clear that also to assess the effect of an applied azimuthal current a finite-temperature model of the plasma flow must be used. Thus, in this paper we wish to extend Schmit and Fisch's idea to Ahedo and Merino's model to have a more complete description of the interaction between the azimuthal current and the plasma flow.

Schmit and Fisch showed that a decrease in the plume divergence is observed when introducing the azimuthal current and they suggest this divergence reduction leads to an increase in the nozzle efficiency. Therefore, we wish also to assess the effects of the azimuthal current on the propulsive performance of the nozzle.

Finally, the introduction of an azimuthal current is an active process and, as such, requires some additional power to be provided to the plume. Thus, it is natural to ask ourselves if the introduction of this azimuthal current is an efficient way of recovering direct kinetic power, or, in other terms, how the direct kinetic power recovery relates with the applied power.

C. Approach

When we apply an azimuthal current at the nozzle throat, an interaction between the Lorentz force and the radial pressure expansion term arises, changing the equilibrium state of the plasma. Therefore, if we want to apply an externally induced swirl motion to a finite temperature model, we need also to modify the nozzle throat conditions consistently with the new equilibrium.

We start by solving the equations of an infinite plasma column in steady equilibrium, confined by an axial external magnetic field, with an applied body force in the azimuthal equation. Mathematically speaking, we are adding a variable that would eventually be defined with an additional equation. Once the new throat boundary conditions are defined, we solve the two dimensional axysimmetric flow in the nozzle and we evaluate the effect on the nozzle performance.

By imposing the sum of the radial components of the Lorentz and the centrifugal forces to be negative

$$F^{\theta}_{a\,r} = q_a B_z u_{\theta a} + m_a \frac{u^2_{\theta a}}{r} < 0 \quad , \tag{1}$$

we can find a condition on the angular velocity at the nozzle throat ($\omega^t_a = u^t_{\theta a}/R^t$) of each species streamline by which such radial force has a net collimating effect. Using the superscript t to indicate the quantities at the throat, we get

$$-\Omega_z \frac{r^2}{{R^t_a}^2} - 2\frac{q_a}{m_a {R^t_a}^2}\left(\psi^t - \psi\right) < \omega^t_a < 0 \quad , \tag{2}$$

where Ω_z is the local cyclotron frequency magnitude of the *a-th* species, computed with the axial magnetic field B_z and ψ is the magnetic streamfunction, defined according to

$$\mathbf{B} = \frac{1}{r}(\hat{\vartheta} \times \nabla\psi) \quad . \tag{3}$$

We can specialize the equations for a two species (electrons and ions) plasma. In this situation, we know that $\psi^0 - \psi \geq 0$ for the ions, due to their inward separation from the magnetic streamlines,[10] and $\psi^0 - \psi \approx 0$ for the electrons[11], due to their high magnetization, typical of most of the practical applications of EDMNs.[1,5] Therefore, since $r \geq R^0$ along all the divergent streamline, the strictest condition is found at the nozzle throat, which is:

$$\begin{cases} -\Omega^0_i < \omega^0_i < 0 \\ 0 < \omega^0_e < \Omega^0_e \quad . \end{cases} \tag{4}$$

If these inequalities are met, the radial component of the Lorentz force dominates over the centrifugal force, leading to a net collimating effect along all the streamline.

From condition 4, we see that electrons have a range of admissible angular velocities that is much wider than that of the ions due to the high ion-electron mass ratio. Thus, we will focus our attention on the electron fluid, also because is easier for the electrons to carry the current.[24–26]

D. Paper Outline

This paper is organized as follows: first, the radial equilibrium in an infinite magnetized plasma column with the presence of an electron azimuthal body force is modeled analytically. Then, the solution is used as boundary condition at the throat of a magnetic nozzle, and the flow in the divergent is computed using an analytical approximation. In the final Sec. IV, the effects of the introduced electron body force on the nozzle propulsive performances are presented and discussed.

II. NOZZLE THROAT BOUNDARY CONDITIONS IN SWIRLING REGIME

A. Equilibrium Equations for an Infinite Column of Magnetized Plasma

We consider an infinite cylindrical plasma column, with an externally applied axial magnetic field. In this section we will write the modified equilibrium equation for such a plasma configuration under the effect of an externally applied azimuthal body force F.

We also make the assumption of low-β, which allows us to neglect the induced magnetic field and we consider a two species plasma (electrons and singly charged ions)

where local quasi-neutrality $n_e = n_i = n$ holds everywhere. Following Ahedo,[27] we assume equal radial velocities of electrons and ions $u_{ri} = u_{re} = u_r$. This is generally true in the plasma central region, where the charge separating electric field of the sheath is not yet significant.

Since the propulsive parameters defined in Sec. IV are mostly influenced by the densest region of the plume, we will limit our investigation to that region.

The modified momentum equation in cylindrical coordinates (r, θ, z), assuming axysimmetry $(\partial/\partial\theta = 0)$ and dropping the axial derivatives $(\partial/\partial z = 0)$ in the azimuthal direction for the electrons is:[27]

$$\begin{aligned} m_e u_r \frac{du_{\theta\mathrm{e}}}{dr} + m_e \frac{u_{\theta\mathrm{e}} u_r}{r} = \; & eBu_r - m_e(\nu_{\mathrm{en}} + \nu_w)u_{\theta\mathrm{e}} \\ & - m_e \nu_{\mathrm{ei}}(u_{\theta\mathrm{e}} - u_{\theta\mathrm{i}}) + F \end{aligned} \tag{5}$$

where ν_{en}, ν_{ei} are the electron-neutral and electron-ion collision frequencies, respectively, and ν_w is the ion production frequency, due to axial diffusion and ionization of neutrals. We introduce F in Eq. 5 as a generalized body force acting on electrons only, that induces the differential motion in the two species required to create a net azimuthal current. The other three momentum equations and the continuity equation are left unchanged:

$$\begin{aligned} m_e u_r \frac{du_r}{dr} - m_e \frac{u_{\theta\mathrm{e}}^2}{r} = \; & -\frac{1}{n}\frac{d}{dr}(T_e n) + e\frac{d\phi}{dr} - eBu_{\theta\mathrm{e}} \\ & - m_e(\nu_{\mathrm{en}} + \nu_w)u_r \quad , \end{aligned} \tag{6}$$

$$\begin{aligned} m_i u_r \frac{du_r}{dr} - m_i \frac{u_{\theta\mathrm{i}}^2}{r} = \; & -\frac{1}{n}\frac{d}{dr}(T_i n) + e\frac{d\phi}{dr} + eBu_{\theta\mathrm{i}} \\ & - m_i(\nu_{\mathrm{in}} + \nu_w)u_r \quad , \end{aligned} \tag{7}$$

$$\begin{aligned} m_i u_r \frac{du_{\theta\mathrm{i}}}{dr} + m_i \frac{u_{\theta\mathrm{i}} u_r}{r} = \; & -eBu_r - m_i(\nu_{\mathrm{in}} + \nu_w)u_{\theta\mathrm{i}} \\ & + m_i \nu_{\mathrm{ei}}(u_{\theta\mathrm{e}} - u_{\theta\mathrm{i}}) \quad , \end{aligned} \tag{8}$$

$$\frac{1}{r}\frac{d}{dr}(rnu_r) = \; n\nu_w \quad . \tag{9}$$

We follow Ahedo by dropping the electric potential gradient in the plasma bulk region ($\nabla\phi = 0$) and nondimensionalizing the equations using the sheath coordinate R_s, the sonic speed $c_s = \sqrt{T_e/m_i}$, the density on the axis n_0, the electron energy T_e, which is considered constant. The frequencies are nondimensionalized by c_s/R_s.

We define also the nondimensional azimuthal velocity of electrons as

$$\hat{u}_{\theta\mathrm{e}} = \frac{u_{\theta\mathrm{e}}}{c_s}\sqrt{\frac{m_e}{m_i}} \tag{10}$$

and the nondimensional lower-hybrid frequency as

$$\hat{\omega}_{\mathrm{lh}} = \frac{eB}{\sqrt{m_i m_e}}\frac{R_s}{c_s} \quad . \tag{11}$$

Manipulating Eq. 5 dropping the inertia terms and under the hypotheses of cold ions $(T_i \approx 0)$[10–12,27] and negligible ionic azimuthal motion $(u_{\theta\mathrm{i}} \approx 0)$,[27] we get the modified expression for the radial velocity

$$\hat{u}_r = \frac{\hat{\nu}_e}{\hat{\omega}_{\mathrm{lh}}} - \frac{\hat{F}}{\hat{\omega}_{\mathrm{lh}}} \quad , \tag{12}$$

where $\hat{\nu}_e = \hat{\nu}_{\mathrm{ei}} + \hat{\nu}_{\mathrm{en}} + \hat{\nu}_w$. From Eq. 12 we can immediately see how the azimuthal body force $\hat{F}$ couples with the magnetic field to modify the radial velocity profile. Indeed, it is clear from Eq. 12 that a positive force $\hat{F}$ would reduce the outward-directed radial velocity. Physically, we see that a positive $\hat{F}$ induces a diamagnetic current that couples with the axial magnetic field, giving an inward-directed Lorentz force that radially confines the plasma.

From the radial momentum balance on the electrons we get

$$\hat{\omega}_{\mathrm{lh}}\hat{u}_{\theta\mathrm{e}} = -\frac{d\ln\hat{n}}{d\hat{r}} \quad , \tag{13}$$

which, together with the continuity equation, leads to the modified diffusion equation:

$$\frac{d^2\hat{n}}{d\hat{r}^2} + \left(\frac{1}{\hat{r}} + \frac{\hat{\omega}_{\mathrm{lh}}}{\hat{\nu}_e}\hat{F}\right)\frac{d\hat{n}}{d\hat{r}} + \left(a_0^2 + \frac{\hat{\omega}_{\mathrm{lh}}}{\hat{\nu}_e}\frac{d\hat{F}}{d\hat{r}} + \frac{\hat{\omega}_{\mathrm{lh}}}{\hat{\nu}_e}\frac{\hat{F}}{\hat{r}}\right)\hat{n} = 0 \quad , \tag{14}$$

where

$$a_0 = \hat{\omega}_{\mathrm{lh}}\sqrt{\frac{\hat{\nu}_w}{\hat{\nu}_e}} \quad . \tag{15}$$

This equation is a second-order ODE, with boundary conditions on the axis $\hat{n}(0) = 1$ and $\hat{n}'(0) = 0$, whose solution clearly depends on the particular choice of $\hat{F}$. The integration is stopped when the sheath is reached, thus for $\hat{u}_r = 1$ in accordance with the Bohm condition.[28]

We see from Equation 12 and Equation 14 that the azimuthal body force $\hat{F}$ couples with the magnetic field, parametrized by $\hat{\omega}_{\mathrm{lh}}$, modifying the diffusion equation and eventually the radial density profile of the plasma. From the same equation we see that the net effect of the body force is scaled by the ratio $\hat{\omega}_{\mathrm{lh}}/\hat{\nu}_e$, which is the ratio of the non-dimensional magnetic field parameter and the electron global collisional term. In other words, the effect of the body force is proportional to the magnetization, which rules the strength of the Lorentz interaction, and is inversely proportional to the electron collisional term, which acts as momentum sinks for the electronic population.

B. Application to a Particular Form of $\hat{F}$

We now proceed by assuming a particular form of $\hat{F}$ in order to solve Eq. 14. The quantitative results will depend strictly on this choice, but some consideration on the behavior of the plasma can be generalized to a broader class of body forces. We choose $\hat{F}$ to be

$$\hat{F} = \hat{\Omega}\hat{r} - \hat{u}_{\theta \mathrm{e}} \quad , \tag{16}$$

which causes the azimuthal motion of the electrons to tend to a rigid body motion with angular frequency $\hat{\Omega}$. Clearly, this body force vanishes when the electrons are moving collectively at the desired angular frequency and changes sign for higher $\hat{u}_{\theta \mathrm{e}}$.

Secondly, we note that a positive $\hat{\Omega}$ would induce a diamagnetic electron current, while a negative $\hat{\Omega}$ would induce a paramagnetic one. (Such a definition of $\hat{F}$ resembles the effect of Rotating Magnetic Field (RMF) used to drive electron currents in fusion experiments.[29] Quantitatively, such definition of $\hat{F}$ correspond to a generalization of the force exerted by the RMF on the electrons within the approximation of fixed ions[25] and of $\hat{\Omega}_{\mathrm{ce}}^2 \gg \nu_{\mathrm{ei}}^2$, which is justified by the low residence time of the ions in the thruster.)

Finally, we can substitute Eq. 16 into Eq. 12

$$\hat{u}_r = \frac{\hat{\nu}_e + 1}{\hat{\omega}_{\mathrm{lh}}} - \frac{\hat{\Omega}\hat{r}}{\hat{\omega}_{\mathrm{lh}}} \quad , \tag{17}$$

and Eq. 14

$$\frac{d^2\hat{n}}{d\hat{r}^2} + \left(\frac{1}{\hat{r}} + \left(\frac{\hat{\omega}_{\mathrm{lh}}\hat{\Omega}}{\hat{\nu}_e + 1} \right) \hat{r} \right) \frac{d\hat{n}}{d\hat{r}} + \left(a_{\hat{\Omega}}^2 + 2 \left(\frac{\hat{\omega}_{\mathrm{lh}}\hat{\Omega}}{\hat{\nu}_e + 1} \right) \right) \hat{n} = 0 \ , \tag{18}$$

where

$$a_{\hat{\Omega}} = \hat{\omega}_{\mathrm{lh}} \sqrt{\frac{\hat{\nu}_w}{\hat{\nu}_e + 1}} \quad . \tag{19}$$

C. Solution for Plasma Bulk Region

From Eq. 18 we see that, when $\hat{F} = 0$, i.e. when no azimuthal momentum is added to the column, we retrieve the original diffusion equation of Ahedo,[27] whose solution is given by

$$\hat{n}(\hat{r}) = J_0(a_{\hat{\Omega}}\hat{r}) \quad . \tag{20}$$

For finite $\hat{F}$, solutions for equation 18 can be obtained either analytically (the analytical solution is too lengthy to quote here) or numerically and are plotted in Fig. 1, where we show the radial profiles of $\log_{10}(\hat{n})$, $\hat{u}_{\theta \mathrm{e}}$ and $\hat{u}_{\mathrm{re}}$ with $\hat{\Omega}$ taken as varying parameter.

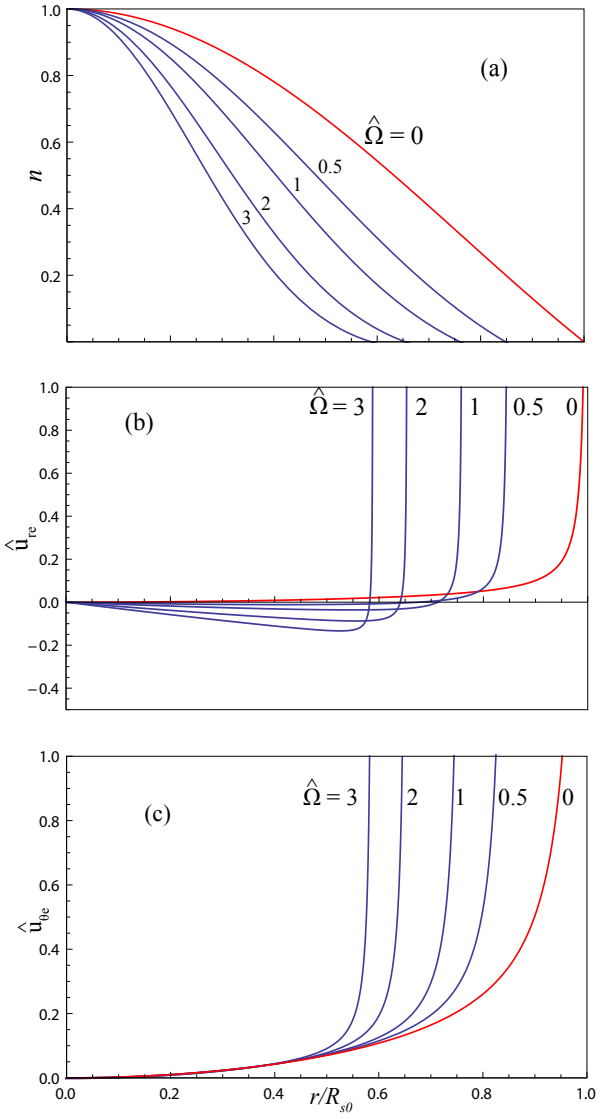

FIG. 1. Radial profile of different plasma quantities at different values of $\hat{\Omega}$. The radial coordinate is normalized on R_{s0}, which is the sheath position in case of $\hat{\Omega} = 0$. All other radial profiles are normalized on the respective $R_s(\hat{\Omega})$. Reference parameters $\hat{\omega}_{\mathrm{lh}} = 10$; $\hat{\nu}_e = \hat{\nu}_i = 1$. The profiles marked in red are the reference solution for $\hat{\Omega} = 0$.

It is clear from Fig. 1(a) that the radial density profile of the plasma column changes significantly even for low values of $\hat{\Omega}$. The resulting shape of the density distribution shows a change in the sign of the second derivative, leading to a steeper decay at greater values of $\hat{r}$. Even more importantly, Figure 1(a) shows that the radius to the sheath edge, R_s, depends on $\hat{\Omega}$ and decreases monotonically with the increase of the force parameter, thus leading to more axial contained of the plasma.

By plotting this dependency in Figure 2, we see a strong decrease of R_s for $\hat{\Omega} < 2$, with the decrease rate reducing after the knee. This knee is more marked for

higher value of the magnetization parameter $\hat{\omega}_{\rm lh}$. No horizontal asymptote has been identified, and R_s decreases monotonically to 0 for $\hat{\Omega} \to \infty$. The enhancement of confinement with increasing force goes on until the validity of the physical model is violated by the neglected electron inertia terms and of the diamagnetically-induced magnetic field.

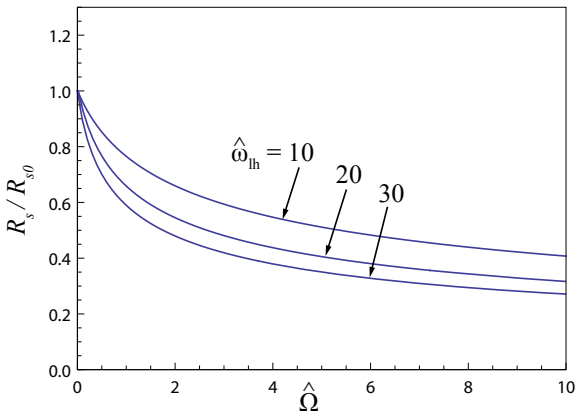

FIG. 2. Sheath coordinate variation with $\hat{\Omega}$ at different values of $\hat{\omega}_{\rm lh}$. Reference parameters $\hat{\nu}_e = \hat{\nu}_i = 1$.

From Fig. 1(c), we see that the confining action is limited to a thin high-current layer, whose thickness decreases with the raise of $\hat{\Omega}$.

We can identify two regions in the radial velocity profile depicted in Fig. 1(b). Internally, the confining Lorentz force dominates over the pre-sheath pull, and the radial velocity is negative. In the external region, the magnitude of the confining effect diminishes and the density gradient pushes away the few particles present in that region, allowing them to reach the sonic condition and enter the plasma sheath.

D. Body Force Power Validity Domain

The external power required to apply $\hat{F}$ can be computed by

$$\mathcal{P}_{\hat{F}} = \int_A \hat{F}\; n\; \hat{u}_{\theta \rm e} \sqrt{\frac{m_i}{m_e}} dA \quad , \tag{21}$$

where the scaling term $\sqrt{m_i/m_e}$ is introduced for accounting for the definition of $\hat{u}_{\theta \rm e}$ given in Eq. 10.

By evaluating this integral, we see that the result can be negative for low enough value of $\hat{\Omega}$, thus resulting in an extraction of power from the column. This unphysical result is related to the definition of $\hat{F}$ of Eq. 16, where the sign of the body force depends on the relative magnitudes of $\hat{\Omega} r$ and $\hat{u}_{\theta \rm e}$ Thus, we limit the validity of the analysis on the jet and body force powers for $\hat{\Omega} \geq 0.5$. All the other quantities show well-behaved trends even for lower values of $\hat{\Omega}$, thus we retain the full solutions in these cases for completeness.

III. NOZZLE FLOW ANALYTICAL SOLUTION

With the modified solution of the magnetized plasma column, we may now proceed to compute the new nozzle flow characteristics. Specifically, we will use the new radial density profile as boundary condition at the throat of an electron-driven magnetic nozzle to solve the two-dimensional expansion of a plasma. This coupling models the implementation of a "focusing stage" before the nozzle throat in a thermal plasma thruster.

A. Model Assumptions and Governing Equations

For this analysis, we will use and expand the analytical approximated model of Little and Choueiri[12]. Their model uses a coordinate transformation from physical (r, z) to magnetic (ψ, ζ), where ψ is the magnetic stream function and ζ is the magnetic scalar potential[32].

$$\mathbf{B} = \frac{1}{r}(\hat{\vartheta} \times \nabla\psi) = -\nabla\zeta \quad . \tag{22}$$

This transformation allows to write the balance equations along and across the magnetic surfaces, which are more representative of the magnetic nozzle physics than the geometric (r, z) and remove the singularities after the magnetic field turning point.

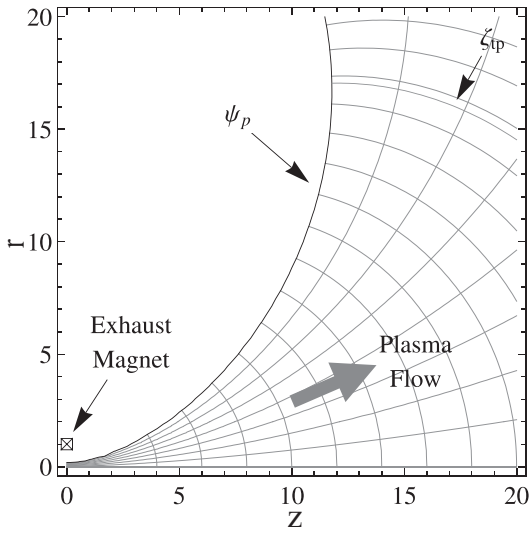

FIG. 3. Magnetic nozzle field topology[12]. The grid shows the transformation from geometric coordinates (r, z) to magnetic (ψ, ζ). The plasma-vacuum interface is marked by the stream coordinate ψ_p. The plasma-vacuum magnetic surface turning point has coordinate $\zeta_{\rm tp}$.

Little and Choueiri's model integrates the plasma equations along the magnetic streamlines ψ, with the nozzle throat plane as boundary condition. We will follow here the same scheme, modifying the equations for the case of non-zero azimuthal velocities of electrons.

The adopted non-dimensionalization uses the coil radius a_e as reference length, the electron temperature T_e for the energies and the sonic speed $c_s = \sqrt{T_e/m_i}$. From the electron momentum equation multiplied by the magnetic versor $\mathbf{b}$

$$\mathbf{b} \cdot \nabla \left(\phi - \ln(n)\right) = \mathbf{b} \cdot \left(\mathbf{M}_e \times \left(\frac{\mathbf{B}}{\rho_e}\right)\right) \quad , \tag{23}$$

leading to

$$\mathbf{b} \cdot \nabla \left(\phi - \ln(n)\right) = 0 \quad . \tag{24}$$

Thus, the electrons still follow the Boltzmann relation along the streamline, without any trace of the action of $M_{\theta \mathrm{e}}$, in agreement with the transversal direction of the Lorentz force.

$$n(\psi, \zeta) = n_t(\psi) e^{\left(\phi(\psi,\zeta) - \phi^0(\psi)\right)} \quad . \tag{25}$$

The introduction of a new variable ($M_{\theta \mathrm{e}}$) requires an additional equation, which is taken from the conservation of angular momentum along the streamlines, under the hypothesis of magnetized electrons.

$$\mathbf{b} \cdot \nabla \left(M_{\theta \mathrm{e}} r\right) = 0 \quad . \tag{26}$$

Retaining for the moment the so-far neglected ionic azimuthal velocity $M_{\theta \mathrm{i}}$, we evaluate the electric potential through the projection of the momentum equation for the ions across $\mathbf{b}$.

$$\frac{\partial \phi}{\partial \psi} = -KM^2 + \frac{M_{\theta \mathrm{i}}}{r} \quad . \tag{27}$$

From this equation we see that the ion swirling affects explicitly the potential distribution. We could explicit the effect of the electron swirl on the density by composing Eq. 27 with the electron cross-field momentum equation, leading to a cross field equation for the density

$$\frac{\partial \ln n}{\partial \psi} = -KM^2 + \frac{M_{\theta \mathrm{i}} - M_{\theta \mathrm{e}}}{r} \quad . \tag{28}$$

This equation affects the boundary conditions at the nozzle throat (n_t), which has to be consistent with the presence of a finite electron current $M_{\theta \mathrm{e}}$.

From these equations, we conclude that the presence of differential species swirling influences the two-dimensional density distribution inside the magnetic nozzle in two ways: the ion azimuthal current and kinetic energy recovery induce a change in the potential profile ϕ across the magnetic streamlines, while the electron current changes the boundary conditions at the nozzle throat, n_t. Here arises a strong difference with what previously observed by Schmit and Fisch[9]. According to our equations, the effect of introducing an electron swirling motion is recorded at the nozzle throat and what happens in the divergent part of the nozzle is the propagation of the modified equilibrium state throughout the plume, according to the hyperbolic nature of the supersonic fluid equations. This allows the modified radial density distribution to propagate along the nozzle, even outside the region of influence of F. This observation implies that the actual effect of an azimuthal current cannot be correctly modeled by using a zero-temperature model. Indeed, in such a case, the radial Lorentz force induced by the swirling would not be balanced by any pressure, leading to a non-equilibrium situation in contrast with the steady state regime of operation of MNs.

B. Throat Boundary Conditions

The boundary conditions at the nozzle throat are reported in Eq. 29.

$$\begin{cases} \phi(\psi, \zeta_t) = 0 \\ M_z(\psi, \zeta_t) = 1 \\ M_{\theta \mathrm{i}}(\psi, \zeta_t) = 0 \end{cases} \quad . \tag{29}$$

A new boundary condition for the variable $M_{\theta \mathrm{e}}(\psi, \zeta)$ has to be added to the set. The final boundary condition comes from the radial density profile in magnetic coordinates

$$\begin{cases} M_{\theta \mathrm{e}}(\psi, \zeta_t) = M^0_{\theta \mathrm{e}}(\psi) \\ n(\psi, \zeta_t) = n_t(\psi) \end{cases} \quad . \tag{30}$$

The boundary condition on the density Eq. 30(b) has to be consistent with the azimuthal current at the nozzle throat Eq. 30(a), thus we apply the infinite plasma column solution with F presented in Sec. II as boundary condition at the throat for both density and azimuthal velocity.

In order to conserve the mass flux at the throat, we expect the plasma density $n(r, \hat{\Omega})$ along the axis to be higher in the swirled case than in the reference situation, that is

$$n(0, \hat{\Omega}) > n(0, 0) \quad \text{for any} \quad \hat{\Omega} > 0 \quad , \tag{31}$$

thus, the density profile at the boundary, $n_t(\psi)$, is scaled by the ratio

$$\rho(\hat{\Omega}) = \int_0^{R_s(\hat{\Omega})} \hat{r}\ \hat{n}(\hat{r}) d\hat{r} \Bigg/ \int_0^{R_{s0}} \hat{r}\ \hat{n}(\hat{r}) d\hat{r} \quad . \tag{32}$$

From Fig. 4 we see the combinations of the two effects of the application of F. First, the plasma column is compressed to a narrower region, thus the value of the plasma boundary radius at the throat $R_s(\hat{\Omega})$ decreases. Then, for mass flux conservation, the relative density peak value in the throat center increases. We note that the raise of this peak dominates over the decrease of r_e^F due to the quadratic dependence of the mass flux on the radius. Therefore, we expect that the nozzle performances related to the density peak value will be more affected than those dependent on the sheath radius.

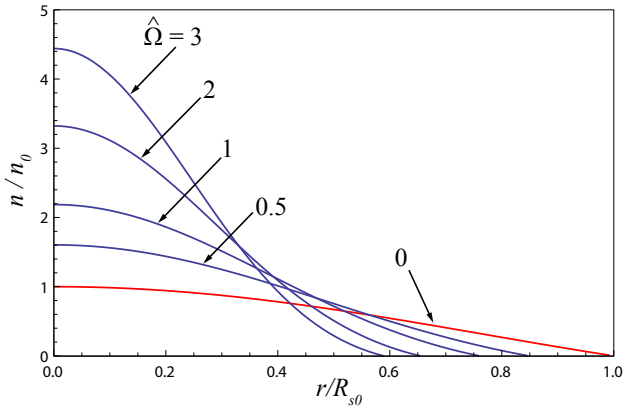

FIG. 4. Change in the non-dimensional plasma radial density profile at the throat with $\hat{\Omega}$, when the flux-conserving scaling is applied. The red line is the baseline for $\hat{\Omega} = 0$. Magnetization parameter $\hat{\omega}_{\rm lh} = 10$.

C. Magnetic Nozzle Flow in Electron Swirling Regime

Having modified the equations and closed the system of boundary conditions, we can now solve the plasma flow in the magnetic nozzle, comparing the new results with the baseline no-swirling solution of Little and Choueiri.[12]

From Figure 5 we observe that the flow has more elongated density lobes and the density decays faster near the border, since the cross-field derivative is higher in magnitude.

Moreover, the turning point is pushed downstream. This leads to a plume with lower divergence at constant expansion ratio, thus a greater nozzle efficiency and thrust coefficient is achieved, as described in Sec. IV.

IV. PROPULSIVE PERFORMANCE ASSESSMENT

In this last section, we use the modified nozzle flow solution to assess the effects of the swirling on the propulsive performances of the magnetic nozzle.

A. Efficiency Model

After Little and Choueiri,[12] we define the divergence efficiency of the nozzle as the ratio between the axial kinetic power in the plume and the total kinetic power at the magnetic field turning point ζ_{tp}. Under the quasi-field aligned assumption, this ratio reads:

$$\eta_{\rm div} = \frac{\mathcal{P}_b^*}{\mathcal{P}_b} = \int_{\zeta_{tp}} nM^3 \frac{B_z^2}{B^2} dA \Bigg/ \int_{\zeta_{tp}} nM^3 dA \quad . \tag{33}$$

This divergence efficiency is related to the overall nozzle efficiency through the relation $\eta_n = \eta_i \, \eta_{\rm div}$, where η_i takes into account all other sources of losses. It is clear

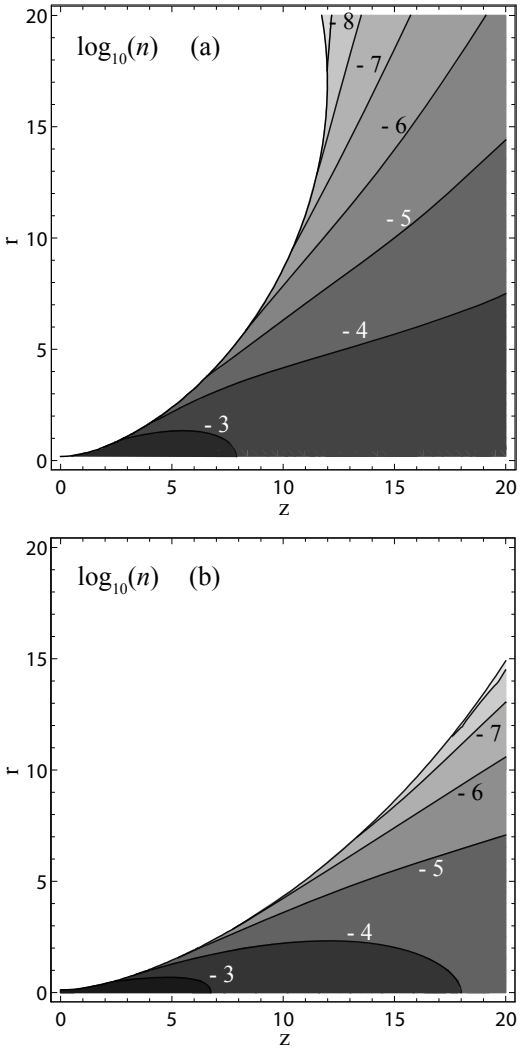

FIG. 5. Change in plasma flow density for $\hat{\Omega} = 2$. Upper graph baseline r_e is 0.185 for $\hat{\Omega} = 0$. Magnetization parameter $\hat{\omega}_{\rm lh} = 10$. Fig. (a) is the baseline no-swirl solution. Fig. (b) is the solution after the application of F.

that a plume focusing affects mainly $\eta_{\rm div}$, however, also η_i might be beneficially affected thanks to improved plasma-helicon wave coupling[30,31] (in helicon plasma sources) and reduced wall losses.

The thrust coefficient C_T is defined as

$$C_T = \frac{1}{\bar{n}_t A_t} \int_{\zeta_{tp}} n \left(M^2 + 1\right) \frac{B_z}{B} dA \quad , \tag{34}$$

where the quasi-field aligned hypothesis has again been used. The non-dimentional thruster specific impulse depends on both η_n and C_T

$$\hat{I}_{\rm sp} = \frac{g_0 I_{\rm sp}}{c_s} = \eta_n C_T \quad . \tag{35}$$

Through the nozzle flow solution, we can also evaluate the plume divergence. Little and Choueiri derives

an handy relation between the divergence half-angle $\theta_{\rm div}$ and a parameter $\Psi_{1/2}$ defined as the coordinate ψ/ψ_p at which the density at ζ_{tp} is half its value on the axis. This $\Psi_{1/2}$ is computed through

$$\frac{n(\Psi_{1/2},\zeta_{tp})}{n(0,\zeta_{tp})} = \frac{1}{2} \quad . \tag{36}$$

Since n_t is no longer a Bessel function, in our case this equation is solved numerically. Then, the divergence angle is computed as $\cos(\theta_{\rm div}) \approx 1 - \Psi_{1/2}$.

B. Nozzle Performance Assessment

In Fig. 6 and Fig. 7 we plot the dependency of plume divergence, thrust coefficient and divergence efficiency on the the force parameter $\hat{\Omega}$ at different values of magnetization factor $\hat{\omega}_{\rm lh}$ and throat radius r_e.

The efficiency in Fig. 6(c) and Fig. 6(d) raises as the divergence decreases, Fig. 6(a) and Fig. 6(b). We note that the increase of the efficiency follows the trend of Fig. 8 of Little and Choueiri,[12]. Therefore, we conclude that such an enhancement is almost completely due to the reduction of the sheath coordinate rather than to the density scaling.

A much higher improvement is recorded for the thrust coefficient, as plotted in Fig. 7. Indeed, in contrast with the efficiency, the thrust coefficient depends also on the density scaling of Eq. 32 and Fig. 4.

From Eq. 35, we can also plot the increase in specific impulse

$$\frac{\Delta \hat{I}_{\rm sp}}{\hat{I}_{\rm sp0}} = \frac{\Delta\left(C_T\ \eta_{\rm div}\right)}{C_{T0}\ \eta_{\rm div0}} \quad . \tag{37}$$

As for R_s, an higher grade of magnetization strengthen the effect, accentuating the knee below $\hat{\Omega} \approx 2$. For high values of $\hat{\Omega}$ we see a stabilization in the difference between the performance increase at different values of magnetization, while the difference is monotonically increasing if the curves are parametrized according to r_e. This might suggest that an high value of $\hat{\omega}_{\rm lh}$ is convenient only if $\hat{\Omega}$ is kept relatively low.

From these Figures, we see that a stronger effect is achieved for high values of r_e, which is for initially inefficient designs of the nozzle.[12] Therefore, it becomes reasonable to design magnetic nozzles with a "focusing stage" before the throat. This would allow to have smaller nozzle coils, thus lowering the power losses, without reducing the thruster efficiency.

These results makes of the concept of focusing stage a promising mean to increase the nozzle efficiency for all the applications where magnetic nozzles have place, even outside the field of plasma propulsion. Indeed, such focusing system would provide a way to actively tune the width of the plasma plume, a degree of freedom that can be very useful, for example, for plasma surface processing.

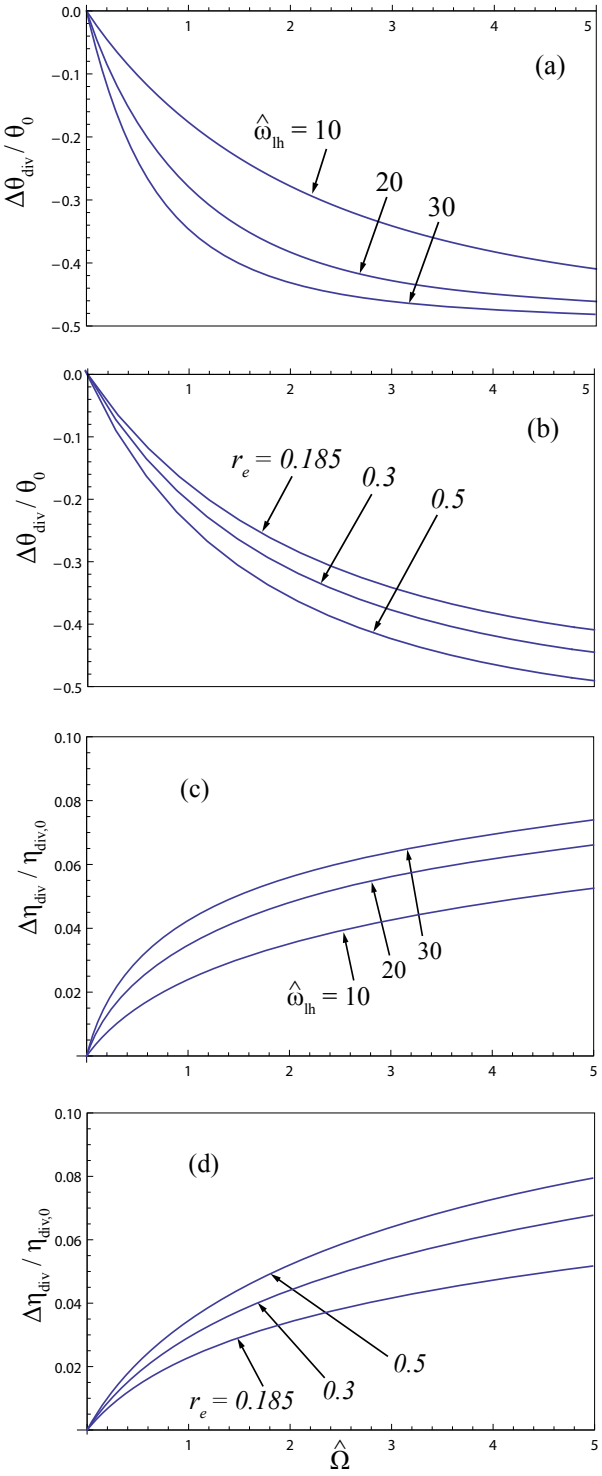

FIG. 6. Relative reduction in plume divergence (a) and (b) and increase in nozzle divergence efficiency (c) and (d) with $\hat{\Omega}$. Graphs (a) and (c) baseline r_e is 0.185 for $\hat{\Omega} = 0$. Graph (b) and (d) magnetization parameter $\hat{\omega}_{\rm lh} = 10$.

Some of the issues with this system may be the raise of the electron inertia, which leads to efficiency loss as ob-

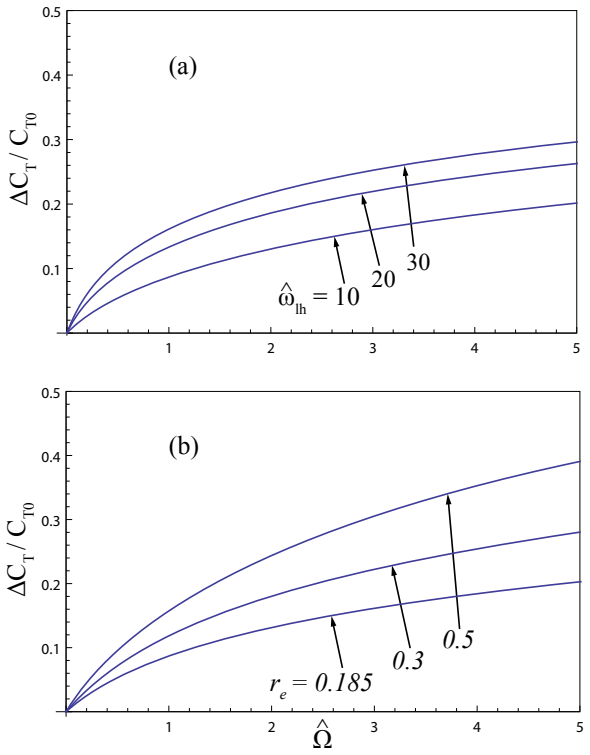

FIG. 7. Relative increase in nozzle thrust coefficient with $\hat{\Omega}$. Upper graph baseline r_e is 0.185 for $\hat{\Omega} = 0$. Lower graph magnetization parameter $\hat{\omega}_{\rm lh} = 10$.

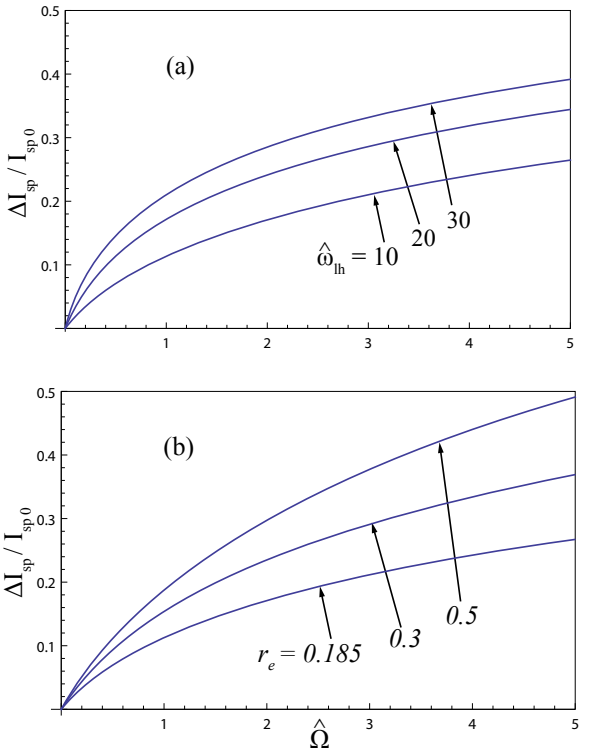

FIG. 8. Relative increase in normalized specific impulse $\hat{I}_{\rm sp}$ with $\hat{\Omega}$. Upper graph baseline r_e is 0.185 for $\hat{\Omega} = 0$. Lower graph magnetization parameter $\hat{\omega}_{\rm lh} = 10$.

served by Ahedo and Merino,[11] and the induced diamagnetic magnetic field, which would increase the divergence of the magnetic field lines.[33].

C. Power Assessment

To assess the efficiency of the body force $\hat{F}$ in increasing the performances of the overall thruster, we can plot the ratio between the increase in the axial jet power and the body force power $\Delta\mathcal{P}_b^*/\mathcal{P}_{\hat{F}}$, where $\mathcal{P}_b^*$ and $\mathcal{P}_{\hat{F}}$ are defined from Eq. 33 and Eq. 21, respectively.

As clear from Fig. 9, the axial power gain overcomes the power introduced by the focusing stage. We must clarify that this increase in the axial power comes from a better conversion of the overall jet power $\mathcal{P}_b$ and not from $\mathcal{P}_{\hat{F}}$, and the overall efficiency remains below the unity. Thus, the body force $\hat{F}$ acts only as an mean of a better conversion of thermal power to axial kinetic power, and not as a net power source for the jet.

We could state that the same power $\mathcal{P}_{\hat{F}}$ of the focusing stage could be used to directly increase the power of the jet, for example by heating the electron fluid to an higher T_e. Thus, we can compare the effects of this temperature increase with those of the introduction of the azimuthal body force. In other words, we can plot the ratio between the axial power in swirling regime $\mathcal{P}^*_{\rm b,S}$

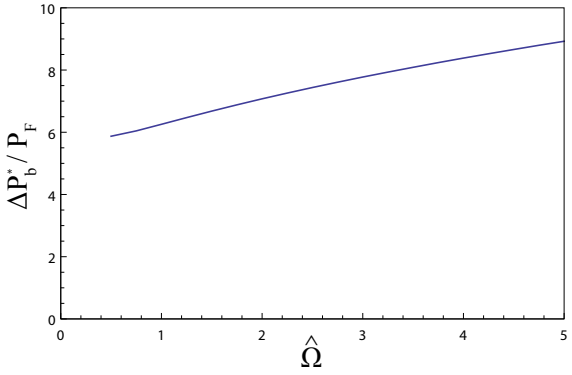

FIG. 9. Ratio between jet axial powers in swirling and increased electron temperature regimes. Magnetization parameter $\hat{\omega}_{\rm lh} = 10$, throat radius $r_e = 0.185$. The plot is limited to $\hat{\Omega} \geq 0.5$, since the limitations of our definition of $\hat{F}$ described in sec Sec. II D lead to unphysical results for lower $\hat{\Omega}$.

and the axial power in augmented temperature regime $\mathcal{P}^*_{\rm b,H} = \eta_{\rm div,0}\left(\mathcal{P}_b + \mathcal{P}_{\hat{F}}\right)$.

From Fig. 10 we see that the ratio $\mathcal{P}^*_{\rm b,S}/\mathcal{P}^*_{\rm b,H}$ is always greater than the unity, thus the axial power recovery due to the introduction of $\hat{F}$ is higher than that gained through an augmented overall beam power. This result makes of the concept of focusing stage a promising mean of increasing the performances of MN-based thrusters,

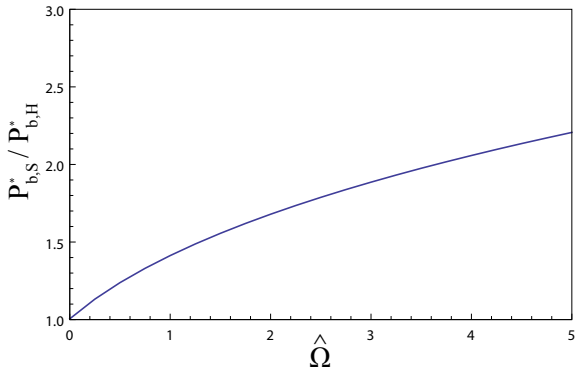

FIG. 10. Ratio between jet axial powers in swirling ($\mathcal{P}^*_{\mathrm{b,S}}$) and increased electron temperature ($\mathcal{P}^*_{\mathrm{b,H}}$) regimes. Magnetization parameter $\hat{\omega}_{\mathrm{lh}} = 10$, throat radius $r_e = 0.185$.

overtaking the well-known difficulties in increasing the electron temperature in helicon plasmas.[34]

V. CONCLUSIONS

In this paper, we assessed the effects on the plasma flow of an azimuthal current induced at the throat of an electro-driven magnetic nozzle. The physics has been investigated by means of a finite-temperature two-dimensional axysimmetric model. The modified equilibrium conditions at the throat have been evaluated through the introduction of an azimuthal body force on the electrons. The flow in the nozzle have been solved using an analyitical approximation. We found that the effect of the azimuthal current on the plume passes through a modified radial density distribution and, as such, can be modeled only by means of a finite-temperature model.

We evaluated the propulsive performance in the swirled regime in terms of plume divergence, nozzle divergence efficiency, thrust coefficient and normalized specific impulse. All these parameters are enhanced by the confining effect of the applied azimuthal force. Stronger enhancements have been found for higher plume magnetization and initially inefficient configuration of the nozzle coil.

An assessment on the beam axial power gain shows that the introduction of an azimuthal force is more efficient than a direct increase of the total jet power, making of the concept of focusing stage a desirable mean of enhancing the performances of magnetic nozzle thrusters.

ACKNOWLEDGMENTS

The work of the first author has been supported by the scholarship *Borsa di Studio Tesi All'Estero 2012-2013* of the Politecnico di Milano.

[1]S. Cohen, X. Sun, E. Ferraro, N.M. abd Scime, M. Miah, S. Stange, N. Siefert, and R. Boivin, IEEE Trans. Plasma Sci. **34**, 792 (2006).
[2]R. Hoyt, J. Scheuer, K. Schoenberg, R. Gerwin, R. Moses, and I. Henins, IEEE Trans. Plasma Sci. **23**, 481 (1995).
[3]K. Schoenberg, R. Gerwin, R. Moses Jr., J. Scheuer, and H. Wagner, Physics of Plasmas **5**, 2090 (1998).
[4]J. Reece Roth, *Industrial Plasma Engineering: Volume 2 - Applications to Nonthermal Plasma Processing* (CRC Press, Boca Raton, FL, USA, 2001).
[5]C. Olsen, M. Ballenger, M. Carter, F. Chang Daz, M. Giambusso, T. Glover, A. Ilin, J. Squire, B. Longmier, E. I. Bering, and P. Cloutier, in *Proceedings of the 33rd International Electric Propulsion Conference* (2013).
[6]E. B. Hooper, Journal of Propulsion and Power **9**, 757 (1993).
[7]R. W. Moses, R. A. Gerwin, and S. K. F., in *Proceedings of the 9th symposium on space nuclear power systems* (1992).
[8]J. M. Little and E. Y. Choueiri, in *Proceedings of the 47th AIAA/ASME/SAE/ASEE Joint Propulsion Conference* (2011).
[9]P. F. Schmit and N. J. Fisch, Journal of Plasma Physics **75**, 359 (2009).
[10]E. Ahedo and M. Merino, Physics of Plasmas **17**, 073501 (2010).
[11]E. Ahedo and M. Merino, Physics of Plasmas **19**, 083501 (2012).
[12]J. M. Little and E. Y. Choueiri, Physics of Plasmas **20**, 103501 (2013).
[13]H. Alfvén, Space Physics **81**, 4019 (1976).
[14]C. C., K. Takahashi, and R. Boswell, Applied Physics Letters **100**, 113504 (2012).
[15]B. Longmier and J. Sheehan, in *Proceedings of the 40th IEEE International Conference on Plasma Science* (2013).
[16]N. Sakaguchi, Y. Kajimura, and H. Nakashima, Trans. Japan Soc. Aero. Space Sci. **48**, 180 (2005).
[17]J. Santarius and B. Logan, Journal of Propulsion and Power **14**, 519 (1998).
[18]W. Von Jaskowsky, A. Kelley, R. Jahn, and J. Polk, Journal of Propulsion and Power **3**, 33 (1987).
[19]K. Kuriki and O. O., Phys. Fluids **13**, 2262 (1970).
[20]E. Ahedo and M. Merino, in *Proceedings of the 48th AIAA/ASME/SAE/ASEE Joint Propulsion Conference* (2012).
[21]A. V. Arefiev and B. B. N., Physics of Plasmas **12** (2005).
[22]C. Deline, R. Bengtson, B. Breizman, M. Tushentsov, J. Jones, D. Chavers, C. Dobson, and B. Schuettpelz, Physics of Plasmas **16** (2009).
[23]E. Ahedo, Plasma Phys. Control. Fusion **53**, 124037 (2012).
[24]R. A. Clemente, J. Phys. Soc. Japan **67**, 3450 (1998).
[25]W. N. Hugrass, Plasma Phys. Control. Fusion **42**, 1219 (2000).
[26]W. N. Hugrass, Plasma Phys. Control. Fusion **45**, 209 (2003).
[27]E. Ahedo, Physics of Plasmas **16**, 113503 (2009).
[28]F. Chen, *Introduction to Plasma Physics and Controlled Fusion. Second Edition. Volume 1: Plasma Physics* (Plenum Press, New York, NY, USA, 1984).
[29]L. Steinhauer, Physics of Plasmas **8**, 3367 (2001).
[30]P. Chabert and N. Braithwaite, *Physics of Radio-Frequency plasmas* (Cambridge University Press, Cambridge, UK, 2011).
[31]B. N. Breizman and A. A. V., Physical Review Letters **84**, 3863 (2000).
[32]R. A. Gerwin, "Integrity of the plasma magnetic nozzle," Tech. Rep. TP-2009-213439 (NASA, 2009).
[33]E. Ahedo and M. Merino, Physics of Plasmas **18**, 053504 (2011).
[34]S. Tonooka, I. Funaki, T. Matsuoka, S. Iwabuchi, T. Nakamura, S. Shinohara, and N. H., in *Proceedings of the 33rd International Electric Propulsion Conference* (2013).